

UNIVERSIDADE
LUSÓFONA

Multiple Access Networks Assisted by Aerial Intelligent Reflecting Surfaces

Brena Kelly Sousa Lima

Thesis to obtain the Degree of Doctor of Philosophy in
Computer Science

Advisers: Rui Dinis

Professor Dr., NOVA University, Costa da Caparica, Portugal

Marko Beko

Professor Dr., Lusofona University, Lisbon, Portugal

Daniel Benevides da Costa

*Professor Dr., King Fahd University of Petroleum & Minerals,
Dhahran, Saudi Arabia*

September, 2024

Multiple Access Networks Assisted by Aerial Intelligent Reflecting Surfaces

Copyright © Brena Kelly Sousa Lima, Departamento de Engenharia Informática e Sistemas de Informação, Universidade Lusófona.

The Departamento de Engenharia Informática e Sistemas de Informação and the Universidade Lusófona have the right, perpetual and without geographical boundaries, to file and publish this dissertation through printed copies reproduced on paper or on digital form, or by any other means known or that may be invented, and to disseminate through scientific repositories and admit its copying and distribution for non-commercial, educational or research purposes, as long as credit is given to the author and editor.

With all my love, I dedicate this Thesis to my parents, Moabe and
Cristiane, and to my sisters, Bruna and Beatriz.



Acknowledgements

This doctoral dissertation was carried out at the COPELABS and the Department of Computer Engineering and Information Systems, Lusofona University, Lisbon, Portugal, from November 2020 to February 2024. This work is funded by Fundação para a Ciência e Tecnologia under the project UIDB/50008/2020, UIDB/04111/2020, and in part by ROBUST under Grant EXPL/EEI-EEE/0776/2021.

I would like to express my gratitude to my supervisor Prof. Dr. Marko Beko, from the Lusofona University and Instituto Superior Técnico, Portugal, for giving me the opportunity of pursuing my doctoral studies with COPELABS. Many thanks for the friendship and the constant encouragement to my academic and personal achievements.

Many thanks to my supervisor Prof. Dr. Daniel Benevides da Costa, from the Department of Electrical Engineering, King Fahd University of Petroleum & Minerals, Dhahran, Saudi Arabia, for your unwavering guidance and support during both my master's and doctoral studies. Your knowledge and invaluable comments were indispensable in bringing this work to completion.

I would like to extend my gratitude to my supervisor Prof. Dr. Rui Dinis, from the NOVA University of Lisbon and Instituto de Telecomunicações, Portugal, for your support throughout this period. Many thanks for your insightful comments, which have undoubtedly been instrumental in the development of this doctoral dissertation.

I want to express my sincere gratitude to Prof. Dr. Rodolfo Oliveira, from the NOVA University Lisbon and Instituto de Telecomunicações, Portugal, and Prof. Dr. João Pedro de Carvalho, from the Lusofona University, Portugal, for their collaboration and ideas. I am also thankful to Prof. Dr. Slavisa Tomic, from the Lusofona University, Portugal, for the warm reception I received at COPELABS and for reading this doctoral dissertation.

With all my heart, my deepest gratitude to my father, Moabe de Castro Lima, my mother, Cristiane Oliveira Sousa Lima, and my sisters, Bruna Kércia Sousa Lima and Beatriz Sousa Lima. Their unwavering faith in me have made this accomplishment possible. Throughout this journey, even with the continental distance, your love, support and understanding have been my guiding

light.

Lastly, but certainly not least, I wish to extend my thanks to all my friends, whose support has made my doctorate journey more enjoyable and the days easier. Many thanks to Amanda Pirola, Carolina Melo, Caroline Costa, Diana Sampaio, Eloise de Carvalho, Isaac Newton Machado, Mariana Nunes, Rui Vigelis, Syllas Magalhães, Tiago Bago, Victória Tomé and Zuil Pirola. Each of you is aware of the affection you have given me and the affection I have for you.



Abstract

In this doctoral dissertation, the conducted research explores the integration of multiple access techniques, such as Non-Orthogonal Multiple Access (NOMA) and Rate-Splitting Multiple Access (RSMA), with Aerial Intelligent Reflecting Surface (AIRS), as these technologies have been highlighted as enablers for the design of the next-generation wireless communication, for enabling resource-efficient simultaneous transmissions and for shaping communication environments characterized by optimized signal radiation. A comprehensive literature review is conducted, revealing potential shortcomings in existing research. To address these gaps, this document offers in-depth discussions on various aspects, including the performance interplay of these techniques, the effects of imperfect Successive Interference Cancelation (SIC), the efficacy of Intelligent Reflecting Surface (IRS)s in both terrestrial and aerial scenarios, and the advantages IRSs bring to multiple antennas in NOMA and RSMA systems. Building upon these insights, solutions aimed at enhancing system performance in terms of throughput, energy efficiency, and coverage are proposed. These solutions leverage a combination of traditional optimization methods and state-of-the-art machine learning approaches for development and implementation. Specifically, Chapter 2 introduces the integration of Unmanned Aerial Vehicle (UAV) in a NOMA network. Problems in the context of user pairing and power coefficient allocation are investigated. By using Reinforcement Learning (RL) algorithms, framework based on Multi-Armed Bandit (MAB) is developed. The proposed method can successfully identify the best user pairing matrix, which leads to maximum system throughput. Chapter 3 provides the fundamentals, potential achievements, and challenges when AIRS are integrated in NOMA networks. By extensive simulation results, attractive gains related to the data rate maximization, user fairness, energy efficiency, and coverage range are highlighted. Chapter 4 investigated the integration of RSMA network with AIRS. An optimization problem is formulated in order to maximize the total achievable rate by optimizing the transmit beamforming and common achievable rate of the users. In order to handle the formulated problem, an algorithm based on Alternating Optimization (AO) method is proposed. In addition, Chapter 5 presents an RSMA network with multiusers assisted by AIRS. To improve the sum-rate of the system,

the UAV's trajectory and phase-shift vectors are optimized, in which the mobility scenarios with static and dynamic users are explored. In particular, Long Short-Term Memory (LSTM)-based frameworks for predicting the UAV's trajectory and the phase-shift of the reflecting elements of AIRS are proposed. For more insight, a third model is created by combining information from the static and dynamic scenarios. Training progress and testing results are provided to demonstrate the efficiency of the proposed models, such as numerical simulations to verify the performance gains in terms of sum-rate. Finally, Chapter 6 presented an overview and conclusions related to the work developed in this doctoral dissertation.

Keywords: Intelligent reflecting surfaces, machine learning, non-orthogonal multiple access, performance analysis, rate-splitting multiple access, unmanned aerial vehicles



Resumo

Nesta tese de doutorado, a pesquisa realizada explora a integração de técnicas de acesso múltiplo, como Non-Orthogonal Multiple Access (NOMA) e Rate-Splitting Multiple Access (RSMA), com Aerial Intelligent Reflecting Surface (AIRS), uma vez que essas tecnologias têm sido destacadas como facilitadoras para o projeto da comunicação sem fio de próxima geração, permitindo transmissões simultâneas eficientes e moldando ambientes de comunicação caracterizados por uma radiação de sinal otimizada. Uma revisão abrangente da literatura é realizada, revelando possíveis deficiências na pesquisa existente. Para abordar essas lacunas, este documento oferece discussões detalhadas sobre diversos aspectos, incluindo a interação de desempenho dessas técnicas, os efeitos do Successive Interference Cancelation (SIC) imperfeito, a eficácia de AIRS em cenários terrestres e aéreos, e as vantagens que AIRS trazem para sistemas NOMA e RSMA com múltiplas antenas. Com base nessas percepções, são propostas soluções com o objetivo de melhorar o desempenho do sistema em termos de taxa de dados, eficiência energética e cobertura. Essas soluções aproveitam uma combinação de métodos de otimização tradicionais e abordagens de aprendizado de máquina para desenvolvimento e implementação. Especificamente, o Capítulo 2 introduz a integração de Unmanned Aerial Vehicle (UAV) em uma rede NOMA. Problemas no contexto de emparelhamento de usuários e alocação de coeficiente de potência são investigados. Por meio do uso de algoritmos de Reinforcement Learning (RL), um framework baseado em Multi-Armed Bandit (MAB) é desenvolvido. O método proposto pode identificar com sucesso a melhor matriz de emparelhamento de usuários, o que leva ótima taxa de dados do sistema para aquele cenário. O Capítulo 3 fornece os fundamentos, potenciais ganhos e desafios quando AIRS são integrados em redes NOMA. Por meio de resultados extensivos de simulação, ganhos atraentes relacionados à maximização da taxa de dados, equidade de taxa entre os usuários, eficiência energética e alcance de cobertura são destacados. No Capítulo 4 investiga-se a integração de uma rede RSMA com AIRS. Um problema de otimização é formulado para maximizar a taxa total alcançável ao otimizar o *beamforming* de transmissão e a taxa alcançável dos usuários. Para lidar com o problema formulado, um algoritmo baseado em Alternating Optimization (AO) é proposto. Além disso, o Capítulo 5 apresenta uma

rede RSMA com vários usuários assistidos por AIRS. Para melhorar a soma das taxas do sistema, a trajetória do UAV e os vetores de mudança de fase da AIRS são otimizados, em que os cenários de mobilidade com usuários estáticos e dinâmicos são explorados. Em particular, estruturas baseadas em Long Short-Term Memory (LSTM) para prever a trajetória do UAV e a mudança de fase dos elementos reflectores da AIRS são propostas. Para obter mais discussões perspicazes, um terceiro modelo é criado ao combinar informações dos cenários estáticos e dinâmicos. O progresso do treinamento e os resultados dos testes são fornecidos para demonstrar a eficiência dos modelos propostos, como simulações numéricas para verificar os ganhos de desempenho em termos de soma de taxa. Finalmente, o Capítulo 6 apresenta uma visão geral e conclusões relacionadas ao trabalho desenvolvido nesta tese de doutorado.

Palavras-chave: Aprendizagem de máquina, acesso múltiplo não ortogonal, acesso múltiplo com divisão de taxas, superfície reflectora inteligente, veículos aéreos não tripulados

Contents

List of Figures	xv
List of Tables	xvii
1 Introduction	1
1.1 Published articles	3
1.2 Awards & Recognition	4
2 User Pairing and Power Allocation for UAV-NOMA Systems Based on Multi-Armed Bandit Framework	5
2.1 Introduction	5
2.2 System Model	8
2.2.1 Channel Model	9
2.2.2 NOMA Transmission	10
2.3 Joint User Pairing and Power Allocation for UAV-NOMA Systems Based on MAB Problem	11
2.3.1 Problem Formulation	12
2.3.2 MAB Framework	12
2.3.3 Action Design	13
2.3.4 Power Allocation Coefficient Design	15
2.3.5 Reward Design	17
2.4 Numerical Results and Discussions	18
2.4.1 Benchmark methods	19
2.5 Conclusions	25
3 Aerial IRS in MIMO-NOMA Networks: Fundamentals, Potential Achievements, and Challenges	27

3.1	Introduction	27
3.1.1	State-of-the-Art	28
3.1.2	Motivation and Contributions	31
3.2	Fundamentals of AIRS and MIMO-NOMA	32
3.2.1	Principles of IRS Structure	33
3.2.2	Architecture of AIRS	34
3.2.3	Aerial IRS in NOMA Networks	35
3.2.4	AIRS-NOMA Networks: System Model	35
3.3	Potential achievements of Aerial IRS-aided MIMO-NOMA Networks	38
3.3.1	Data Rate Maximization	39
3.3.2	User Fairness	41
3.3.3	Energy Efficiency	43
3.3.4	Coverage range	45
3.4	Relevant Challenges and Research Opportunities	47
3.4.1	Channel Model and Estimation Strategies	47
3.4.2	Deployment Strategy	48
3.4.3	Terahertz (THz) Communications	49
3.4.4	Reinforcement Learning in AIRS-NOMA Networks	50
3.4.5	AIRS Standardization	51
3.5	Conclusion	52
4	Rate-Splitting Multiple Access Networks Assisted by Aerial Intelligent Reflecting Surfaces	55
4.1	Introduction	55
4.2	System Model	57
4.3	Beamforming Design for the Proposed AIRS-RSMA Network	59
4.3.1	Problem Formulation	59
4.3.2	Transmit Beamforming Optimization	59
4.4	Simulation Results	63
4.5	Conclusions	65
5	LSTM-based Trajectory and Phase-Shift Prediction for RSMA Networks Assisted by AIRS	67
5.1	Introduction	67
5.1.1	Related works	68
5.1.2	Motivation and Contributions	69
5.2	System Model	70
5.3	Beamforming Design	73
5.4	Phase-shift and Trajectory optimization with LSTM	77
5.4.1	Long Short-Term Memory Networks	77
5.4.2	Trajectory	78

5.4.3	Phase-shift	80
5.5	Results	81
5.5.1	Training Progress	81
5.5.2	Performance Analysis	84
5.6	Conclusions	87
6	Conclusions	89
	Bibliography	91
	Appendices	
A	Proposition 2: Chapter 4	103

List of Figures

2.1	System model.	8
2.2	Illustration of reinforcement learning scheme: agent and environment.	12
2.3	Structure of the proposed method.	16
2.4	Cumulative regret versus TTI for different methods to solve MAB problems ($M = 6$ and $\rho = 35$ dB).	20
2.5	System throughput versus TTI for different methods to solve MAB problems ($M = 6$ and $\rho = 35$ dB).	23
2.6	System throughput versus SNR for different user pairing methods ($M = 6$, $\varepsilon_{1,n} = 0.5$ bits/s/Hz, and $\varepsilon_{2,n} = 1.0$ bits/s/Hz).	23
2.7	System throughput versus SNR: comparison between the power allocation methods ($M = 6$, $\varepsilon_{1,n} = 0.5$, and $\varepsilon_{2,n} = 1.0$).	24
2.8	System throughput versus number of users for different user pairing method and MAB problem solvers ($\rho = 35$ dB, $\varepsilon_{1,n} = 0.5$, and $\varepsilon_{2,n} = 1.0$).	25
3.1	Illustration of the IRS structure.	33
3.2	Illustration of AIRS in MIMO-NOMA networks (AIRS-NOMA) and potential gains of its integration.	33
3.3	Achievable rate versus the transmit SNR for each user group. ($K = 20$, $\alpha_{g1} = 0.7$, $\alpha_{g2} = 0.3$, and $\epsilon = 0.01$).	39
3.4	Sum-rate versus transmit SNR for different number of reflecting elements. ($\alpha_{g1} = 0.7$, $\alpha_{g2} = 0.3$, and $\epsilon = 0.01$).	40
3.5	Sum-rate versus transmit SNR for different coefficients of imperfect SIC (ϵ). ($K = 20$, $\alpha_{g1} = 0.7$, $\alpha_{g2} = 0.3$).	41
3.6	Achievable rate versus transmit SNR for AIRS-NOMA system and TIRS-NOMA system with adaptive PA and fixed PA. When the fixed PA scheme is applied, it is assumed that the power allocation coefficients applied to the users 1 and 2 of the g -th group are, respectively, ($K = 20$, $\alpha_{g1} = 0.7$, $\alpha_{g2} = 0.3$, and $\epsilon = 0.01$).	42

3.7 Jain's fairness index versus SNR for different adaptive PA schemes. When the fixed PA scheme is applied, it is assumed that the power allocation coefficients assigned to the users 1 and 2 of the g -th group are, respectively, ($K = 20$, $\alpha_{g1} = 0.7$, $\alpha_{g2} = 0.3$, and $\epsilon = 0.05$).	42
3.8 Energy efficiency of the system versus the number of reflecting elements of the AIRS and the transmit power for AIRS-NOMA systems. ($\alpha_{g1} = 0.7$, $\alpha_{g2} = 0.3$, and $\epsilon = 0.01$).	43
3.9 Energy efficiency versus transmit power for different number of reflecting elements. ($\epsilon = 0.01$).	44
3.10 Energy efficiency versus transmit power for AIRS-NOMA and TIRS-NOMA systems. Non-neutral power consumption and imperfect SIC are considered. ($K = 20$, $\alpha_{g1} = 0.7$ and $\alpha_{g2} = 0.3$).	45
3.11 Centralized design: Illustration of the scenario used to simulate the results in Figure 3.12.	46
3.12 Sum-rate versus distance for AIRS-NOMA, TIRS-NOMA, and ADF-NOMA deployments. ($\bar{\gamma} = 30$ dB, $K = 20$, and $\epsilon = 0.01$).	46
3.13 Different deployment strategies.	48
3.14 Sum-rate versus SNR for AIRS-NOMA system with centralized and distributed deployment. For centralized deployment, the approximate distance between the AIRS and the group 1, group 2, and group 3 are, respectively, 20m, 50m, 100m. For centralized deployment, the approximate distance between the AIRS and a specific group is 20 m. ($K = 20$, $\epsilon = 0.01$, $\alpha_{g1} = 0.7$, and $\alpha_{g2} = 0.3$).	50
4.1 Illustration of AIRS-RSMA network with two users.	56
4.2 Sum-rate versus transmit SNR for different levels of imperfect SIC and $L = 50$	64
4.3 Sum-rate versus transmit SNR for different deployment, number of reflecting elements and $\epsilon = 0.01$	64
5.1 Illustration of AIRS-RSMA network with two groups of users.	70
5.2 Architecture of the proposed system.	78
5.3 Generating the observation space.	82
5.4 Root Mean Squared Error (RMSE) and loss training results for trajectory model with the static and dynamic group movement.	83
5.5 RMSE and loss training results for phase-shift model with the static and dynamic group movement.	83
5.6 Performance comparison static scenario with $\rho = 40$ dB and $\epsilon = 0.1$	85
5.7 Performance comparison dynamic scenario with $\rho = 40$ dB and $\epsilon = 0.1$	86
5.8 Sum-rate for AIRS-RSMA scheme versus transmit Signal-to-Noise Ratio (SNR) for static scenario with different prediction models.	87
5.9 Sum-rate for AIRS-RSMA scheme versus transmit SNR for dynamic scenario with different prediction models.	87

List of Tables

2.1	Simulation parameters.	19
3.1	List of the papers that considered the integration of IRS in future wireless technologies, such as UAV, NOMA, and MIMO. Notions: ✓ → partial discussion. ✓✓ → Detailed discussion. x → no discussion. * → text-based work. ** → text- and performance-based work.	32
3.2	Simulation parameters.	38
3.3	Comparison of AIRS-NOMA with other frameworks.	46
5.1	The proposed custom RNN architecture hyperparameters for AI trajectory model. .	79
5.2	The proposed custom Recurrent Neural Network (RNN) architecture hyperparameters for Artificial Intelligence (AI) trajectory model.	80



Acronyms

3GPP	3rd Generation Partnership Project 51, 52)
5G	fifth-generation 52)
6G	sixth-generation 27, 52, 55)
ADF-NOMA	aerial decode-and-forward relaying with NOMA 32, 39, 40, 44–46, 52)
AF	amplify-and-forward 34)
AI	Artificial Intelligence xvii, 78, 80)
AIRS	Aerial Intelligent Reflecting Surface vii, ix, x, xvi, 1–3, 28, 29, 31, 32, 35–41, 44, 45, 47–52, 55–57, 63, 65, 67, 69–73, 78, 80, 81, 84, 87, 88, 90)
AIRS-NOMA	aerial IRS in MIMO-NOMA 2, 31, 32, 38–41, 43–52, 56)
AIRS-RSMA	aerial IRS in MISO-RSMA 2, 3, 56, 58, 63–65, 90)
AO	Alternating Optimization vii, ix, 3, 56, 62, 65, 70, 77, 90)
AoA	angle of arrival 34)
AP	access point 29, 31, 68)
AWGN	additive Gaussian noise 37, 58, 72)
B5G	Beyond Fifth-Generation 5, 52)
BS	Base Station 3, 7, 27–29, 31, 34–36, 38, 39, 45, 47, 48, 50, 51, 55–57, 59, 61, 63, 65, 67–71, 73, 74, 84, 90)
CDMA	Code Division Multiple Access 1)
CMAB	Combinatorial Multi-Armed Bandit 15)
CSI	Channel Status Information 7, 10, 34, 37, 39, 47, 48, 51, 52, 61, 76)
D3QN	Dueling Double Deep Q-network 68)

DDPG	Deep Deterministic Policy Gradient 69)
DF	decode-and-forward 34)
DL	Deep Learning 68, 72, 84, 87)
DoF	Degree-of-Freedom 55, 63, 67)
DQN	Deep Q-Learning 68)
DRL	Deep Reinforcement Learning 31, 68)
e2e	end-to-end 36–38, 47, 57, 58, 72, 73)
EM	Electromagnetic 33)
ETSI	European Telecommunications Standards Institute 52)
FD	Full-Duplex 6, 34)
FDMA	Frequency Division Multiple Access 1)
GPS	Global Positioning System 78)
HCC	Hard Channel Condition 7, 11, 17)
HD	Half-Duplex 8)
IMU	Inertial Measurement Unit 78)
IoT	Internet-of-Things 5, 6, 8, 29–31, 69)
IRS	Intelligent Reflecting Surface <i>vii</i> , 1, 2, 28–41, 43–45, 47–52, 55–57, 63, 64, 67, 68, 71, 81, 89, 90)
ISG	Industry Specification Group 52)
LoS	Line-of-Sight 6, 9, 28, 34, 39, 40, 44, 45, 50, 56, 68)
LSTM	Long Short-Term Memory <i>viii</i> , <i>x</i> , 3, 68–70, 77, 80–82, 87, 90)
MA	Multiple Access 1, 90)
MAB	Multi-Armed Bandit <i>vii</i> , <i>ix</i> , 2, 6–8, 12, 13, 17–19, 24, 25, 89)
MC	Monte Carlo 18, 38)
MIMO	Multiple-Input Multiple-Output 2, 29–31, 35, 38, 39, 45, 52, 56, 67)
MISO	Multiple-Input Single-Output 2, 31, 56, 57, 63, 65, 68, 69, 87)
ML	Machine Learning 6, 68, 69)
NLoS	non line-of-sight 28, 56, 68)
NOMA	Non-Orthogonal Multiple Access <i>vii</i> , <i>ix</i> , 1–3, 5–8, 10–13, 15, 17, 23, 27–32, 35, 36, 38, 39, 41, 43, 45, 47–52, 55, 63, 65, 67, 68, 81, 84, 88–90)
OFDMA	Orthogonal Frequency Division Multiple Access 1)

OMA	Orthogonal Multiple Access <i>1, 7, 11, 12, 15, 17, 23–25</i>)
PA	Power Allocation <i>2, 7, 8, 15, 16, 19, 24, 25, 41, 42</i>)
PID	proportional–integral–derivative <i>78</i>)
QoS	Quality of Service <i>2, 7, 11, 13, 15, 16, 24, 25, 35, 48</i>)
RHI	Residual Hardware Impairment <i>30</i>)
RIS	Reconfigurable Intelligent Surface <i>30, 68, 69</i>)
RL	Reinforcement Learning <i>vii, ix, 2, 6, 12, 17, 31, 51, 52, 89</i>)
RMSE	Root Mean Squared Error <i>xvi, 82–84</i>)
RNN	Recurrent Neural Network <i>xvii, 68, 77, 78, 80</i>)
RSMA	Rate-Splitting Multiple Access <i>vii, ix, x, xvi, 1–3, 55–58, 64, 65, 67–73, 84, 87–90</i>)
RWP	Random Waypoint <i>8, 9</i>)
SC	Superposition Coding <i>5, 10, 27, 35, 39</i>)
SDP	Semi-Definite Program <i>2, 56, 62, 65, 70, 77, 90</i>)
SIC	Successive Interference Cancelation <i>vii, ix, 2, 5, 7, 10, 11, 16, 17, 19, 24, 27, 37, 39–41, 44, 51, 55, 56, 58, 59, 63, 65, 67–69, 72, 73, 84</i>)
SINR	Signal-to-Interference-plus-Noise Ratio <i>10, 11, 30, 37, 58, 69, 72</i>)
SNR	Signal-to-Noise Ratio <i>xvi, 10, 37, 40–42, 45, 58, 63, 64, 72, 81, 84–87</i>)
SWIPT	Simultaneous Wireless Power Transfer and Information Transmission <i>29</i>)
TDMA	Time Division Multiple Access <i>1, 15</i>)
THz	Terahertz <i>29, 31, 49, 50, 52, 68</i>)
TIRS	Terrestrial Intelligent Reflecting Surface <i>28, 30–32, 38–40, 56, 64, 65, 67, 69</i>)
TIRS-NOMA	Terrestrial IRS-aided MIMO-NOMA Networks <i>39–41, 44–46, 50, 52</i>)
TTI	Transmission Time Interval <i>10, 12, 13, 17, 21, 22</i>)
UAS	Unmanned Aerial Systems <i>52</i>)
UAV	Unmanned Aerial Vehicle <i>vii–x, 1, 2, 5–10, 12, 14, 17–19, 27–32, 34, 38–40, 43–45, 47, 50–52, 56, 57, 63, 65, 69–72, 78–81, 84, 87, 89, 90</i>)
UCB	Upper Confidence Bound <i>2, 7, 13, 17, 18, 21</i>)
URLLC	ultra-reliable low latency <i>29</i>)
ZF	zero-forcing <i>63</i>)

CHAPTER

1

Introduction

Driven by the growth in number of network-connected devices and the quick development of applications with different requirements, the next-generation wireless networks must provide pervasive connectivity with high data rates, high reliability, and low latency, by exploring efficiently the available resources. To adaptively handle the stringent requirements of the different network infrastructures expected for the next-generation wireless networks, Multiple Access (MA) techniques play an increasingly significant role in providing those ubiquitous capabilities.

In particular, MA techniques can be broadly categorized into two approaches: orthogonal and non-orthogonal. Orthogonal Multiple Access (OMA) techniques have been applied over the years, including examples such as Time Division Multiple Access (TDMA), Code Division Multiple Access (CDMA), Frequency Division Multiple Access (FDMA), and Orthogonal Frequency Division Multiple Access (OFDMA). These techniques allow only a single user to occupy the same time/frequency resource block, or, in the case of CDMA, allow several users to be supported in the same resource block by orthogonal code sequences [0]. In contrast to OMA, non-orthogonal techniques enable a transmitter to efficiently serve multiple users concurrently on a single frequency channel. This is achieved through multiplexing in either the power domain or the code domain. Within the realm of existing techniques, Non-Orthogonal Multiple Access (NOMA) and Rate-Splitting Multiple Access (RSMA) emerge as noteworthy approaches, providing services to meet the evolving demands of the next generations of mobile communication.

Based on this, the aim of this research is to explore the powerful integration of multiple access technologies, such as NOMA and RSMA, with Aerial Intelligent Reflecting Surface (AIRS). The latter involves a planar metasurface Intelligent Reflecting Surface (IRS) mounted onto a Unmanned Aerial Vehicle (UAV) [0], which will be thoroughly investigated in this document. The goal is to identify gaps in the current literature regarding this potential interaction and propose models to enhance system performance in terms of achievable rate, energy efficiency, and coverage. Problems related to this integration are sequentially explored. For each identified issue, a comprehensive and consistent literature review is presented, along with the motivation and objectives. Subsequently,

novel solutions are proposed to improve system performance, utilizing conventional optimization approaches and/or methods based on machine learning.

To support the efficiency of the proposed solutions, extensive simulation results are provided. Furthermore, articles are written and published to corroborate the eligibility of the obtained results. Articles published in full are presented in chapters format in this document, which can be summarized as the following:

- **Chapter 2:** In this chapter, the joint user pairing and power coefficient allocation for UAV systems which employ NOMA to communicate with multiple ground users is investigated. Aiming to maximize the achievable sum rate and ensure the users' Quality of Service (QoS) requirements, we formulate an optimization problem that relies on Reinforcement Learning (RL) from Multi-Armed Bandit (MAB) framework to propose a solution based on Upper Confidence Bound (UCB) approach. The proposed solution can successfully identify the best action and selects it more often, which leads to maximum system throughput. The attained results show that the proposed scheme finds the best-performing action fast, while the other methods spend a lot of time exploring non-ideal user pairs. As a result, the proposed method accumulates less regret and achieves satisfactory results in terms of system throughput when compared to other user pairing strategies and Power Allocation (PA) policies.
- **Chapter 3:** This chapter presents the fundamentals, potential achievements, and challenges when AIRS are integrated in Multiple-Input Multiple-Output (MIMO)-NOMA Networks. In particular, NOMA techniques and UAVs have been recognized as promising technologies for enabling the stringent requirements of the different network infrastructures expected for the next generation of wireless networks. In parallel, IRSs have been widely pointed out as an auspicious solution to further improve spectral efficiency, coverage range, and connectivity. By integrating IRS with UAV and NOMA schemes with MIMO it is possible to smartly improve the overall network performance. In order to explore some of these potentials, this work provides a comprehensive discussion about the interplay of aerial IRS in MIMO-NOMA (AIRS-NOMA) networks, as well its architecture, functionality principles, and performance gains. In particular, attractive gains related to data rate maximization, user fairness, energy efficiency, and coverage range are highlighted. Simulation results are provided to support our insightful discussions, in which it is revealed that the performance gains of AIRS-NOMA networks are superior when compared to terrestrial deployment. In addition, to guide new studies perspectives, it is addressed some issues and research opportunities associated with this potential integration.
- **Chapter 4:** This chapter investigates RSMA networks assisted by AIRS and assuming a downlink Multiple-Input Single-Output (MISO) scenario (aerial IRS in MISO-RSMA (AIRS-RSMA)) with imperfect Successive Interference Cancelation (SIC). An optimization problem is formulated in order to maximize the total achievable rate by optimizing the transmit beamforming and common achievable rate of the users. By using approximation and transformation techniques, we convert the optimization problem into a Semi-Definite Program

(SDP) problem. To solve this problem, an algorithm based on Alternating Optimization (AO) is proposed to iteratively solve the transmit beamforming problem. Simulation results are provided to demonstrate the efficiency of the proposed method, in which it is revealed that the performance gains in terms of sum-rate of AIRS-RSMA networks with robust beamforming are significantly greater than the non-optimized AIRS-RSMA and conventional NOMA schemes.

- **Chapter 5:** Building upon the preceding topic, this chapter delves into RSMA networks augmented by AIRS. However, a multiuser scenario is explored, and both the trajectory and phase-shift of AIRS are meticulously investigated. To enhance the system's sum-rate, optimization is applied to the UAV's trajectory and phase-shift vectors, encompassing mobility scenarios featuring both static and dynamic users. Specifically, Long Short-Term Memory (LSTM)-based frameworks are introduced to predict the UAV's trajectory and the phase-shift of the reflecting elements within AIRS. To provide deeper insights, a third model is devised by combining information from both static and dynamic scenarios. Additionally, the solution proposed in Chapter 4 is extended to accommodate multiuser scenarios, focusing on refining transmit beamforming at the Base Station (BS). Comprehensive details regarding training progress and testing results are presented to underscore the efficacy of the proposed models. Furthermore, numerical simulations are deployed to validate the performance gains in terms of sum-rate. The simulation results align with the outcomes achieved during the training and testing phases for each investigated scenario. It is noteworthy that the simulation results indicate superior performance in trajectory prediction and phase-shift of the UAV when different scenarios are examined independently.

1.1 Published articles

- **B. K. S. Lima**, J. P. Carvalho, R. Dinis, D. B. da Costa, M. Beko, and R. Oliveira,"LSTM-based Trajectory and Phase-Shift Prediction for RSMA Networks Assisted by AIRS" in IEEE Transactions on Communications, 2024, doi: 10.1109/TCOMM.2024.3407192.
- **B. K. S. Lima**, J. P. Carvalho, R. Dinis, D. B. da Costa, M. Beko, and R. Oliveira,"Trajectory Design for RSMA Networks Assisted by AIRS with LSTM and Transformers" in 19th International Symposium on Wireless Communication Systems (ISWCS), 2024.
- **B. K. S. Lima** et al., "Rate-Splitting Multiple Access Networks Assisted by Aerial Intelligent Reflecting Surfaces," 2022 IEEE Latin-American Conference on Communications (LATINCOM), Rio de Janeiro, Brazil, 2022, pp. 1-6, doi: 10.1109/LATINCOM56090.2022.10000454.
- **B. K. S. Lima**, A. S. de Sena, R. Dinis, D. B. da Costa, M. Beko, and R. Oliveira, "Aerial Intelligent Reflecting Surfaces in MIMO-NOMA Networks: Fundamentals, Potential

Achievements, and Challenges" in IEEE Open Journal of the Communications Society, v. 3, p. 1007-1024, 2022.

- **Lima, B.**, Fachada, N., Dinis, R., Costa, D.B. and Beko, M., 2022. Uavnom: A UAV-NOMA Network Model under Non-Ideal Conditions. *Journal of Open Research Software*, 10(1), p.9. DOI: <http://doi.org/10.5334/jors.397>.
- **B. K. S. Lima, R.** Dinis, D. B. da Costa, R. Oliveira, and M. Beko, "User Pairing and Power Allocation for UAVNOMA Systems Based on Multi-Armed Bandit Framework" in *IEEE Transactions on Vehicular Technology*, 2022, doi: 10.1109/TVT.2022.3199606

1.2 Awards & Recognition

- **Honorable Mention for Presentation:** Most Innovate Ph.D. Thesis in COST CA20120 - INTERACT Training School DolCom 2023, Campitello di Fassa, Trentino-Alto Adige, Italy.

User Pairing and Power Allocation for UAV-NOMA Systems Based on Multi-Armed Bandit Framework

B. K. S. Lima, R. Dinis, D. B. da Costa, R. Oliveira, and M. Beko, "User Pairing and Power Allocation for UAV-NOMA Systems Based on Multi-Armed Bandit Framework" in IEEE Transactions on Vehicular Technology, 2022, doi: 10.1109/TVT.2022.3199606

2.1 Introduction

In the context of the Internet-of-Things (IoT), millions of devices are expected to be able to communicate simultaneously [0]. Several services and applications ranging from smart homes and self-driving cars to interconnected low-power sensors in health, factories, and agriculture are foreseen for Beyond Fifth-Generation (B5G) wireless systems. These different network infrastructures and deployments will impose stringent requirements to the system designers, such as reliable communications, massive connectivity, low latency, low energy consumption, seamless connectivity, and high spectral efficiency [0].

To attend to the tight requirements, numerous strategies and technologies have been proposed. In particular, Non-Orthogonal Multiple Access (NOMA) has been widely pointed out as a promising candidate for multiple access technology of the next generation of wireless networks. Some of its features are high spectral efficiency, massive connectivity, low latency, and user fairness when compared to the orthogonal counterpart [0]. The main idea of NOMA is to perform Superposition Coding (SC) at the transmitter and Successive Interference Cancelation (SIC) at the receiver. These techniques allow to leverage of the coding and decoding process and enable multiple users to share the same resource block with distinct power levels, while users share a common radio resource of time and frequency.

On a parallel avenue, in the last few years, the demand for Unmanned Aerial Vehicle (UAV)s in communication networks has increased due to its cost-effectiveness solution, ability to perform complex tasks in different scenarios, flexible configuration, and deployment in comparison with ground base stations [0]. UAVs can significantly improve the connectivity and coverage of terrestrial

CHAPTER 2. USER PAIRING AND POWER ALLOCATION FOR UAV-NOMA SYSTEMS BASED ON MULTI-ARMED BANDIT FRAMEWORK

wireless devices by enabling flexible deployment. In addition, it can reduce visual pollution and eliminate the need for expensive towers. In comparison with terrestrial base stations, the benefits of UAVs can be reached owing to their capacity to adjust their altitude, avoid obstacles, and enhance the probability of achieving Line-of-Sight (LoS) communication links to ground users [0]. In addition, the combination of the NOMA technique with UAV allows segments to support diverse applications required by the next generations of mobile communications, attracting considerable academic and industrial research interests [0].

In recent years, Machine Learning (ML) has attracted the attention of researchers in the field of telecommunications and has been adopted to solve several wireless communication problems [0], including supervised, unsupervised, and Reinforcement Learning (RL) problems. Supervised learning requires a large dataset for training. This characteristic can make it challenging to apply supervised learning in real-time wireless communication scenarios. In unsupervised learning, machines do not need to supervise the model. Instead, data are classified or estimated. On the other way, the RL methods are a branch of ML whose main characteristic is the learning of the ideal strategy exploring unknown environments based on received rewards.

In particular, RL is a process where an interactive algorithm provides one representation of the particulars in an environment by taking actions and receiving rewards. Based on this, three components must be taken into consideration when designing solutions using RL: agents, rewards, and action. Due to the learning properties, RL has been used in numerous applications [0]. Specifically, the authors in [0] proposed a new approach for UAV dynamic maneuver design based on RL via Q-learning. On the other hand, [0] studied the joint problem of dynamic multi-UAV-NOMA altitude control and multi-cell wireless channel access management of IoT devices as a stochastic control problem with multiple energy constraints. To improve the user pairing on a network, [0] proposed a novel method based on deep learning to solve the problem in a Full-Duplex (FD) network, but without taking into account the NOMA and UAV technologies.

A peculiar RL problem that has been widely used in applications is Multi-Armed Bandit (MAB). In MAB framework, the agent chooses an action among a set of different actions to maximize expected rewards, providing a decision policy [0]. It is worth mentioning that the value rewards are not initially known to the agent, but after an appropriate choice of action, the instantaneous reward of that choice is announced. The idea in solving MAB problems is to explore the action space and understand the distribution of the unknown rewards function. Based on this, the machine needs to decide between multiple choices by taking action and observing the returns. Due to the relatively low complexity since it does not account for the state changes, the MAB framework is an ideal tool for solving the user pairing and power allocation problems of wireless communication systems.

Considering the MAB framework, the authors in [0] proposed a distributed NOMA-based MAB approach to solve the problem of the channel selection and the power level selection, aiming to decrease the impact of the collision in the same channel. In [0], the authors investigated the NOMA system with joint resource allocation and power control problem and proposed a solution based on MAB. The proposed solution allows users to choose the appropriate resource block and power level in a distributed manner. In [0], the optimal UAV position was calculated so that the highest sum rate for the network can be achieved from the perspective of the MAB problem. The authors

used the Upper Confidence Bound (UCB) algorithm to solve the MAB problem. In [0], an online learning framework to characterize the UAV trajectory was investigated. To find the ideal path, the authors formulated an optimization problem and then showed that the problem can be transformed into an extended MAB problem. The authors used the UCB principles to solve the problems. Based on this, two path planning algorithms to learn an energy-efficient path were proposed. The authors in [0] formulated the problems as stochastic MAB and the proposed solutions based on UCB principles. In particular, a new exploration policy to learn resource-efficient scheduling was investigated in [0]. In [0], the exploration-exploitation tradeoff was investigated to allow users to choose the appropriate resource block and power level in a distributed manner.

In the literature, few works have explored the MAB structure to solve problems in NOMA systems served by an aerial Base Station (BS). To fill out partly this gap that exists in the literature, we propose intelligent methods to optimize a UAV-NOMA network with multiple users. Since multiple users are admitted at the same resource block with different power coefficients, the power allocation for each user is quite challenging to be designed. Consequently, the performance of each user can be decreased, resulting in a degradation of the overall system's performance. To overcome this problem, a promising strategy is to separate the users into multiple pairs so that the power coefficients are allocated adaptively. To solve the user pairing and Power Allocation (PA) problems, in this chapter we rely on an intelligent algorithm to make sequential decisions without requiring all the information from the environment. The main contributions of the chapter are summarized as follows:

- We investigate a UAV-enabled downlink NOMA system with multiple mobile IoT devices. In order to maximize the system sum rate and, at the same time, ensure the Quality of Service (QoS) from adaptive power allocation, we formulate an optimization task to find out the optimal user pairing.
- Based on available Channel Status Information (CSI), we verify that the formulated problem can be solved using the MAB framework to perform the user pairing. The reward obtained from a given agent action is formulated based on the difference of gain between the Hard Channel Condition (HCC) of NOMA and HCC of Orthogonal Multiple Access (OMA).
- A PA policy based on the QoS constraint is designed for each pair of users in order to ensure that, by considering the impact of residual error from imperfect SIC, the achievable rate of the NOMA users can be better or equivalent to the one that employs OMA.
- Simulation results with insightful discussions are provided to investigate the performance of the proposed method. We compare the proposed method with conventional user pairing methods, PA policies, and solvers MAB to select the user pairing matrix. In particular, our results show that the proposed method finds the best user pairing matrix with high accuracy. The performance converges to the optimal rate as soon as each user pairing matrix is initialized once. The proposed method outperforms conventional and solvers MAB methods in terms of regret and system throughput.

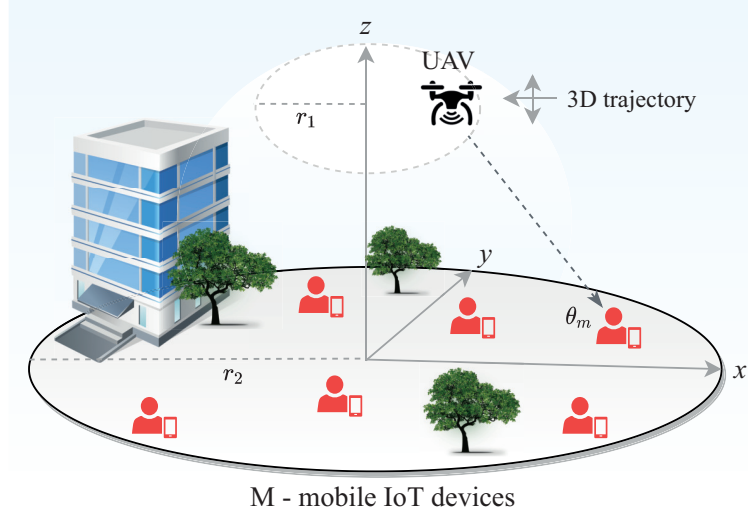


Figure 2.1: System model.

The remainder of this chapter is organized as follows. Section 2.2 describes the system model under consideration. Section 2.3 introduces the user pairing and PA problem and the MAB learning framework for UAV-NOMA networks. In Section 2.4, we conduct a performance evaluation and discussions. Finally, the conclusions are presented in Section 2.5.

2.2 System Model

Let us consider a downlink UAV-aided NOMA network, as illustrated in Fig. 2.1. In this scenario, an UAV is deployed as an aerial base station that communicates with M mobile IoT devices with different channel conditions in an urban macro cell. We consider that each node is equipped with a single antenna and both UAV and users operate in the Half-Duplex (HD) mode. In addition, we assume that the UAV continuously flies with a constant velocity and variant elevation H in a spherical plan of radius r_1 . For a given H , the UAV can fly in the following height range: $H - r_1 \leq z \leq H + r_1$, where z denotes the instantaneous height. Based on three-dimensional Cartesian coordinates, the location of the UAV can be represented by (x, y, z) .

The mobile users' IoT devices move randomly and independently in a circular cell of radius r_2 . The Random Waypoint (RWP) model is implemented to simulate the mobility of the users [0]. The RWP model can interpret the basic properties of many real-world mobility patterns, including the random mobile users in the context of cellular networks. During all periods of the mobility process, the users randomly choose a new coordinate and move to it at a constant speed. For each time slot of the mobility process, the new location of the users is calculated. Based on this, the location of the m -th mobile user can be represented by $(x_m, y_m, 0)$, with $m \in \mathcal{M} = \{1, \dots, M\}$.

For each time slot of the mobility process, the Euclidian distance between the UAV and the

m -th user can be obtained by

$$d_m = \sqrt{(x_m - x)^2 + (y_m - y)^2 + z^2}. \quad (2.1)$$

2.2.1 Channel Model

Based on [0], air-to-ground channel experiences small-scale fading and large-scale fading. Since the RWP path typically exists in our scenario, the ground users can enjoy the LoS communications. Due to LoS communications, the small-scale fading can be modeled by the Rician fading. Therefore, we assume that the channels between the UAV and the mobile IoT devices follow the Rician distribution.

A Rician fading channel can be described using two parameters: 1) Rician factor (K_m) for communication channel with m -th mobile user and 2) the total power accounting for direct path and the scattered paths ($P_{LoS} = \mu^2 + 2\sigma^2$), where μ denotes the mean and σ denotes the standard deviation and variance. According to [0], the Rician factor can be modeled by the following exponential function

$$K_m = A_1 \exp(A_2 \theta_m), \quad (2.2)$$

where A_1 and A_2 denote the adjustable factors to design the environment, $\theta_m = \arctan(z^2/d_m)$ denotes the elevation angle between the UAV and the m -th user. From [0], the Rician factor for urban macro cell environment is approximately $K = 15$. Based on this, we consider $A_1 = 5$ and $A_2 = \frac{2}{\pi} \log(\frac{15}{A_1})$, and calculate the Rician Factor for the m -th user based on θ_m .

Considering a given P_{LoS} and K_m calculated in (2.2), μ and σ can be calculated, respectively, as follows

$$\mu = \sqrt{\frac{K_m}{K_m + 1} P_{LoS}}, \quad (2.3)$$

and

$$\sigma = \frac{P_{LoS}}{\sqrt{2(K_m + 1)}}. \quad (2.4)$$

For an urban macro cell scenario with an aerial base station, the path loss model can be expressed by [0]:

$$PL_m[dB] = 28.0 + 22 \log_{10}(d_m) + 20 \log_{10}(f_c), \quad (2.5)$$

where d_m denotes the distance in meters between the transmitter and the m -th mobile IoT device, and f_c denotes the carrier frequency. Thus, the average power gain of the channel coefficient due to the large-scale fading, taking into account the signal attenuation due to the path loss and shadowing, can be given by

$$\beta_m = 10^{(-PL_m[dB]/10)}. \quad (2.6)$$

The channel coefficient $h_{m,n}$ from UAV to the m -th user of the n -th group, with $m \in \{1, \dots, M\}$ and $n \in \{1, \dots, M/2\}$, can be expressed by

$$h_{m,n} = \sqrt{\beta_{m,n}} g_{m,n}, \quad (2.7)$$

where $g_{m,n} \sim \mathcal{CN}(\mu, 2\sigma^2)$ is the small-scale fading component modeled by the Rician fading from complex Gaussian variables, and $\beta_{m,n}$ denotes the large-scale fading component.

2.2.2 NOMA Transmission

The message of each user pair is superposed based on the SC technique. By pairing two users, it is possible to reduce interference and ensure a low SIC delay on the receiver. In this chapter, we consider that the UAV employs a user pairing method, so that, the two users in each group assume the roles of weak and strong users, represented, respectively, by $U_{1,n}$ and $U_{2,n}$. It is important to mention that the users' channels must be ordered as $|h_{1,n}|^2 < |h_{2,n}|^2$. The users can be viewed as IoT healthcare devices. For example, $U_{1,n}$ can be delay-sensitive with a low target rate which is sharing information about health records, while $U_{2,n}$ can be treated in a delay-sensitive manner, assuming that there is no urgency in sending the file with information about the health.

The communication occurs in a dynamic scenario, where at each Transmission Time Interval (TTI), the UAV performs the user pairing strategy. Thus, the received message by the m -th user of the n -th group is given by

$$y_{m,n} = |h_{m,n}|^2 \sum_{k=1}^2 \sqrt{\alpha_{k,n} P} x_{k,n} + \eta_{m,n}, \quad (2.8)$$

where P denotes the transmit power of the UAV, $x_{k,n}$ denotes the message of interest of the k -th user of the n -th group, with $n = 1, \dots, M/2$. The parameter $\eta_{m,n}$ stands for the additive white Gaussian noise, following complex Gaussian distribution with zero mean and variance σ_m^2 , i.e., $\mathcal{CN}(0, \sigma_m^2)$. The variable $\alpha_{k,n}$ represents the power coefficient of k -th user at the n -th group.

Following the NOMA principle, multiple users can be served in the same resource block (time/frequency) by assigning different power coefficients to them. In order to ensure better performance and improved user fairness, higher power must be allocated to the weaker user, i.e., the user with the worst channel conditions, which means that $\alpha_{1,n} > \alpha_{2,n}$, with $\sum_{k=1}^M \alpha_{k,n} \leq 1$ and $\alpha_{k,n} > 0$.

Thus, based on this power allocation strategy, $U_{1,n}$ decodes its own messages $x_{1,n}$ by treating $x_{2,n}$ as noise. It is noteworthy that we are assuming perfect CSI knowledge. Although this is an optimistic assumption, there are numerous papers that provide powerful techniques for estimating CSI [0]. On the other hand, imperfect SIC is assumed. The imperfect SIC assumption allows us to analyze a more realistic environment, in which there is the presence of residual interference caused by other users' signal. In general, imperfect SIC can be quantified by a parameter that reflects directly on the formulation of the Signal-to-Interference-plus-Noise Ratio (SINR) experienced by users. Therefore, the SINR at the weak user of the n -th group can be expressed by

$$\gamma_{1,n} = \frac{\rho |h_{1,n}|^2 \alpha_{1,n}}{\rho |h_{1,n}|^2 \alpha_{2,n} + 1}, \quad (2.9)$$

where $\rho = \frac{P}{\sigma_m^2}$ denotes the transmit Signal-to-Noise Ratio (SNR) at the UAV.

On the other hand, $U_{2,n}$ firstly decodes the data of the $U_{1,n}$, $x_{2,n}$, and then cancels it from the received signal and detects its data. Thus, the SINR at $U_{2,n}$ can be expressed by

$$\gamma_{2 \rightarrow 1,n} = \frac{\rho |h_{2,n}|^2 \alpha_{2,n}}{\rho |h_{2,n}|^2 \alpha_{1,n} + 1}. \quad (2.10)$$

2.3. JOINT USER PAIRING AND POWER ALLOCATION FOR UAV-NOMA SYSTEMS BASED ON MAB PROBLEM

Employing SIC technique, the SINR at $U_{2,n}$ for detecting its own message, under imperfect SIC conditions, can be written as

$$\gamma_{2,n} = \frac{\rho|h_{n,2}|^2\alpha_{n,2}}{\rho|h_{n,2}|^2\alpha_{n,1}\zeta + 1}, \quad (2.11)$$

where ζ denotes the coefficient of imperfect SIC ($0 \leq \zeta \leq 1$). For instance, $\zeta = 0$ means perfect SIC. On the other hand, when $\zeta = 1$, the SIC process fails completely.

The instantaneous achievable data rate achieved by the weak user, $U_{1,n}$, of the n -th group, can be written as

$$R_{1,n}^{NOMA} = \log_2(1 + \gamma_{1,n}). \quad (2.12)$$

The instantaneous achievable data rate of the strong user, $U_{2,n}$, is given by

$$R_{2,n}^{NOMA} = \log_2(1 + \gamma_{2,n}). \quad (2.13)$$

When OMA is employed, the instantaneous achievable data rate of the weak and strong user of the n -th group is respectively represented by

$$R_{1,n}^{OMA} = \frac{1}{2} \log_2(1 + \rho|h_{1,n}|^2), \quad (2.14)$$

and

$$R_{2,n}^{OMA} = \frac{1}{2} \log_2(1 + \rho|h_{2,n}|^2), \quad (2.15)$$

where $\frac{1}{2}$ factor results from the loss of OMA multiplexing [0].

Based on the achievable data rates, the transmission capabilities of the system by the HCC, which is formulated as

$$\Upsilon = \sum_{n=1}^{M/2} (R_{1,n} + R_{2,n}). \quad (2.16)$$

For clarity, we will use Υ^N to denote the HCC of NOMA systems and Υ^O to represent the HCC of OMA systems. These metrics will be used to design the reward and to analyze the system performance.

2.3 Joint User Pairing and Power Allocation for UAV-NOMA Systems Based on MAB Problem

In this section, we investigate the user pairing and power coefficient allocation to improve the system performance in terms of achievable rate. The main objective is to maximize the system throughput and ensure that the QoS requirements of all users are satisfied through efficient user pairing and energy allocation policy.

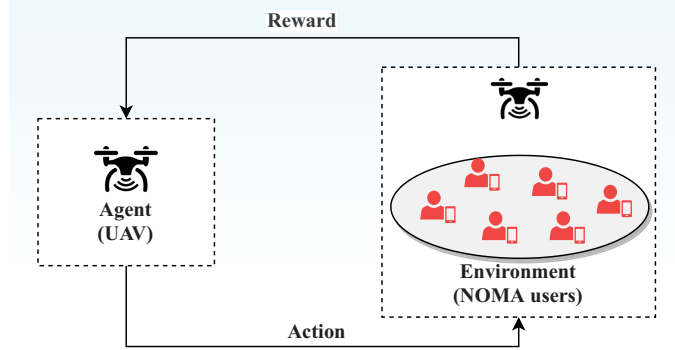


Figure 2.2: Illustration of reinforcement learning scheme: agent and environment.

2.3.1 Problem Formulation

First, we formulated the joint user pairing and power allocation problem to maximize the system sum rate as

$$\max_{\mathbf{A}_i \in \mathcal{A}, n \in \mathbf{A}_i, \alpha} \sum_{n=1}^{M/2} (R_{1,n}^{NOMA} + R_{2,n}^{NOMA}), \quad (2.17)$$

subject to

$$C1 : R_{1,n}^{NOMA} \geq R_{1,n}^{OMA}, \quad (2.18)$$

$$C2 : R_{2,n}^{NOMA} \geq R_{2,n}^{OMA}, \quad (2.19)$$

$$C3 : \alpha_{1,n} + \alpha_{2,n} = 1, \quad (2.20)$$

$$C4 : \alpha_{1,n}, \alpha_{2,n} \geq 0, \quad (2.21)$$

where \mathcal{A} denotes the action space of all possible pairs of users, \mathbf{A}_i is the i -th pairing matrix of the set \mathcal{A} , for $i = \{1, 2, \dots, N\}$, with N denoting the number of user pairing matrices in space \mathcal{A} . It is worth mentioning that the formulation of space \mathcal{A} is described in Section 2.3.3. The parameter α denotes the power coefficient allocation set $(\alpha_{1,n}, \alpha_{2,n})$, where $R_{1,n}^{NOMA}$ and $R_{2,n}^{NOMA}$ are functions of α . The constraints (2.18) and (2.19) ensure that the achievable data rate of NOMA users must be greater than or equal to OMA, (2.20) is the power coefficient constraint, and (2.21) ensures the non-negative power coefficient allocation for each user.

The problem (2.17) can be interpreted as a MAB problem. MABs are a form of RL in which the agent, in our case the UAV, selects an action from the set of available actions. Based on the selected action, a reward is generated. In this process, the agent understands that the best action is the one that produces the best reward.

2.3.2 MAB Framework

The MAB framework is a simplified version of the Markov decision process, where actions are not associated with states [0]. Specifically, when the MAB framework is employed, the agent has no previous knowledge about the rewards of the actions. For each TTI, the agent explores an action in

2.3. JOINT USER PAIRING AND POWER ALLOCATION FOR UAV-NOMA SYSTEMS BASED ON MAB PROBLEM

a set of available ones to find the best value, exploring the best action many times to maximize the total reward. As a result of a given action, the agent receives a reward as feedback that indicates whether the choice is sufficient to satisfy the imposed requirements. This problem is an instance of an *exploration* and *exploitation* dilemma. In summary, when the exploitation method is employed, the agent takes advantage of the best action that knows about the scenario. With exploration, the agent takes some risk to collect information about unknown actions.

However, one can achieve a balance between exploration and exploitation. When using the strategy based on the UCB [0] to solve a MAB problem, it is possible to make choices based on the uncertainty of the action value estimates. This decision strikes a trade-off between choosing the best action that exhibits the most valuable expected gain or taking a risk and testing another action from the set of available actions.

As illustrated in Fig. 2.2, the UAV works as the agent and the users' devices as the environment. In this chapter, we formulate the action to maximize the achievable rate of the system and the rewards designed to ensure that the QoS requirements of the NOMA users can be satisfied through the adaptive allocation of the power coefficients.

Specifically, the MAB framework can be described as a tuple of $\langle \mathcal{A}, \mathcal{R} \rangle$, where at each time step t , the agent takes an action a and receives a reward $r(t, a)$.

- \mathcal{A} is an actions space, each action referring to the different user pairing matrix of the system. The obtained value from the action a , at TTI t , is the expected reward, $\tilde{R}(t, a)$.
- \mathcal{R} is a reward function. We observe a reward in a stochastic way, because at TTI t , $r(t, a)$, the chosen action can return reward with a certain probability.

Based on the actions set, the goal is to maximize the cumulative reward $\sum_{t=1}^T r(t, a)$, where T denotes the total interval. The action and reward designs used to model and solve the problem (2.17) using the MAB framework are presented in the next topic.

2.3.3 Action Design

Since the UAV employs the user pairing strategy. We define the action set of the UAV as the index of the user pairing procedure, where each action represents a combination between the pairs.

Unlike a combination used to indicate how many subsets there are in a set with M elements, we formulate an expression that returns the number of combinations where specific repetitions of pairs between the subsets are allowed, without presenting ambiguity between the indices, i.e., the setting $(1, 2) = (2, 1)$ is not allowed. According to the prescribed rule, we verified that from all possible combinations, we wanted to identify all subsets that generate redundancy between indexes. In this way, we derive next the expression to calculate the dimension of the action space. The number of pairing matrices contained in the action space can be given by:

$$N = \frac{M!}{2^{\frac{M}{2}} (\frac{M}{2})!}, \quad (2.22)$$

where $2^{\frac{M}{2}}$ is designated to identify the number of subsets that present ambiguity between indices, i.e., $(1, 2) = (2, 1)$, and $(\frac{M}{2})!$ is used to identify matrices that have equal pairs, but in a different

order, i.e., $[(1, 2), (3, 4), (5, 6)] = [(5, 6), (1, 2), (3, 4)]$. On the other hand, the following setting is allowed $[(1, 2), (3, 4), (5, 6)] \neq [(1, 2), (4, 6), (3, 5)]$, because the system can achieve different rates. As a result, we eliminate all subsets that generate redundant information.

Based on this, it is possible to considerably reduce the space of actions without affecting the learning process. For example, let us consider a system with $M = 4$ users, using the permutation method, we get $N = 24$. On the other hand, by using the Eq. (2.22) it is possible to reduce the action set to $N = 3$. For $M = 6$ users, we obtain $N = 15$, while using permutation it is obtained $N = 720$. As a result, we achieve less computational complexity, as the UAV will not need much effort to choose the optimal action.

One important step to implement the user pairing is to convert the action set obtained into indexes set, denominated as action space \mathcal{A} , where each index of \mathcal{A} represents an action matrix that the agent can take to organize the users' pairs. After describing all possible sequence combinations, we reshape each action into a matrix of dimension $[\frac{M}{2}, 2]$. For this purpose, the action space $\mathcal{A} \in \mathbb{R}^{\frac{M}{2} \times 2 \times N}$ given to describe user pairing possibilities can be defined as

$$\mathcal{A} = [\mathbf{A}_1, \mathbf{A}_2, \dots, \mathbf{A}_N], \quad (2.23)$$

where $\mathbf{A}_N \in \mathbb{R}^{\frac{M}{2} \times 2}$, wherein each row of \mathbf{A}_N represents a group of user pairs. To simplify the notation, we will denote the matrices contained in the action space \mathcal{A} as $a \in \mathbf{A}_N$. Note that, for each a , it is obtained one distinct pair arrangement. For example, by considering $M = 4$ users, we obtain the following action space:

$$\mathcal{A} = \left\{ \underbrace{\begin{pmatrix} 1 & 2 \\ 3 & 4 \end{pmatrix}}_{a=1}, \underbrace{\begin{pmatrix} 1 & 3 \\ 2 & 4 \end{pmatrix}}_{a=2}, \underbrace{\begin{pmatrix} 1 & 4 \\ 2 & 3 \end{pmatrix}}_{a=3} \right\}.$$

The agent can be chosen between three possible combinations to employ the user pairing, where each row of \mathbf{A}_N represents a group of two users.

Note that the Eq. (2.22) gives us the dimension of the action space, i.e., the number of available actions without ambiguity between the indexes that the UAV can take. In order to explore the various combinations between users to maximize the system rate, a function that returns the action space is implemented. In this way, we were able to verify accurately all settings between user pairs. The function is summarized in the Algorithm 1.

In the best case, where $M = 2$, the runtime of Algorithm 1 is $\Theta(kN)$. On the other hand, when the recursion is needed, the execution time is $\Theta(k^2N)$. To formulate the feasible action space, the algorithm has a quadratic time complexity due to the pairwise processing of the data to form pairs of users. It is important to mention that this complexity occurs at the block or the frame level, not at the bit or symbol level, which means that the required additional complexity is negligible when compared with needed signal processing complexity for equalization and channel decoding. Algorithms of this type are useful for solving relatively small problem sizes that limit the number of users per resource block. To serve a large number of users, we would have to consider some

2.3. JOINT USER PAIRING AND POWER ALLOCATION FOR UAV-NOMA SYSTEMS BASED ON MAB PROBLEM

Algorithm 1 Generate action set

```

Input: symb = [1 : M]
Function: sequence-generate(symb)
1: k = |symb|
2: Calculate N according to (2.22)
3: Initialize the action set action-set = zeros(N, k)
4: Update the action set action-set(:, 1) = symb(1)
5: for i = 1 to k – 1 do
6:   action-set(1 + (i – 1) *  $\frac{N}{k-1}$  : i * N, 2) = symb(i + 1)
7:   if (k ≠ 2) then
8:     idx = 2 : M
9:     idx = idx(idx ≠ (i + 1))
10:    action-set(1 + (i – 1) *  $\frac{N}{k-1}$  : i * N, 3 : end) = sequence-generate(symb(idx))
11:   end if
12: end for
13: for j = 1 to N do
14:   Reshape action-set into indexes matrix  $\mathcal{A}(\frac{M}{2}, 2, j) = \text{action-set}(j, :)$ 
15: end for
16: Return: action-set,  $\mathcal{A} \in \mathbb{R}^{\frac{M}{2} \times 2 \times N}$ 
End Function

```

assumptions in our scenario, which can be imposed through the adoption of clustering methods. Thus, multiple clusters composed of multiple user pairs could be served by the UAV in distinct resource blocks. Since the scenario is composed of a large number of users and, as a consequence, a large action set, i.e., super-arms, the number of exploration rounds grows abruptly, and the regret returned may be incorrect due to the combinatorial nature of the large action space. To circumvent this problem, Combinatorial Multi-Armed Bandit (CMAB) [0] can be used so that a super-arm is played in each round, and the results of its related single arms are observed. In this way, the selection of super arms in future rounds is improved by using the regret approximation of the difference between the expected reward and reward obtained by the optimal super-arm. It is important to mention that the choice of an action by the UAV is determined by the balancing between exploitation and exploration based on UCB strategy.

2.3.4 Power Allocation Coefficient Design

This section investigates both the impact of user pairing and power coefficient allocation. After the UAV takes the first action, groups of user pairs are formed. For each group, the PA coefficients assigned to the users' messages are calculated adaptively.

To ensure that the QoS requirement of NOMA users can be greater or equal than when using OMA technologies, e.g., Time Division Multiple Access (TDMA), we investigate a PA policy for NOMA users subject to the minimum rate constraint.

The instantaneous achievable rate of the weak user ($U_{1,n}$), and the strong user ($U_{2,n}$) of the *n*-th group can be bounded to ensure better QoS performance when compared to OMA. In this

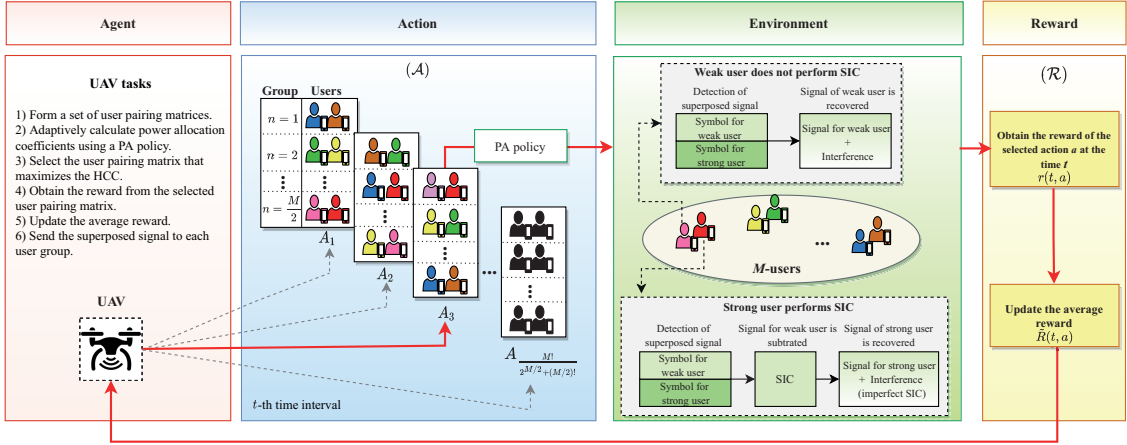


Figure 2.3: Structure of the proposed method.

way, the rate constraint for $U_{1,n}$ can be expressed as:

$$R_{1,n}^{NOMA} \geq R_{1,n}^{OMA} \quad (2.24)$$

$$\log_2 \left(1 + \frac{\rho |h_{1,n}|^2 \alpha_{1,n}}{\rho |h_{1,n}|^2 \alpha_{2,n} + 1} \right) \geq \frac{1}{2} \log_2 (1 + \rho |h_{1,n}|^2). \quad (2.25)$$

Considering $\alpha_{1,n} = 1 - \alpha_{2,n}$ and after some algebraic manipulations, we obtain the following PA coefficient for $U_{2,n}$,

$$\alpha_{n,2} \leq \frac{1}{1 + \sqrt{1 + \rho |h_n|^2}}. \quad (2.26)$$

For $U_{2,n}$, we obtain:

$$R_{2,n}^{NOMA} \geq R_{2,n}^{OMA} \quad (2.27)$$

$$\log_2 \left(1 + \frac{\rho |h_{n,2}|^2 \alpha_{n,2}}{\rho |h_{n,2}|^2 \alpha_{n,1} \zeta + 1} \right) \geq \frac{1}{2} \log_2 (1 + \rho |h_{n,2}|^2), \quad (2.28)$$

$$\alpha_{n,2} \geq \frac{1 + \rho |h_{n,2}|^2 \zeta}{1 + \rho |h_{n,2}|^2 \zeta + \sqrt{1 + \rho |h_{n,2}|^2}}. \quad (2.29)$$

Based on the derived PA coefficient, we limit the power allocated to the strong user, ensuring that the weak user can be served with more power and that the QoS requirements of both users can be satisfied.

To achieve different trade-offs between the two users' data rates, [0] introduced two constant coefficients so that the system can be adjusted to balance the rate between users. Unlike [0], in our analysis, we consider imperfect SIC. By associating (2.26) and (2.29), and inserting the two constant parameters to tune the users' data rates, the optimal PA coefficient can be given by

$$\alpha_{2,n} = \frac{\xi_1}{1 + \sqrt{1 + \rho |h_{1,n}|^2}} + \frac{\xi_2 (1 + \rho |h_{n,2}|^2 \zeta)}{1 + \sqrt{1 + \rho |h_{n,2}|^2}}, \quad (2.30)$$

and

$$\alpha_{1,n} = 1 - \alpha_{2,n}. \quad (2.31)$$

2.3. JOINT USER PAIRING AND POWER ALLOCATION FOR UAV-NOMA SYSTEMS BASED ON MAB PROBLEM

The parameters ξ_1 and ξ_2 denote the two constant parameters to balance the users' data rates of the n -th group. Based on (2.30) and (2.31), the values of the two individual user rates of each group can be tuned by adjusting the parameters ξ_1 and ξ_2 , where $0 \leq (\xi_1, \xi_2) \leq 1$ and $\xi_1 + \xi_2 = 1$.

2.3.5 Reward Design

In the MAB framework, for each TTI t , an action is selected and a reward for that action is obtained. Unlike many RL approaches that describe rewards through discrete values, such as 1 to represent success and 0 to failure, we consider that rewards are designed from continuous values to ensure greater accuracy in our solution. Based on the power coefficient allocation method presented, we can maximize the system data rate without defining the system's instantaneous rate as a reward for a given action. This is possible because the adaptive power coefficient allocation method was formulated to ensure that the rate performance of each user pair is greater or equal when using the OMA technology, even under imperfect SIC. In addition, it is possible to achieve better performance in terms of rate and ensure that more power can be allocated to users with worse channel conditions.

Note that reward achieved by a determined action of user pairing is given by the difference in gain between NOMA and OMA systems. Thus, the main objective of the UAV is to ensure that the system's achievable rate is maximized, achieving the best performance when using NOMA. Therefore, the reward corresponding to the action taken at TTI t is given by the difference between the HCC of NOMA and OMA. The reward function for a given action can be written as

$$r(t, a) = \frac{\left(\frac{Y^N - Y^O}{Y^O}\right) + \varpi}{10}, \quad (2.32)$$

where ϖ denotes the number of constraints of the problem (2.17) that need to be satisfied. In order to normalize the reward function so that the values represent the reward which ranges from 0 to 1, we use the factor 1/10 for a scaling transformation. Thus, the normalization in (2.32) leads to: $r(t, a) \in (0, 1)$. In UCB policy, the objective of the UAV is to maximize the expected reward. Based on this, we represent the expected reward as the average of the rewards obtained per a given action a selected at the time t per the number of times that a was selected. Therefore, for a given reward, $r(t, a)$, the expected reward can be written as

$$\tilde{R}(t, a) \leftarrow \tilde{R}(t, a) + \frac{1}{n_t(a)}(r(t, a) - \tilde{R}(t, a)), \quad (2.33)$$

where $n_t(a)$ denotes the number of times that the action a was selected.

Once the expected value of the reward is calculated, one can define how each action is chosen. Based on the UCB strategy, it is possible to measure the potential of each action through an upper confidence limit of the reward value. An important aspect of this strategy is related to the fact that despite being uncertain about the estimated rewards of actions at each TTI t , the UAV always selects the action that maximizes the upper confidence bound. Therefore, the choice of the action at TTI t can be given by [0]

$$A(t) = \max_{a \in A_N \in \mathcal{A}} \left[\tilde{R}(t, a) + \sqrt{\frac{\phi \ln(t)}{n_t(a)}} \right], \quad (2.34)$$

where ϕ denotes the degree of exploration of UCB strategy and $\sqrt{\phi \ln(t)/n_t(a)}$ denotes the confidence interval. Note that if an action was selected many times, i.e., $n_t(a)$ is large, the confidence interval decreases. As a consequence, the UAV intends to explore other less selected actions. On the other hand, when an actions result in a high reward in the past, i.e., when $R(t, a)$ is large, the UAV exploits this action to achieve the maximal reward.

Algorithm 2 UCB-based Algorithm for User Pairing and Power Coefficient Allocation

Input: Interval T , action set size N according to (2.22), action space \mathcal{A} .

Output: User pairing matrix

- 1: Initialize each action a once
 - 2: Set $n_t(a) = 1, \forall a \in \mathcal{A}$
 - 3: Observe the initial rewards $r(t, a)$ according to (2.32)
 - 4: Calculate the expected reward: $\tilde{R}(t, a) = \frac{r(t, a)}{n_t(a)}$
 - 5: **for** $t = 1 + N$ to T **do**
 - 6: Choose action \hat{a} according to equation (2.34)
 - 7: Based on the user pairing matrix, estimate (2.12) and (2.13) using the available CSI
 - 8: Calculate the reward $r(t, \hat{a})$ according to (2.32)
 - 9: $n_t(\hat{a}) = n_t(\hat{a}) + 1$
 - 10: Update the expected reward $\tilde{R}(t, \hat{a})$ according to (2.33)
 - 11: **end for**
 - 12: **Return:** Chosen the pairing matrix $a \in \mathcal{A}_i, \mathcal{A}_i \in \mathcal{A}$, with $i = 1, \dots, N$.
-

The main structure of the proposed method for power coefficient allocation and user pairing based on the MAB framework is illustrated in Fig. 2.3 and summarized in Algorithm 2. Given a history of rewards and the number of times each action has been selected, the algorithm calculates the upper confidence limit and uses it to decide which action will be selected to maximize the expected reward. Although the action set is initialized once, Algorithm 2 has a running time of $\Theta(T)$. Note that for a large action space \mathcal{A} , the interval T needs to be increased, as the method starts training from time $N + 1$.

2.4 Numerical Results and Discussions

In this section, we provide simulations results to discuss and evaluate the impact of the proposed method. Monte Carlo (MC) simulations are run over 1×10^3 samples. This method is widely used to understand the impact of risk and uncertainty in forecasting models. In our simulations, we consider 1×10^3 MC samples and run the experiments over T for each sample. We stored the rewards that were obtained in each trial and averaged them over MC samples to demonstrate the performance of each algorithm. In the simulations, we consider an Urban-macro cell scenario where the UAV flies at a height $H = 100$ m, the radius of the area where the UAV flies and the mobile users are located are given, respectively, by $r_1 = 20$ m and $r_2 = 500$ m. Moreover, we consider $P_{LoS} = 1$, $\lambda^2 = 1$, and μ and σ are calculated according (2.3) and (2.4), respectively. The target rate of the user with worst channel conditions is $\varepsilon_{1,n} = 0.5$ bits/s/Hz, while the target rate for the user with the best channel conditions is $\varepsilon_{2,n} = 1.0$ bits/s/Hz. We considered that the imperfect

Table 2.1: Simulation parameters.

Parameter	Value
UAV height (H)	100 m
Radius of spherical plan UAV (r_1)	20 m
Region radius of users (r_2)	500 m
Power LoS (P_{LoS})	1 W
Carrier frequency (f_c)	2 GHz
Target rate of the weak user ($\varepsilon_{1,n}$)	0.5 bits/s/Hz
Target rate of the strong user ($\varepsilon_{2,n}$)	1.0 bits/s/Hz
Parameters to balance the users' data rates (ξ_1, ξ_2)	0.7, 0.3
Imperfect SIC coefficient (ζ)	0.05
No of constraints of the problem (2.17) (ϖ)	4
Time interval (T)	1000

SIC coefficient is $\zeta = 0.05$. The parameters to balance the users' rate are $\xi_1 = 0.8$ and $\xi_2 = 0.2$. When the fixed PA scheme is applied at the UAV, it is assumed that the respective power factors to the weak and strong user at the n -th group are $\alpha_{n,1} = 0.85$ and $\alpha_{n,2} = 0.15$, respectively. The simulation parameters are listed in Table 2.1.

2.4.1 Benchmark methods

To compare the performance of the proposed method, we present the results obtained from three algorithms to solve MAB problems: ϵ -greedy, Softmax, and Exp3 [0]. Initially, the quality of each algorithm will be evaluated based on measure regret.

In particular, regret measures the difference between the results obtained from the optimal choice and the one at a given instant of time. In other words, it measures how far the algorithm was from making the best choice. Based on this, one can assume that an algorithm achieves good performance when the cumulative regret value is small. The cumulative regret can be expressed by:

$$\Gamma = \sum_{t=1}^T \max_a [\tilde{R}(:, a)] - E[\tilde{R}(t, a)], \quad (2.35)$$

where $\tilde{R}(:, a)$ is the expected reward when the agent chooses to play a given action a , and $\tilde{R}(t, a)$ is the expected reward when the agent chooses to play a given action $a \in \mathcal{A}$ at a time $t \in T$.

Fig. 2.4 shows the cumulative regret obtained by the method investigated and by the benchmark methods. To make a consistent comparison, we introduce a descriptive analysis of each algorithm.

2.4.1.1 ϵ -greedy Policy

The ϵ -greedy Policy is a strategy to balancing the exploitation-exploration trade-off for solving MAB problems. The ϵ -greedy method performs the best action most of the time, but does random exploration occasionally. In this chapter, we update ϵ in order to decrease as a function of the time. In addition, we consider the number of times that the current action is selected. As the value $n_t(a)$ increases, the epsilon gradually decays as a function of time. Based on this, ϵ decreases the fraction of time in which the algorithm randomly explores the available arms, and exploits those

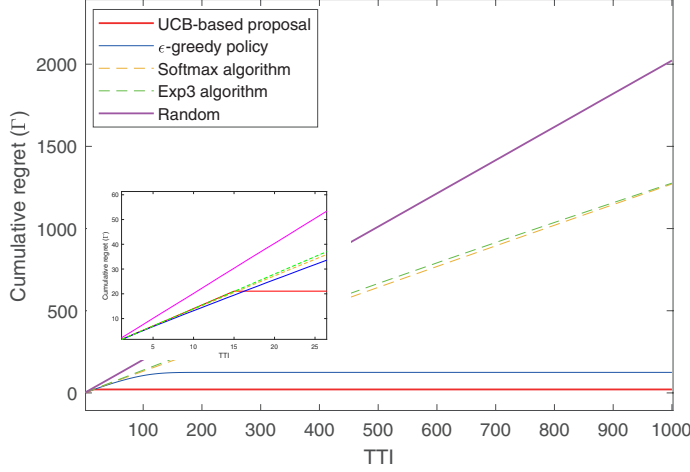


Figure 2.4: Cumulative regret versus TTI for different methods to solve MAB problems ($M = 6$ and $\rho = 35$ dB).

that had the best historical performance the rest of the time. As a result, the algorithm returns high exploratory performance at the beginning and highly exploitation performance at the end. In particular, the probability of choosing an action is described as

$$\text{Action } a = \begin{cases} \text{Randomly } a, & \text{with probability } \epsilon, \\ \max_{a \in \mathcal{A}} [r(t, a)], & \text{with probability } (1 - \epsilon). \end{cases}$$

Algorithm 3 presents the pseudocode for the user pairing matrix selection using ϵ -greedy policy. Note that the ϵ -greedy policy has a running time of $\Theta(T)$, since the choice of the pairing matrix occurs linearly to the interval T .

Algorithm 3 ϵ -greedy policy

Input: Interval T , exploration probability $\epsilon = 0.9$, action set \mathcal{A}
Output: User pairing matrix

- 1: Initialize the auxiliary expected reward $\hat{r}(a) = 0$, $\forall a \in \mathcal{A}$
- 2: **for** $t = 1$ to T **do**
- 3: Set the probability p with a uniform random number
- 4: **if** $p < \epsilon$ **then**
- 5: Choose a random action \hat{a}
- 6: **else**
- 7: Choose a current-best action $\hat{a} = \max[\hat{r}(a)] \forall a \in \mathcal{A}$
- 8: **end if**
- 9: Update $\epsilon = \frac{\epsilon}{1+n_t(a)/T}$ to decrease the exploration of random alternatives
- 10: Calculate the reward $r(t, \hat{a})$ according to (2.32)
- 11: Update $\hat{r}(\hat{a})$ according to $r(t, \hat{a})$
- 12: **end for**

2.4.1.2 Softmax Algorithm

The Softmax algorithm attributes a probability to each action following the Boltzmann distribution [0]. Based on the probabilities, the agent selects an action to exploit. The probability attributed to each action is proportional to its average reward. In other words, when the best action is selected, a higher probability is assigned to her.

The probability of selecting a pairing matrix is given by

$$p_a(t) = \frac{e^{\frac{\hat{R}(t,a)}{\tau}}}{\sum_{i=1}^N e^{\frac{\hat{R}(t,i)}{\tau}}}, \quad a = 1, \dots, N, \quad (2.36)$$

where $p_a(t)$ denotes the probability of selecting action a at the time t , $\hat{R}(t, a)$ denotes the initial empirical expected reward, and τ the temperature parameter that controls the randomness of choice. Algorithm 4 illustrates the pseudocode for the Softmax Algorithm.

Algorithm 4 Softmax Algorithm

Input: Interval T , action space \mathcal{A} , action size N according to (2.22)

Output: User pairing matrix

- 1: Initialize the expected reward $\hat{R}(t, a) = 0, \forall a \in N$
 - 2: **for** $t = 1$ to T **do**
 - 3: Set the temperature $\tau = \frac{1}{\log(t+0.1)}$
 - 4: Set the probability $p_a(t) = \frac{e^{\frac{\hat{r}_a(t)}{\tau}}}{\sum_{j=1}^N e^{\frac{\hat{r}_j(t)}{\tau}}}$
 - 5: Draw the next action \hat{a} randomly according to probabilities $p_a(t), \dots, p_N(t)$
 - 6: Observe the reward $r(t, \hat{a})$ according (2.32)
 - 7: Update the expected reward $\tilde{R}(t, \hat{a})$ according to (2.33)
 - 8: Update the estimated reward $\tilde{r}(t, \hat{a})$
 - 9: **end for**
-

2.4.1.3 Exp3 Algorithm

Exp3 algorithm constructs a weight list for each action based on a specific probability distribution. To formulate the probability, each agent introduces an egalitarianism factor. This factor improves the decision action uniformly at random. When the agent chooses an action, the weight related to the action increases, and then, the greater will be the probability of action chosen again. It is relevant to mention that when the egalitarianism factor is equal to 1, the learned weights are ignored, inducing a complete random exploration.

To describe the Exp3 algorithm, first, we initialize a vector of weights w . Each weight is initialized to equal 1. The egalitarianism factor κ , which controls the algorithm's probability to explore user pairing matrices uniformly at random, was introduced. The Exp3 pseudocode to select the best action in our problem is illustrated in Algorithm 5.

As mentioned above, Fig. 2.4 depicts the cumulative regret of solvers for each TTI. One can see that the UCB-based algorithm finds the best-performing action fast. Once enough data is accumulated, the algorithm exploits the best action, unlike exploring, almost all the time. On the

Algorithm 5 Exp3 Algorithm

Input: Interval T , action space \mathcal{A} , action size N according to (2.22), egalitarianism factor $\kappa = 0.5$.

Output: User pairing matrix.

- 1: Initialize the vector of weights $w_a = 1, \forall a \in \mathcal{A}$
- 2: **for** $t = 1$ to T **do**
- 3: Set the probability $p_a(t) = (1 - \kappa) \frac{w_a(t)}{\sum_{i=1}^N w_i(t)}$
- 4: Draw the next action \hat{a} randomly according to probabilities $p_a(t), \dots, p_N(t)$
- 5: Observe the reward $r(t, \hat{a})$ based on the selected action
- 6: Define the estimated reward $\tilde{R}(t, \hat{a}) = \frac{r(t, \hat{a})}{p_{\hat{a}}(t)}$ for $a = \hat{a}$, and 0 for all other a
- 7: Set $w_{\hat{a}}(t) = w_{\hat{a}}(t) e^{\frac{\kappa \tilde{R}(t, \hat{a})}{N}}$
- 8: **end for**

other hand, the algorithm requires each action chosen once. Thus, for massive sets of actions, the computational complexity increases considerably. The main advantage of ϵ -greedy policy is its ease of understanding and implementation. However, the ϵ -greedy method achieves a low convergence time due to the fixed distribution percentage for exploitation of the actions, independent if it is the best action or the worst one. As a result, the agent acts completely random for a fixed amount of time, and thereafter, exploits the best actions based on the after results.

On the other hand, Softmax Algorithm is not adequate to solve our problem. As can be seen in Fig. 2.4, the low performance occurs because Softmax is not suitable for modifications whose actions have a similar reward. Due to random mobility in our scenario, user pairs can achieve a similar achievable rate as long as they are close to each other. Based on this, we observe that the action space can offer similar rewards and the Softmax algorithm spends a lot of time exploring non-ideal user pairs. As a result, this method accumulates much more regret compared to more complex algorithms. Based on the observations obtained by Softmax, the Exp3 algorithm is also not ideal for solving our problem. Due to the similarity of modifications between the rewards, the Exp3 method will result in a set of bad choices when they look good. The regret obtained by the Exp3 algorithm never stops increasing, and the rewards are generally lower than other algorithms due to the accumulation of bad choices. Like ϵ -greedy, the Softmax and Exp3 algorithms have a $\Theta(T)$ runtime.

In Fig. 2.5, we compare the performance of our proposed method in terms of system throughput. The results represent the maximum achievable rate for the upper limit of data throughput for each TTI. For comparison purposes, we simulate three methods of selecting the pairing matrix. One can see that the result achieved by our scheme quickly coincides with those obtained by exhaustive search, resulting in the selection of the best pairing matrix that maximizes the system rate. Our proposed method can more efficiently explore the best user pairing matrix. On the other hand, ϵ -greedy method needs more computational effort to select the best action, as that method uses random choices when the value ϵ is small. Softmax and Exp3 do not quickly converge on the optimal solution as many of their choices are pairing matrices that have similar rewards and so the algorithms cannot distinguish which is better. Thus, as the probability attributed to bad matrices

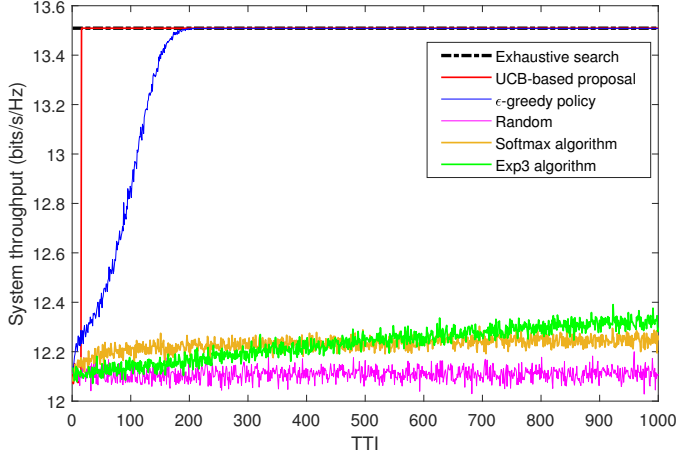


Figure 2.5: System throughput versus TTI for different methods to solve MAB problems ($M = 6$ and $\rho = 35$ dB).

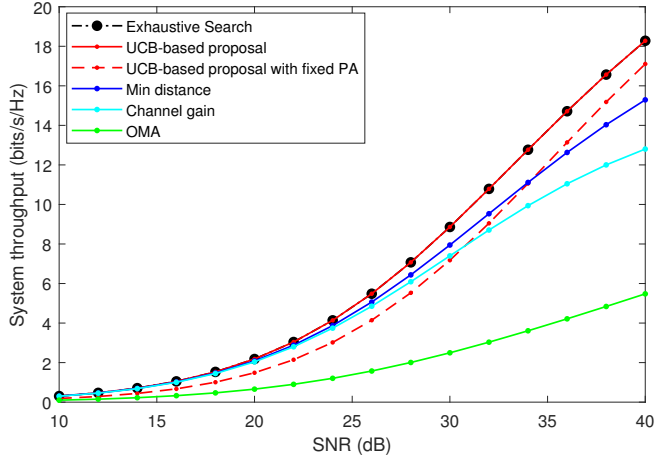


Figure 2.6: System throughput versus SNR for different user pairing methods ($M = 6$, $\varepsilon_{1,n} = 0.5$ bits/s/Hz, and $\varepsilon_{2,n} = 1.0$ bits/s/Hz).

increases, a series of bad choices is performed. As expected, the random method results in a lower performance than the other analyzed methods.

Fig. 2.6 depicts the system throughput for different user pairing methods. As a performance benchmark, we compare our method with three user pairing policies. The method based on minimum distance aims to pair the users who have the shortest distance between them. The method based on channel conditions aims to pair users who have the greatest difference between channel conditions. To the random scheme, the users are randomly pairing. For all schemes, we apply the adaptive power coefficient allocation. In addition, we plot the results for OMA transmission. One can see that the proposed user pairing method provides significant performance improvements

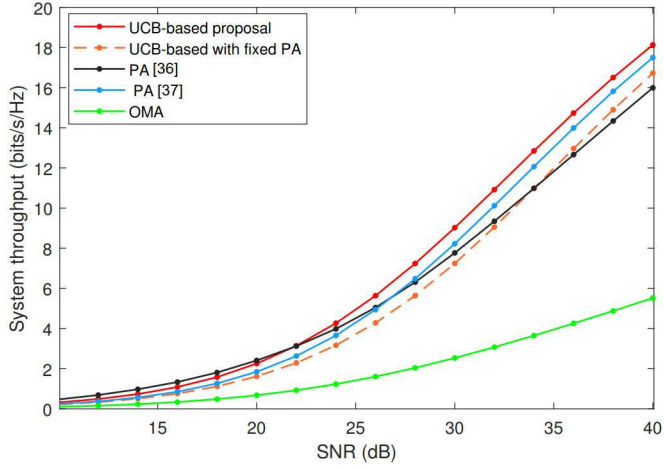


Figure 2.7: System throughput versus SNR: comparison between the power allocation methods ($M = 6$, $\varepsilon_{1,n} = 0.5$, and $\varepsilon_{2,n} = 1.0$).

compared to other user pairing benchmark schemes. Note that all NOMA pairing schemes perform better than OMA, including the random pairing method. This result occurs due to the power coefficient allocation policy presented in this chapter, which ensures that the QoS of each user is greater than or equal to OMA, even under imperfect SIC.

Fig. 2.7 shows system throughput versus SNR. As a performance benchmark, we compare the proposed method with two other adaptive PA methods based on [0] and [0], simulated by considering imperfect SIC. One can see that the proposed method outperforms all other comparative schemes. In [0], the objective is to ensure that the weak user can have their QoS requirements satisfied. By experimenting with the SIC imperfect, we consider that the power allocated to the user who performs the SIC must be sufficient to reach only its QoS requirements. This way, the rate of the user who performs the SIC is never maximized. On the other hand, the other portion of power is provided to the user with worse channel conditions. Thus, the method limits the rate reached by the user who needs to perform the SIC, directly affecting the system's achievable rate. In [0], the strategy was formulated assuming that the weak user rate can be maximized through adaptive PA. One can see that the proposed method outperforms all other comparative schemes. The rate achieved by the proposed method is noticeably greater. By adaptively allocating the power coefficients, it is possible to provide the system more robustness to the fading effects and effectively guarantee that the QoS requirements can be satisfied according to the service to be requested by the user.

Fig. 2.8 investigates the system throughput for different user pairing methods in terms of the number of users. We compare our scheme with two problem-solvers MAB, and with two conventional user pairing methods. One can see that as the number of users increases, the proposed method achieves better performance when compared to the other schemes. For example, for

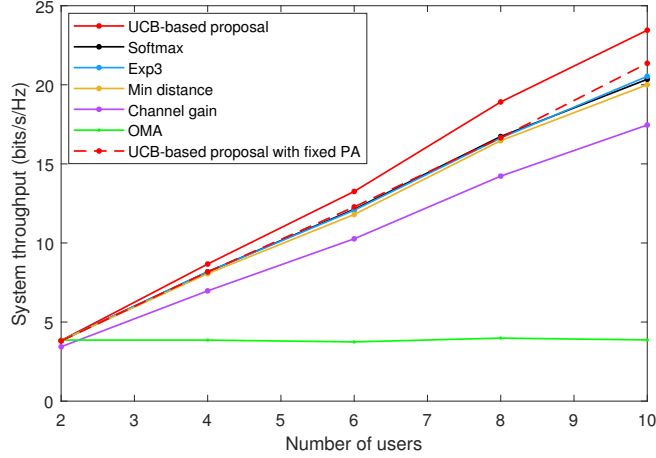


Figure 2.8: System throughput versus number of users for different user pairing method and MAB problem solvers ($\rho = 35$ dB, $\varepsilon_{1,n} = 0.5$, and $\varepsilon_{2,n} = 1.0$).

$M = 8$ the conventional method based on channel gain achieves a rate of 14.22 bits/s/Hz, while the proposed method 18.91 bits/s/Hz, representing a performance gain of 4.69 bits/s/Hz. Softmax and Exp3 show similar results. The achievable rate by these algorithms is approximately 16.62 bits/s/Hz, which represents a performance loss of 2.29 bits/s/Hz when compared to our scheme. For OMA, as the number of users increases, the system throughput slightly decreases. This behavior occurs because network resources must be shared equally for all users, regardless of their respective channel conditions. In addition, even considering the fixed PA, the proposed user pairing method can achieve a higher performance than other benchmark schemes.

2.5 Conclusions

In this chapter, the user pairing and power allocation to maximize the sum rate of the system were investigated. We formulated an optimization problem based on the channel conditions and achievable rate, and we assumed solving it based on the MAB framework. To solve the problem efficiently, we proposed a method that optimizes the user pairing and the allocation of power coefficients. Our method was able to successfully identify the best pairing matrix and selects it more often. This result leads to maximum system throughput, ensuring that users' QoS requirements can be satisfied and the system achievable rate maximized. Simulation results showed that the proposed method outperforms the benchmark schemes.

Aerial IRS in MIMO-NOMA Networks: Fundamentals, Potential Achievements, and Challenges

B. K. S. Lima, A. S. de Sena, R. Dinis, D. B. da Costa, M. Beko, and R. Oliveira, "Aerial Intelligent Reflecting Surfaces in MIMO-NOMA Networks: Fundamentals, Potential Achievements, and Challenges" in IEEE Open Journal of the Communications Society, v. 3, p. 1007-1024, 2022.

3.1 Introduction

The number of connected devices across the world has been foreseen to surpass 75.4 billion by 2025 [0]. This number is related to the diverse services and applications expected for sixth-generation (6G) wireless systems, ranging from smart homes and self-driving cars to interconnected low-power sensors in health, factories, and agriculture. These different network infrastructures will impose stringent requirements to system designers, such as reliable communications, massive connectivity, low latency, low energy consumption, seamless connectivity, and high spectral efficiency. To achieve these heterogeneous requisites, numerous strategies and transmission technologies have been proposed.

The design of appropriate multiple access techniques is crucial for supporting the massive number of devices foreseen for future networks. In particular, Non-Orthogonal Multiple Access (NOMA) has been regarded as a promising candidate technique for next-generation wireless networks due to its potential in achieving high spectral efficiency, massive connectivity, low latency, and user fairness, which can outperform orthogonal multiple access counterparts [0]. By performing Superposition Coding (SC) at the transmitter and Successive Interference Cancelation (SIC) at the receiver, power-domain NOMA enables multiple users to share the same resource block with distinct power levels [0].

In parallel, Unmanned Aerial Vehicle (UAV)s working as aerial Base Station (BS)s have also been identified as enablers of future-generation wireless networks due to their attractive characteristics, such as the ability to perform complex tasks in diverse scenarios and the flexible configuration and deployment in comparison with ground BS. Due to these features, UAVs can

CHAPTER 3. AERIAL IRS IN MIMO-NOMA NETWORKS: FUNDAMENTALS, POTENTIAL ACHIEVEMENTS, AND CHALLENGES

significantly improve the connectivity and coverage range of communication networks, therefore, reducing the need for deploying expensive towers [0]. Unlike terrestrial BSs, the channels between UAV and ground devices have a high probability of being dominated by Line-of-Sight (LoS) links, which can provide significant performance improvement for the communication system.

In order to improve the propagation environment and enhance the signal strength of 6G systems, Intelligent Reflecting Surface (IRS)s have arisen as another promising technology. An IRS is a planar metasurface composed of a large number of reflecting elements that can be controlled via integrated electronics [0]. In general, IRS structures are composed of nearly passive elements that can significantly reduce energy consumption [0]. Thus, IRSs can be more energy-efficient than conventional relaying strategies. Moreover, each reflecting element can be programmed independently to induce distinct phase and amplitude changes, which enables IRSs to reflect and steer impinging waves, ideally, towards any desired direction. This feature, commonly called passive beamforming, can maximize effective channel gains and enhance the reliability of received signals. Signal beams can be formed to weaken the interference coming from non-desirable devices or to avoid information leakage. In the deployment context, the intrinsic features of IRS can be efficiently integrated with other emerging technologies in order to achieve enormous gains for the overall network [0]. Next, we present a comprehensive state-of-the-art related to the IRS technology.

3.1.1 State-of-the-Art

Despite such promising opportunities for the combination of UAV, NOMA and IRS technologies, one must address several technical challenges to effectively use them for each specific networking application. To tackle these problems and challenges, research efforts are being carried out in the context of these technologies. Based on this, a descriptive state-of-the-art of the IRS, UAV, and NOMA techniques is presented as follows.

3.1.1.1 Aerial IRS

In recent years, numerous works have been developed in the field of IRS-mounted on the UAV to demonstrate their role in improving network performance, explore the feasibility of building a controllable and programmable radio environment, and to corroborate the compatibility of deployment with already existing technologies. More specifically, in these works, the integration of IRS on aerial platforms has been extensively investigated due to the numerous benefits compared to Terrestrial Intelligent Reflecting Surface (TIRS) designs, among them flexible deployment and full-angle panoramic reflection (360°). Moreover, in Aerial Intelligent Reflecting Surface (AIRS) only one reflection is sufficient due to LoS, while for terrestrial designs multiple reflections are required due to non line-of-sight (NLoS), which makes the TIRS design relatively large to improve beam propagation. Due to the numerous benefits compared to TIRS, AIRS is a research topic with a wide potential. In particular, a comprehensive overview of the combination of UAV and IRS in [0], where two case studies were carried out to optimize the UAV trajectory, the transmit beamforming, and the IRS passive beamforming. Types of aerial platforms, their operation, control architecture, and types of communication were investigated in [0]. The joint optimization of phase

shifts, placement, and passive beamforming for the AIRS was considered in [0] and [0] to maximize the worst-case signal-to-noise ratio.

When multiple UAVs are deployed to enable AIRS communication, numerous applications and challenges can be explored. In [0], the authors investigated multiple UAVs cooperatively. The authors presented an overview of the UAV swarm-enabled AIRS, including its motivations and competitive advantages compared to terrestrial and aerial IRS, as well as its applications and challenges of designing in wireless networks. In [0], methods to improve the coverage of served users by multiple AIRS were introduced, and the maximum achievable coverage probabilities of the two users were derived and analyzed.

By considering a more realistic modeling channel, where communication systems were characterized by Nakagami-m small-scale fading and inverse-Gamma large scale shadowing, in [0], the authors investigated the delay-limited performance and the outage probability. On the other hand, the compatibility and feasibility of AIRS in a cell-free massive Multiple-Input Multiple-Output (MIMO) network to maximize the user's achievable rate were investigated in [0]. In [0], the authors investigated AIRS to support ultra-reliable low latency (URLLC) communication to tackle the interference caused by the dense network. An AIRS communication system over Terahertz (THz) bands for confidential data dissemination from an access point (AP) towards multiple ground user equipments (UEs) on the Internet-of-Things (IoT) networks was investigated in [0]. In order to analyze the performance of AIRS under high-altitude, a wireless architecture mounted on a high-altitude aerial platform enabled by AIRS was investigated in [0]. The placement and array-partition strategies of aerial-IRS and the phases of IRS elements were jointly optimized. In addition, resource management for transmit power minimization in AIRS HetNets supported by dual connectivity was investigated in [0]. The authors studied the problem of total transmit power minimization by jointly optimizing the trajectory/velocity of each UAV, IRSs' phase shifts, subcarrier allocations, and active beamformers at each BS.

3.1.1.2 UAV with terrestrial IRS

The terrestrial IRS, commonly mounted in building facade, ceilings, and furniture, in UAV-enabled wireless networks have been explored in numerous scientific works [0]. In [0], the authors investigated the coverage IRS-assisted transmission strategy to support multi-user. A transmission protocol was proposed to adjust the transmission strategy for all UAV-user pairs by addressing the IRS elements' allocation and their phase shifts configuration. In order to maximize the sum rate of the network, in [0] the authors investigated multiple UAVs acting as aerial BSs employing NOMA to serve multiple groups. The reflection matrix of the IRS and the NOMA decoding orders among users were optimized. On the other hand, to maximize the achievable rate, the UAV trajectory and IRS's passive beamforming design were optimized in [0].

In order to maximize the network's throughput by jointly optimizing the UAV's trajectory, IoT's energy harvesting time scheduling, and the phase shift matrix, a Simultaneous Wireless Power Transfer and Information Transmission (SWIPT) scheme for IoT devices with support from IRS-aided UAV communication was investigated in [0]. In the same direction, the authors in [0] studied

IRS-assisted UAV for timely data collection in IoT networks. The phase shift of IRS elements, the scheduling of IoT devices transmissions, and the trajectory of the UAV were optimized to maximize the total number of served devices. To minimize the energy consumption, the integration of IRS into UAV-NOMA systems by jointly designing the movement of the UAV, phase shifts of the IRS, power allocation policy at the UAV, and the decoding order was investigated in [0].

To solve the continuous optimization problem with time-varying channels in a centralized fashion, the joint optimization of the power allocation and the phase-shift matrix of an IRS-assisted multi-UAV network was investigated in [0]. Under the presence of multiple nonidentical interference links, the authors in [0] investigated IRS-assisted UAV-enabled vehicular communication systems with infinite and finite blocklength codes. On the other hand, an IRS-assisted UAV physical-layer secure communication for improving the system secrecy rate was investigated in [0] in order to maximize the average worst-case secrecy rate.

3.1.1.3 Terrestrial IRS with NOMA

A comprehensive overview of the recent progress on the integration of TIRSs and NOMA was presented in [0] and [0]. The fundamentals of the two techniques were introduced, and then the basic concepts of the integration of the IRSs and NOMA were discussed. In parallel, a comprehensive discussion of the role of TIRS in MIMO-NOMA systems was presented in [0]. Attractive performance gains to the communication networks were identified, such as higher data rates, improved user fairness, and possibly higher energy efficiency. In [0], the authors optimized the rate performance of the IRS-assisted NOMA system, while ensuring user fairness. By jointly optimizing the active transmit beamforming at the BS and passive beamforming at the IRS, the authors considered the maximizing of the minimum decoding Signal-to-Interference-plus-Noise Ratio (SINR) of all users.

In [0], the authors investigated both downlink and uplink IRS-NOMA network. On the other hand, in [0] the authors investigated an IRS-assisted NOMA downlink system under both continuous and discrete phase-shifting IRS. Then, closed-form expressions for the average required to transmit power, the outage probability, and the diversity order were derived. User pairing and fixed power allocation scheme to enable Reconfigurable Intelligent Surface (RIS)-NOMA network were investigated in [0]. To explore the IRS-NOMA network with Residual Hardware Impairment (RHI) in IoT scenarios, the impact of RHI on the physical layer security performance was investigated in [0]. IRS-enabled MIMO-NOMA networks were investigated in [0] and [0]. More specifically, in [0] a dual-polarized IRS was investigated to improve the performance of dual-polarized massive MIMO-NOMA networks. The proposed scheme alleviates the impact of imperfect SIC and enables users to exploit polarization diversity with near-zero inter-subset interference. On the other hand, a passive beamforming weight at IRS in a MIMO-NOMA network was proposed in [0]. The channel statistics, outage probability, ergodic rate, spectral efficiency, and energy efficiency were derived in closed-form expressions.

3.1.1.4 Machine Learning in AIRS-NOMA Networks

In an effort to effectively exploit IRSs for optimizing wireless systems, solutions based on machine learning methods have been investigated along recent years. In [0], the authors introduced machine learning for user partitioning and phase shifters design in IRS-aided NOMA networks. On the other hand, the authors in [0] explored THz massive MIMO-NOMA with IRS and proposed a smart reconfigurable scheme, which can realize customizable and intelligent communications by flexibly and coordinately reconfiguring hybrid beams through the cooperation between access points and IRS.

In particular, Deep Reinforcement Learning (DRL) and Reinforcement Learning (RL) algorithms, branches of machine learning, have been proposed and applied to solve different problems related to IRS-enabled communication systems. In [0], the authors investigated a single-antenna transmission of IRS-assisted NOMA network and two RL algorithms were proposed to solve the problem caused by the overhead. In [0], two RL-based algorithms were adopted to solve a resource allocation problem in order to minimize the average age-of-information of the users in IoT networks. The freshness of collected data of the IoT devices was improved via optimizing power, sub-carrier, trajectory variables, and the phase shift matrix elements. In [0], the authors investigated an IRS-aided multi-robot served by an AP through the NOMA technique. A dueling double deep Q-network-based algorithm was used to jointly optimize the trajectories, decoding orders, reflecting coefficients, and the power allocation of the AP.

In [0], the authors investigated the application of deep deterministic policy gradient to the AIRS-NOMA network with multiple users. The power allocation of the BS, the phase shifting of the IRS, and the horizontal position of the UAV were jointly optimized. In [0], the authors investigated a DRL-based relay selection scheme for cooperative networks with IRS. A DRL-based framework was proposed in [0] to jointly optimize the IRS and reader beamforming, with no knowledge of the channels or ambient signal in an ambient backscatter communications system aided by an IRS. In [0], the authors investigated a UAV-powered IoT network. A multi-agent DRL approach was proposed to find the optimal collaboration strategy of these energy-limited UAVs that maximizes the accumulated throughput of the IoT network. In [0], a three-step approach based on machine learning was proposed to maximize the sum-rate of all users in an TIRS-aided Multiple-Input Single-Output (MISO)-NOMA network by jointly optimizing the passive beamforming of the IRS, decoding order, and power coefficient allocation, subject to the rate requirements of users.

In order to summarise the main papers presented in this chapter, Table 3.1 presents a list of works that considered the integration of IRS, UAV, NOMA, and MIMO.

3.1.2 Motivation and Contributions

Although there is substantial work on AIRS, MIMO and NOMA networks, there are no works that specifically incorporate AIRS in MIMO-NOMA networks, demonstrating the role of this interaction in terms of its potential achievements. Inspired by the aforementioned considerations, it is provided a comprehensive discussion based on performance analysis related to the aerial IRS in MIMO-NOMA (AIRS-NOMA) networks is provided in order to show the potential improvements

**CHAPTER 3. AERIAL IRS IN MIMO-NOMA NETWORKS: FUNDAMENTALS,
POTENTIAL ACHIEVEMENTS, AND CHALLENGES**

Table 3.1: List of the papers that considered the integration of IRS in future wireless technologies, such as UAV, NOMA, and MIMO. Notions: ✓ → partial discussion. ✓✓ → Detailed discussion. x → no discussion. * → text-based work. ** → text- and performance-based work.

References	Type	AIRS	TIRS	NOMA	MIMO
[0]	*	x	✓✓	x	x
[0]	*	✓	✓✓	✓	✓
[0]	*	x	✓✓	✓	✓
[0]	*	✓✓	x	✓	x
[0]	**	✓✓	✓	x	x
[0]	**	✓✓	x	x	x
[0]	**	✓	✓✓	✓✓	✓
[0]	*	x	✓✓	✓✓	x
[0]	**	x	✓✓	✓✓	✓✓
[0]	**	x	✓✓	✓	x
[0]	*	✓	✓✓	✓	x
Our work	**	✓✓	✓	✓✓	✓✓

and new insights that can be attained due to this promising integration. In particular, the features of the chapter refers to the timeliness and importance of the research topic, and the lack of works in the current literature providing discerning discussions, from an informative guide perspective, on the considered scenario. To provide a consistent guide, the fundamental principles of IRS and its integration into aerial platforms are introduced and, then, the system model of AIRS-NOMA network is presented. Once the system model has been detailed, the potential realizations that AIRS-NOMA systems are capable of offering are discussed, where numerical simulations are presented to demonstrate the achieved performance gain when this setup is employed. The attained results show that this strategy achieves satisfactory results in terms of achievable rate, user fairness, energy efficiency, and coverage area when compared to the TIRS, and aerial decode-and-forward relaying with NOMA (ADF-NOMA) scheme. Furthermore, characteristics of this design are highlighted, as well as potential scenarios, research challenges to inspire future research, and solutions for the design and implementation of AIRS-NOMA networks.

The remainder of this chapter is organized as follows. Section 3.2 describes the fundamentals of AIRS-NOMA technology and the system model under consideration. Section 3.3 presents the potential achievement of the integration of AIRS-NOMA system in comparison with terrestrial deployment. In Section 3.4, we conduct a discussion about research opportunities associated with the integration of AIRS-NOMA networks. Finally, the conclusions are presented in Section 3.5.

3.2 Fundamentals of AIRS and MIMO-NOMA

In this section, we provide a background of the IRS hardware and the control architecture of the IRS mounted on UAV.

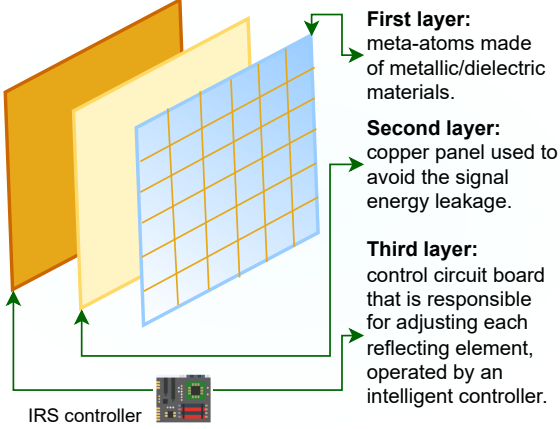


Figure 3.1: Illustration of the IRS structure.

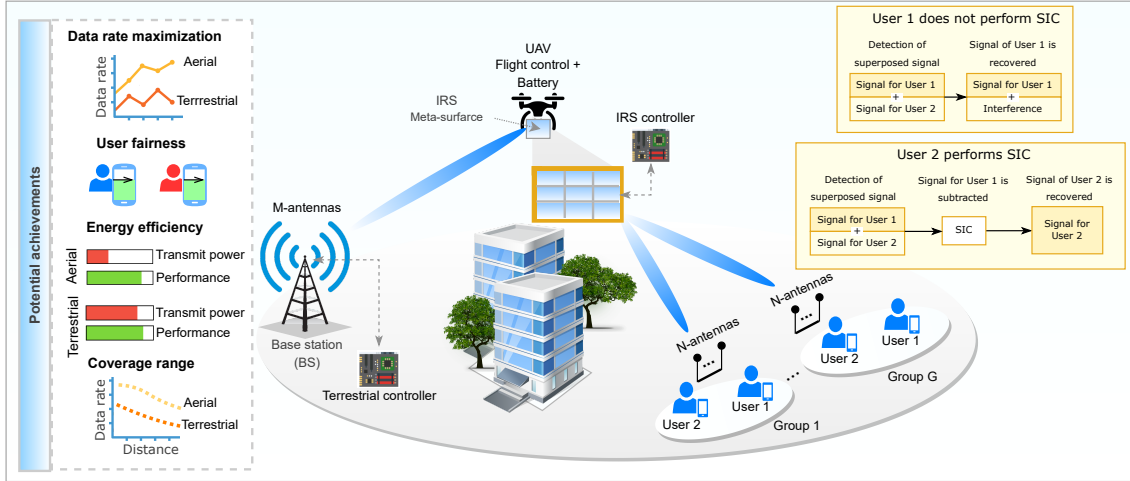


Figure 3.2: Illustration of AIRS in MIMO-NOMA networks (AIRS-NOMA) and potential gains of its integration.

3.2.1 Principles of IRS Structure

Motivated by recent advances in the field of Electromagnetic (EM) materials, IRS frameworks are envisioned as a revolutionary solution for the next generation of wireless communication. IRS is a planar meta-surface made of a large number of low-cost and passive meta-materials. The meta-surface structure is composed of ultra-thin layers of different EM elements, also known as meta-atoms. The key feature of the IRS structure is that each meta-atom can modify the impinging waves in ways that conventional materials cannot. In particular, each meta-atom can be configured in real-time with different phases and amplitudes to dynamically adapt to the fluctuations/characteristics of the environment and reflect the signal in the desired direction. In general, an IRS architecture is composed of at least three layers. The first layer consists of a large number of meta-atoms made of metallic/dielectric materials, which act directly in the process of reflecting the signal. The second layer consists of a copper panel to avoid signal/power leakage. The third layer, also called the control

layer, consists of an electronic board composed of circuits capable of controlling the reflection coefficients (amplitude/phase shift) of each meta-atom, and it is operated by an intelligent controller. In addition, this layer can also act as a gateway to communicate and coordinate with other network components. In order to summarize the aforementioned layers, a generic IRS structure is illustrated in Fig. 3.1.

Unlike structures composed of active materials, a passive metasurface does not require high-energy consumption, complex circuits, and expensive materials [0]. It is noteworthy that, naturally, IRSs support advanced wireless waveforms and operate in Full-Duplex (FD) mode without generating self-interference and noise amplification. In consequence, the IRS framework does not require complex processing to encode and decode the information, which significantly minimizes power consumption and complexity when compared to conventional technologies, such as MIMO beamforming and relaying systems i.e., decode-and-forward (DF) and amplify-and-forward (AF).

3.2.2 Architecture of AIRS

UAVs have been widely used to enhance network performance. Then, the design and benefits of UAVs as aerial BSs in a wireless network were explored in numerous researches [0]. When IRSs are employed in an aerial platform, it is possible to achieve significant performance improvement to the network due to the high flexibility/mobility that UAVs can provide. In addition, if the LoS links between the BS and UAV, and/or UAV and users are blocked by obstacles, the reflecting elements can be accurately adjusted to form virtual LoS links. This solution is one alternative to enhance the coverage area, throughput and capacity both in urban environments and in remote areas, without expensive implementation cost. In particular, a typical control architecture of UAV equipped with IRS can be summarized as follows:

- Terrestrial control: it consists of a processing central composed of radio-frequency transmitters capable of analyzing the environment data, management trajectory information, and communication tasks. Once the meta-surface reflector is made of passive elements, the IRSs do not employ processing functions. Then, the terrestrial unit is responsible to process the sensed data, providing the Channel Status Information (CSI) and the angle of arrival (AoA) between the UAV and users. It is noteworthy that the tasks to obtain data about channel modeling and estimation in the IRS-enhanced UAV networks are extremely difficult due to the dynamic nature of the system. This interesting topic arises as promising research possibilities and will be in-depth explored in challenges and research opportunities in this work.
- UAV Control: it consists of an aerial onboard coupled to the UAV to perform flight and IRS control. Given a set of environment conditions, it is possible to improve the mobility and establishment of the UAV. This unit performs the management of the battery, communication gateway, and arrangement of reflecting elements of the meta-surface. The meta-surface coupled to the UAV can be designed in three-layers, as aforementioned. In addition, the UAV control unit can send and receive pilot symbols to the terrestrial control unit to adjust

the reflection coefficient. Based on the received information, it is possible to optimize the trajectory and the passive beamforming to improve the signal reflection for serving the users.

3.2.3 Aerial IRS in NOMA Networks

Multiple access techniques have an important role to support massive connectivity for next-generation mobile networks. In order to improve the spectral efficiency and the connectivity of AIRS framework, NOMA techniques can be employed [0]. When these technologies are accurately combined, significant performance enhancements can be achieved, such as more flexibility, efficient resource allocation, and signal coverage area.

In particular, IRS technology introduces a new paradigm in NOMA transmission to opportunistically improve the decoding process. This paradigm increases the flexibility by changing the original order of the users' channel gains. In the uplink of conventional NOMA, where the users are sorted according to their channel conditions, the new paradigm allows that the users are sorted according to their data requirements, circumventing the problem of strict dependence on the propagation environment and the location of users. Then, reflecting elements of IRS can be dynamically tuned to either maximize or attenuate the rates by each user according to their specific Quality of Service (QoS). As a result, it is possible to serve a large number of users with stringent communication requirements without requiring more energy and time slots. In addition, the performance of conventional NOMA can be enhanced by the supplementary signal diversity generated by the IRS. The integration of IRS in aerial platforms, and the potential gains of its integration in MIMO-NOMA networks are illustrated in Fig. 3.2.

3.2.4 AIRS-NOMA Networks: System Model

Consider a MIMO-NOMA downlink network where one base station (S) equipped with M antennas communicates with multi-antenna users, equipped with N antennas each, distributed into G groups with two users (D_{gu}) each, where $g = \{1, \dots, G\}$ and $u = 1, 2$, such that $N \leq M$ and $G \leq M$ must be satisfied. It is assumed that there is no direct link between the BS and the users due to severe blockage, then an IRS (R) with K reflecting elements is installed at the UAV to enable the communication between the BS and the users. It is considered that the IRS can forward the impinging signals with high directivity so that a signal beam for the u -th user of the g -th group does not interfere with another signal beam. The mobile users' devices move randomly and independently in a circular cell, with radius r_g . The random waypoint model is implemented to simulate the mobility of the users [0]. During all periods of the mobility process, the users randomly choose a new coordinate and move to it at a constant speed. For each time slot of the mobility process, the new location of the users is calculated. In addition, it is assumed that the UAV continuously flies with a constant velocity and variant elevation Z in a spherical plan of radius r_u . For a given Z , the UAV can fly in the following height range: $Z - r_u \leq z \leq Z + r_u$, where z denotes the instantaneous height.

Based on the downlink power-domain NOMA principles [0], the users' message are superimposed at the BS by SC technique, which consists of superposing the messages of each user by

assigning different power coefficients between the users. Then, the BS sends the superimposed signal in the direction of the AIRS. More specifically, the transmitted signal can be written as

$$\mathbf{x} = \sum_{g=1}^G \sum_{u=1}^2 \alpha_{gu} s_{gu} \in \mathbb{C}^{M \times 1}, \quad (3.1)$$

where s_{gu} denotes the message of interest of the u -th user in the g -th group, and α_{gu} denotes their respective power allocation coefficient with $\alpha_{gu} > 0$ and $\sum_{u=1}^2 \alpha_{gu} \leq 1$. The channel gain matrices between $S \rightarrow R_r$ and $R_r \rightarrow D_{gu}$ can be expressed, respectively, as

$$\mathbf{H}_{SR_r} = \sqrt{\beta_{SR_r}} \mathbf{W}_{SR_r} \in \mathbb{C}^{M \times K}, \quad (3.2)$$

and

$$\mathbf{H}_{R_r D_{gu}} = \sqrt{\beta_{R_r D_{gu}}} \mathbf{W}_{R_r D_{gu}} \in \mathbb{C}^{K \times N}, \quad (3.3)$$

where $\beta_a = \beta_0 d_a^{-\nu}$, $a \in \{SR_r, R_r D_{gu}\}$ denotes the large-scale average channel power gain with $r = 1, \dots, K$, in which β_0 denotes the average channel power gain at the reference distance $d_0 = 1$ m, d_a denotes the distance between $S \rightarrow R_r$ and $R_r \rightarrow D_{gu}$, and ν denotes the pathloss exponent. \mathbf{W}_a denotes the small-scale fading, modeled by the Nakagami- μ distribution, as in [0]. Without loss of generality, the complex channel gain matrices \mathbf{W}_{SR_r} and $\mathbf{W}_{R_r D_{gu}}$ can be expressed as

$$\mathbf{W}_{SR_r} = \begin{bmatrix} |g_{SR_1,1}|e^{j\omega_{1,1}} & \dots & |g_{SR_1,M}|e^{j\omega_{M,1}} \\ |g_{SR_2,1}|e^{j\omega_{1,2}}, & \dots, & |g_{SR_2,M}|e^{j\omega_{M,2}} \\ \vdots & \ddots & \vdots \\ |g_{SR_K,1}|e^{j\omega_{1,K}}, & \dots, & |g_{SR_K,M}|e^{j\omega_{M,K}} \end{bmatrix}, \quad (3.4)$$

and

$$\mathbf{W}_{R_r D_{gu}} = \begin{bmatrix} |g_{R_1 D_{gu},1}|e^{j\omega_{1,1}} & \dots & |g_{R_1 D_{gu},N}|e^{j\omega_{N,1}} \\ |g_{R_2 D_{gu},1}|e^{j\omega_{1,2}}, & \dots, & |g_{R_2 D_{gu},N}|e^{j\omega_{N,2}} \\ \vdots & \ddots & \vdots \\ |g_{R_K D_{gu},1}|e^{j\omega_{1,K}}, & \dots, & |g_{R_K D_{gu},N}|e^{j\omega_{N,K}} \end{bmatrix}^H, \quad (3.5)$$

where $|g_{a,m}|$ and $\omega_{m,r} \in [0, 2\pi)$ are, respectively, the magnitude and phase angle between m -th transmission antenna of the BS and the r -th reflecting element of the AIRS, with $m = 1, \dots, M$.

Since a controller connected to the IRS can smartly adjust the IRS's phase shifts to assist the NOMA transmission, the properties of the AIRS can be characterized via the following diagonal phase-shift matrix

$$\boldsymbol{\Theta} = \text{diag}[\kappa_1 e^{j\theta_1}, \kappa_2 e^{j\theta_2}, \dots, \kappa_K e^{j\theta_K}] \in \mathbb{C}^{K \times K}, \quad (3.6)$$

where $\theta_K \in [0, 2\pi)$ denotes the phase-shift occurring at r -th element of the AIRS, and $\kappa_K \in [0, 1)$ denotes the fixed amplitude reflection coefficient. In particular, it is very expensive to realize infinite-resolution phase shifters due to hardware limitations. As a result, the complexity to perform the phase-shift increases considerably [0]. In particular, the end-to-end (e2e) channel matrix from the BS to the u -th user in the g -th group with aid of the AIRS is given by

$$\tilde{\mathbf{H}}_{gu} = \mathbf{H}_{SR_r} \boldsymbol{\Theta} \mathbf{H}_{R_r D_{gu}} \in \mathbb{C}^{M \times N}. \quad (3.7)$$

The signal received at the u -th user in the g -th group can be expressed as

$$\mathbf{y}_{gu} = \sqrt{P_S} \tilde{\mathbf{H}}_{gu} \mathbf{x} + \mathbf{w}_{D_{gu}}, \quad (3.8)$$

where P_S denotes the transmit power of the BS and $\mathbf{w}_{D_{gu}} \sim \mathcal{CN}(0, \sigma^2)$ denotes the additive Gaussian noise (AWGN).

Analogous to [0], it is considered that the IRS can reflect the signal to a desired point with high directivity and that the clusters are separated far enough. Thus, the clusters have a non-overlapping reflection angle and the interference arriving at a specific cluster from other clusters will be extremely small i.e., it can be neglected. On the other hand, to eliminate the inter-group interference, the signal reception is designed by adopting a zero-forcing receiver. More specifically, the detection matrix can be constructed as follows

$$\hat{\mathbf{H}}_{gu} = [\tilde{\mathbf{H}}_{gu}^H \tilde{\mathbf{H}}_{gu}]^{-1} \tilde{\mathbf{H}}_{gu}^H \in \mathbb{C}^{M \times N}. \quad (3.9)$$

Given this zero-forcing receiver, the received signal at each user is decoupled from each other. Then, the effective channel power gain between the BS and the u -th user in the g -th group with the aid of the AIRS is given by

$$\mathbf{H}_{gu} = \hat{\mathbf{H}}_{gu} (\hat{\mathbf{H}}_{gu})^H \in \mathbb{C}^{M \times M}. \quad (3.10)$$

Since the symbols will be decoded from the beam that is equivalent to the index gg of the channel power gain matrix, the highest effective channel gain, the selected beam is denoted as $g\bar{g}$. Then, $[(\mathbf{H}_{gu})_{g\bar{g}}]^{-1}$ denotes the effective channel gain observed by the u -th user in the g -th group.

Based on available CSI, the users are ordered according to their effective channel gains. Without loss of generality, we assume that the user D_{g1} has the weakest channel gain, while user D_{g2} experiences the greatest channel conditions. Then, higher power must be allocated to the user with the worst channel conditions in order to ensure that its data requirements can be achieved, which means that $\alpha_{g1} > \alpha_{g2}$. After the user ordering operation, the e2e SINR for the weakest user in the g -th group to decode its message is given by

$$\gamma_{g1} = \frac{\bar{\gamma} \tilde{h}_{g1} \alpha_{g1}}{\bar{\gamma} \tilde{h}_{g1} \alpha_{g2} + 1}, \quad (3.11)$$

where $\tilde{h}_{g1} = [(\mathbf{H}_{g1})_{g\bar{g}}]^{-1}$ denotes the effective channel gain observed by the weaker user in the g -th group, $\bar{\gamma} = P_S / \sigma^2$ denotes the transmit Signal-to-Noise Ratio (SNR).

Under the assumption of imperfect SIC, the e2e SINR observed by the stronger user in the g -th group is given by

$$\gamma_{g2} = \frac{\bar{\gamma} \tilde{h}_{g2} \alpha_{g2}}{\bar{\gamma} \tilde{h}_{g2} \alpha_{g1} \epsilon + 1}, \quad (3.12)$$

where $\tilde{h}_{g2} = [(\mathbf{H}_{g2})_{g\bar{g}}]^{-1}$ denotes the effective channel gain observed by the strongest user in the g -th group, $\epsilon \in [0, 1]$ is the coefficient of imperfect SIC.

The instantaneous achievable rate of the weaker user in the g -th group can be expressed as

$$R_{g,1} = \log_2(1 + \gamma_{g1}). \quad (3.13)$$

Table 3.2: Simulation parameters.

Parameter	Value
Number of users per group (U)	2
Group cell radius (r_g)	5 m
UAV height (z)	($20 - r_u \leq z \leq 20 + r_u$) m
Spherical plan radius of UAV (r_u)	2 m
Number of groups (G)	3
Number of transmit antennas (M)	4
Number of receiver antennas (N)	4
Number of reflecting elements (K)	20
Path loss exponent (ν)	2.2
PA coefficient for weak user (α_{g1})	0.7
PA coefficient for strong user (α_{g2})	0.3
Nakagami parameter (μ)	2.5
Average channel power gain (β_0)	500
Coefficient of imperfect SIC (ϵ)	0, 0.005, 0.01
Distance between BS and AIRS (d_{SR})	($98 \leq d_{SR} \leq 102$) m
Distance between AIRS and group 1 ($d_{RD_{1u}}$)	($20 - r_g \leq d_{RD_{1u}} \leq 20 + r_g$) m
Distance between AIRS and group 2 ($d_{RD_{2u}}$)	($50 - r_g \leq d_{RD_{2u}} \leq 50 + r_g$) m
Distance between AIRS and group 3 ($d_{RD_{3u}}$)	($100 - r_g \leq d_{RD_{3u}} \leq 100 + r_g$) m

The e2e instantaneous achievable rate of the stronger user in the g -th group is given by

$$R_{g,2} = \log_2(1 + \gamma_{g2}). \quad (3.14)$$

In the next section, we provide in-depth discussions and significant numerical results to support the gains achieved by AIRS in MIMO-NOMA networks.

3.3 Potential achievements of Aerial IRS-aided MIMO-NOMA Networks

In this section, numerical simulations to emphasize the performance gain when AIRS is applied in MIMO-NOMA wireless networks are presented. More specifically, it is discussed and highlighted the performance gain in terms of sum-rate, user fairness, energy efficiency, and coverage range. Performance metrics are evaluated by extensive Monte Carlo (MC) simulations that corroborate the advantages of implementing IRS in aerial scenarios.

Taking into account the three-dimensional spatial movement of UAV, we design a downlink AIRS-NOMA network system with G groups with two mobile users, denoted by user 1 and user 2, respectively. In particular, it is assumed that each node in the network is equipped with multiple antennas and there is no direct link between the BS and the users due to strong fading and physical obstacles. The distance between the BS and the center of the cell of the group 1, group 2, and group 3 is, respectively, 100 m, 150 m, and 200 m. When TIRS is deployed, it is assumed that the TIRS is positioned at 80 m from the BS. The users of each group are randomly distributed in a cell of radius $r_g = 5$ m, and classified according to their channel conditions. Without loss of generality, centralized design is employed in our simulations. Unless otherwise specified, the simulation parameters follow the Table 3.2.

3.3. POTENTIAL ACHIEVEMENTS OF AERIAL IRS-AIDED MIMO-NOMA NETWORKS

It is noteworthy that no optimization method is used to configure the reflecting elements in this chapter. Then, the phase shift is randomly and uniformly generated in $[0, 2\pi]$. From a deployment perspective, we assume that the network control structure follows the centralized deployment, where the AIRS is controlled by a terrestrial central controller installed at the BS. By using centralized deployment, all processing tasks are employed by the BS, such as estimation protocols. In addition, we consider that the terrestrial controller is able to estimate the CSI of all propagation links. As a benchmark performance, we compare our results with Terrestrial IRS-aided MIMO-NOMA Networks (TIRS-NOMA) presented in [0] without considering massive MIMO and direct link between the BS and users, and with conventional relaying ADF-NOMA method.

3.3.1 Data Rate Maximization

To demonstrate the potential of AIRS-NOMA, we first discuss the performance gains in terms of sum-rate for each user group. Then, we compare the obtained results with TIRS-NOMA and ADF-NOMA. According to the NOMA principles, the BS sorts the users based on their respective channel conditions so that more power can be allocated to the user with the worst channel conditions. Without loss of generality, it is assumed that user 1 has unfavorable channel conditions and requires a low data rate. On the other hand, user 2 has better channel conditions and requires a high data rate. At the BS, the signals of the two users are superimposed with different power levels by the SC technique and transmitted to the AIRS, which passively reflects signals from BS to users. In the receiver, the users can employ SIC to decode the transmitted messages.

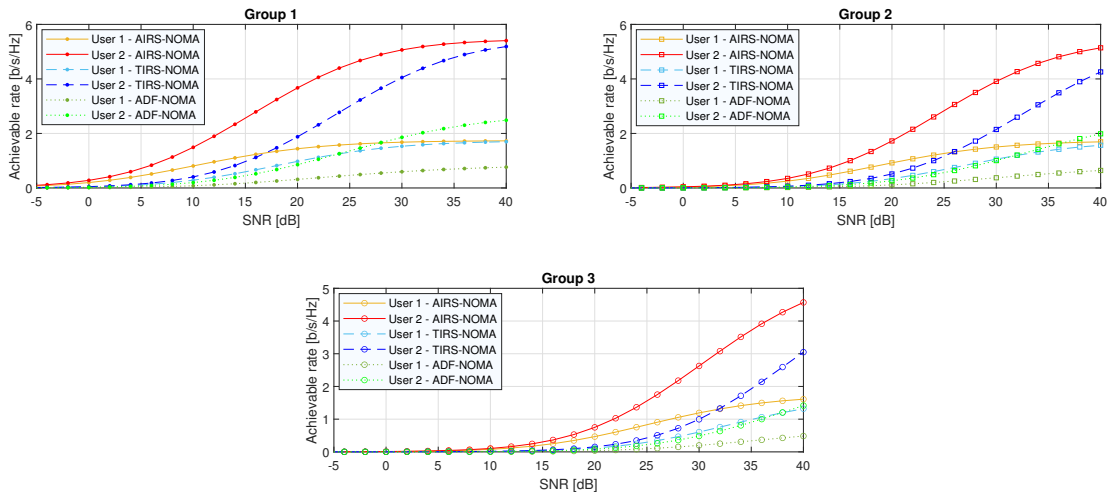


Figure 3.3: Achievable rate versus the transmit SNR for each user group. ($K = 20$, $\alpha_{g1} = 0.7$, $\alpha_{g2} = 0.3$, and $\epsilon = 0.01$).

Fig. 3.3 presents the achievable rate versus the transmit SNR for both weak and strong user for each group of users. For comparison, TIRS and ADF-NOMA deployment are applied. One can observe that for all groups the AIRS outperforms the TIRS deployment. This performance is related to the coverage holes and blind spots that can occur during the transmission process, and virtual LoS links might not be formed even with the aid of the IRS. On the other hand, the UAV placement can be adjusted to maintain LoS links. Once the favorable UAV placement is found, one

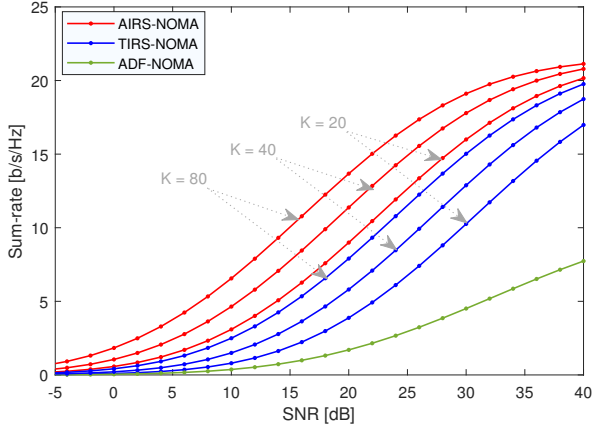


Figure 3.4: Sum-rate versus transmit SNR for different number of reflecting elements. ($\alpha_{g1} = 0.7$, $\alpha_{g2} = 0.3$, and $\epsilon = 0.01$).

can adjust the IRS reflection parameters to reflect the signal in the desired direction. On the other way, the UAV can remain static to minimize energy consumption until it is necessary to adjust its position again to ensure the LoS component. However, one can also see that the greater is the distance between AIRS and a group of users, the worse is the rate achieved by this group. This reinforces the need to improve propagation in far-field scenarios. In particular, the integration of IRS in the aerial platform can provide more flexibility to assist terrestrial users. In addition, the performance achieved by using ADF-NOMA as relaying protocol is evidently low when compared to both AIRS and TIRS schemes.

In addition, Fig. 3.4 illustrates the average sum-rates versus SNR for deployment with AIRS-NOMA, TIRS-NOMA, and without IRS for a different number of reflecting elements of the IRS (K). One can observe that the performance of the sum-rate enhances as the number of reflecting elements increases. In particular, higher reflecting array gain can be explored to maximize the effective channel gain and improve the reliability of the received signal. When IRS is installed at the UAV, one can achieve better service quality to the overall network due to the capability to maintain the LoS links even in an environment with a high probability of link obstruction. As a result, significant benefits in sum-rate gain can be achieved. For example, when the SNR is 20 dB, the TIRS-NOMA with $K = 80$ achieves a performance of 7.9 bits/s/Hz, while AIRS-NOMA with $K = 80$ can reach 13.6 bits/s/Hz, that represents a performance gain of approximately 5.7 bits/s/Hz. We also observe that when IRS is employed, the performance gain is more pronounced than conventional ADF-NOMA at AIRS-NOMA transmission is a promising framework.

Fig. 3.5 presents the impact of imperfect SIC factor through the sum-rate of the system. As a performance comparison, we vary ϵ and compare the performance between AIRS-NOMA, TIRS-NOMA, and ADF-NOMA schemes. One can see that the errors due to imperfect SIC can cause severe damage to the system. On the other hand, as expected, when $\epsilon = 0$ is employed the performance in terms of sum-rate is expressively better. For example, when the SNR is 30 dB, the AIRS-NOMA scheme achieves a sum-rate of 19.23 b/s/Hz for $\epsilon = 0$, but with $\epsilon = 0.05$ the sum-rate obtained is 12.44 b/s/Hz, which represents approximately a loss of 6.78 b/s/Hz.

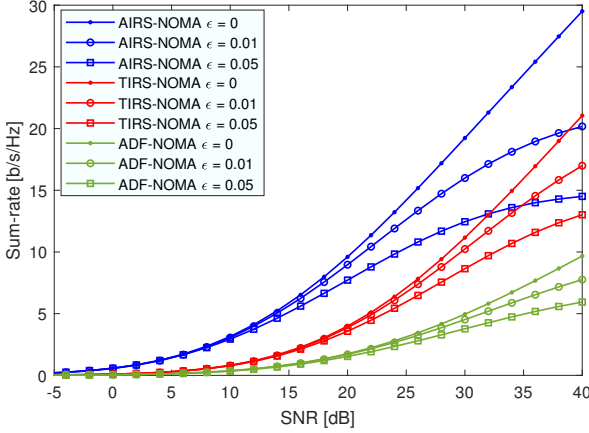


Figure 3.5: Sum-rate versus transmit SNR for different coefficients of imperfect SIC (ϵ). ($K = 20$, $\alpha_{g1} = 0.7$, $\alpha_{g2} = 0.3$).

3.3.2 User Fairness

Since the NOMA technique is used as the transmission scheme, the spectrum's usage efficiency can be improved by superimposing the users' signals, exploring the same resource block. By assuming that the users subscribe to the same traffic service that requires a minimum data rate to be acceptably provided, one can guarantee that all users are served equally throughout the communication process by the efficient Power Allocation (PA) method. By dynamically allocating power coefficients, it is possible to provide a portion of power for the user with a better conditions channel, called user 2, which performs the SIC correctly. Meanwhile, the remaining power is applied to maximize the weak user's rate, called user 1. More details about the dynamic power allocation strategy can be found in [0].

Fig. 3.6 depicts the achievable rate for each user at the g -th group versus transmit SNR for different PA methods. For comparison purposes, we employ both fixed and the adaptive PA policy [0]. It is interesting to observe from Fig. 3.6 that the adaptive PA can significantly improve the rate performance of the user with the worst channel conditions. However, the main disadvantage of this approach is that the performance of the user with better channel conditions is degraded. Since the main idea of this strategy is performing a balance between users' rates, the strong user can be penalized in order to guarantee that the weak user could reach the same service traffic. On the other hand, one can observe that by the adequate deployment of IRS, it is possible to significantly improve the network performance. By exploring the UAV features, AIRS achieves better performance than terrestrial deployment. Compared with the rate performance of groups 1 and 2, group 3 presents a lower performance due to the distance in relation to AIRS, but the result obtained is expressively superior to the result obtained by TIRS-NOMA. This result indicates that AIRS-NOMA systems can provide user fairness while bringing high-performance to the system in comparison with terrestrial framework.

In Fig. 3.7, the relation between resource allocation fairness in terms of transmit SNR is investigated. The Jain's fairness index, given by $J_g = (R_{g,1} + R_{g,2})^2 / [2((R_{g,1})^2 + (R_{g,2})^2)]$, is

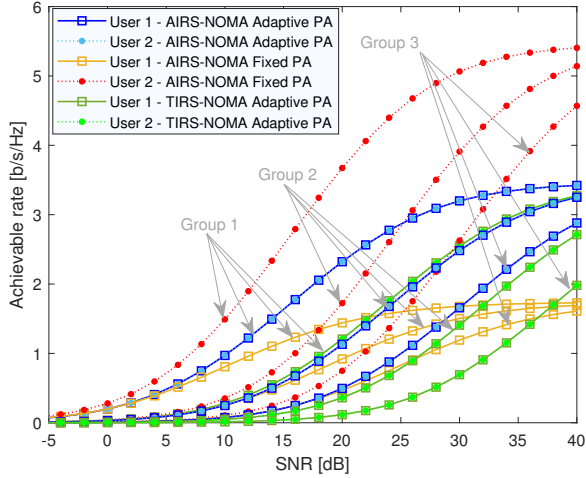


Figure 3.6: Achievable rate versus transmit SNR for AIRS-NOMA system and TIRS-NOMA system with adaptive PA and fixed PA. When the fixed PA scheme is applied, it is assumed that the power allocation coefficients applied to the users 1 and 2 of the g -th group are, respectively, ($K = 20$, $\alpha_{g1} = 0.7$, $\alpha_{g2} = 0.3$, and $\epsilon = 0.01$).

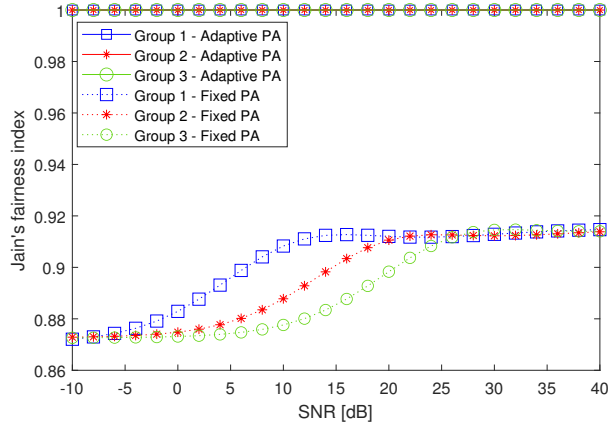


Figure 3.7: Jain's fairness index versus SNR for different adaptive PA schemes. When the fixed PA scheme is applied, it is assumed that the power allocation coefficients assigned to the users 1 and 2 of the g -th group are, respectively, ($K = 20$, $\alpha_{g1} = 0.7$, $\alpha_{g2} = 0.3$, and $\epsilon = 0.05$).

used as a fairness metric. As a performance benchmark, the conventional fixed PA policy has been adopted. One can see that the adaptive PA can provide optimal user fairness for all SNR values, ensuring that all network users are served equally throughout the communication process. If all users get the same rate amount, then the fairness index is 1 and the system is totally fair. On the other hand, for fixed PA, there is a disparity between rates and, consequently, the fairness index decreases. The adaptive strategy favors all the users of the system, ensuring fair rate resources independently of channel conditions.

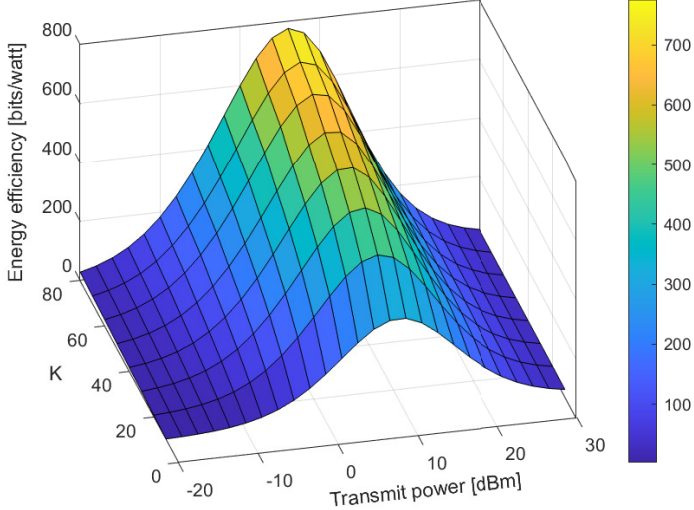


Figure 3.8: Energy efficiency of the system versus the number of reflecting elements of the AIRS and the transmit power for AIRS-NOMA systems. ($\alpha_{g1} = 0.7$, $\alpha_{g2} = 0.3$, and $\epsilon = 0.01$).

3.3.3 Energy Efficiency

In the literature, it has been proved that the NOMA technique can significantly increase the spectrum and energy efficiency of the communication networks due to the capability to allow multiple users to share the same resources. In parallel, studies in the field of IRS prove that this promissory technology can improve the data rates of users without requiring more transmit power, but only smartly adjusting the reflecting elements to increase the channel gains. Since a centralized IRS deployment is considered, the energy required by IRS is only directed for the reconfigurability of reflecting elements, which can be employed by low-power electronics. However, considering the hardware constraints, it is not always feasible to deploy a centralized IRS when the number of reflecting elements is large. To achieve a trade-off between the number of reflecting elements and energy consumption, the features of IRS can be integrated into the UAV in order to strengthen the received signal at the ground users due to the high operating altitude of the UAV which increases the coverage area through efficient dynamic 3D beamforming.

A practical demonstration of the integration of the IRS into aerial platforms for performance gains in terms of the rate achieved for the radiated power at the specific time instant, can be seen in Fig. 3.8, which is defined as $B \cdot \tilde{R}_{gu}/P_{total}$, where B denotes the bandwidth, \tilde{R}_{gu} denotes the system's sum rate, and P_{total} denotes the transmit power [0]. In particular, the energy efficiency performance for different number of reflecting elements and transmit power levels¹. One can observe that the greater the number of reflecting elements, the higher the energy efficiency that the AIRS-NOMA system is able to achieve. It is noteworthy that the energy neutrality in the elements of the IRS is assumed. In addition, one can see that there exists a trade-off between the number of

¹Please note that certain characteristics of the UAV were not considered during the calculation of energy efficiency, as this area of study is quite extensive. Consequently, future research should delve into the specifics of UAV types, such as fixed-wing or multi-rotor, along with attributes related to energy consumption, autonomy, and vibrations transmitted to the IRS.

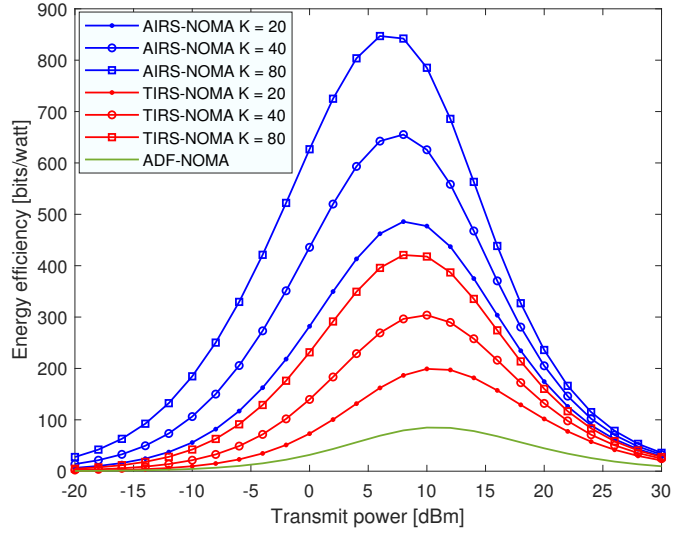


Figure 3.9: Energy efficiency versus transmit power for different number of reflecting elements. ($\epsilon = 0.01$).

reflecting elements, K , and transmit power levels to maximizes energy efficiency.

Based on the previous result, we investigate the performance of AIRS-NOMA for different number of reflecting elements and different framework scenarios. Specifically, Fig. 3.9 presents the energy efficiency curves versus transmit power for different number of reflecting elements and TIRS-NOMA and ADF-NOMA counterpart schemes. One can observe that the AIRS-NOMA systems have the ability to achieve enhanced energy efficiency compared to terrestrial and conventional deployment. By exploring aerial mobility, we can achieve higher performance gains with less transmit power. One can see the significant gain in performance when K increases due to the passive energy-consumption nature. In this way, the signal beam can be improved without the need of excessive energy cost. For example, when the transmit power is 10 dBm, the AIRS-NOMA with $K = 20$ reaches a performance of 477 bits/watt, while with $K = 80$, the energy-efficiency achieves a performance of 785 bits/watt, that represent a gain performance of 308 bits/watt. In particular, to contribute with this good performance, there is an energy consumption compensation between the IRS and UAV. The UAV does not need to be in constant movement, as the IRS can form virtual LoS Links. On the other hand, when the IRS cannot guarantee this link due to the dynamic nature of ultra-dense environments, the UAV can dynamically changes position to guarantee the LoS link. Then, the UAV can remain static until further intervention is required.

In order to show how energy-efficient AIRS can become in scenarios where the IRS is not neutral and with perfect and imperfect SIC, Fig. 3.10 presents the energy efficiency curves for energy neutral and energy non-neutral scheme with perfect and imperfect SIC. One can observe the impact caused by the imperfect SIC. For example, when the transmit power is 10 dBm and the neutral power consumption is considered, the AIRS-NOMA with $\epsilon = 0.05$ can reach a performance of 386.3, bits/watt, while with $\epsilon = 0$, the energy efficiency increase up to 477 bits/watt, that represent a performance gain of approximately 90.68 bits/watt. In addition, we compare the obtained results

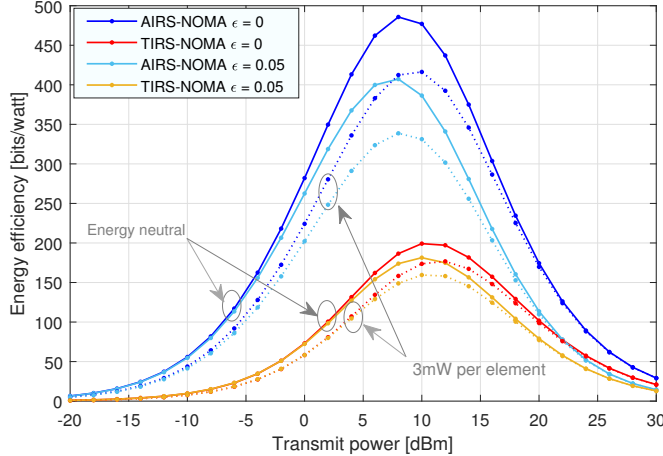


Figure 3.10: Energy efficiency versus transmit power for AIRS-NOMA and TIRS-NOMA systems. Non-neutral power consumption and imperfect SIC are considered. ($K = 20$, $\alpha_{g1} = 0.7$ and $\alpha_{g2} = 0.3$).

with TIRS-NOMA framework. Due to the non-neutral power consumption of the circuit, one can see that the energy efficiency decrease. However, the performance obtained by AIRS-NOMA scheme is significantly superior to obtained using TIRS-NOMA scheme. It is noteworthy that if the energy neutrality assumption can be satisfied, the energy efficiency will significantly be increased as the number of reflecting elements increase.

3.3.4 Coverage range

It was discussed that the IRS can form virtual LoS links by adjusting the reflecting elements, but when these links cannot be formed due to obstructions, the UAV can be repositioned to help establish high data rates and reliable transmissions. As a result, users' service requirements can be met, leading to good network performance. In particular, Fig. 3.11 illustrates the scenario used to analyze the performance in terms of coverage range. To investigate the impact of AIRS-NOMA scheme, Fig. 3.12 presents the sum-rate versus distance for different IRS deployments and the conventional ADF-NOMA relaying protocol. We set the transmit SNR to $\rho = 30$ dB and assume that the distance between the BS and AIRS is d_{SR} , and the distance between the BS and the center of the cell of the group 1, group 2, and group 3 are, respectively, 100 m, 150 m and 200m. One can observe that the performance of AIRS-NOMA decreases when the distance between the users increases. In contrast to the TIRS-NOMA scheme, the AIRS-NOMA scheme has more potential to establish strong LoS links with the users due to the relatively higher altitude of UAV, thus reducing the coverage holes or blind spots with them. For example, when the distance between the BS and the AIRS is 130 m, the TIRS-NOMA scheme can reach a sum-rate of 8.59 b/s/Hz, while with the AIRS-NOMA system, the sum-rate increases up to 15.17 b/s/Hz, which represents a gain of 6.57 b/s/Hz. In addition, when $d_{SR} = 120$ m the AIRS-NOMA outperforms conventional ADF-NOMA with a performance gain of approximately 11.5 b/s/Hz. This result clearly demonstrates that, by exploiting the AIRS capabilities, the MIMO-NOMA scheme can effectively extend the coverage

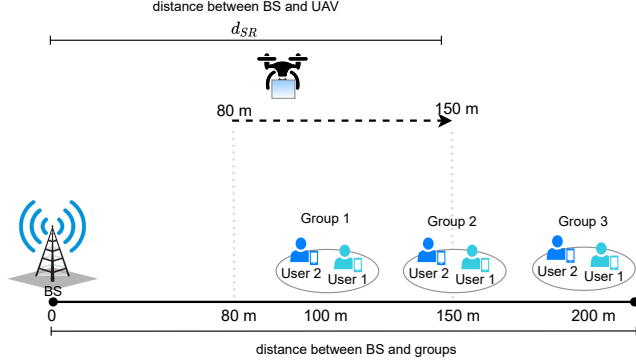


Figure 3.11: Centralized design: Illustration of the scenario used to simulate the results in Figure 3.12.

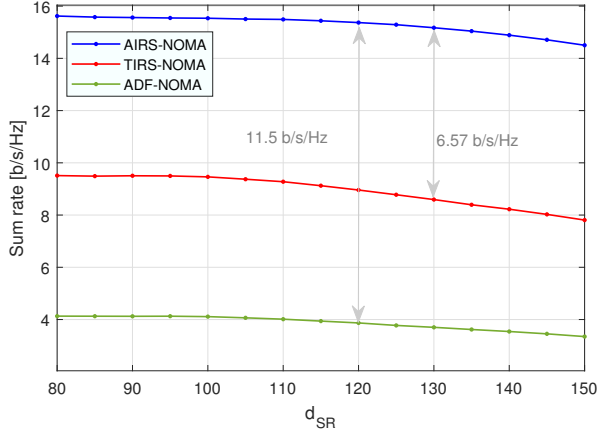


Figure 3.12: Sum-rate versus distance for AIRS-NOMA, TIRS-NOMA, and ADF-NOMA deployments. ($\bar{\gamma} = 30$ dB, $K = 20$, and $\epsilon = 0.01$).

Table 3.3: Comparison of AIRS-NOMA with other frameworks.

Framework	Advantage	Drawback
AIRS-NOMA	Rate maximization User fairness High energy efficiency Coverage range Low hardware cost	High sensitivity to channel Uncertainty due to the fast mobility Battery UAV
TIRS-NOMA	User Fairness Low hardware cost	Limited coverage range Difficult to estimate CSI
ADF relay	Decodes the signal and forwards a regenerated copy	High energy consumption Low data rate

area.

To summarize the main difference between AIRS-NOMA, TIRS-NOMA, and ADF-NOMA, Table 3.3 presents an overview of the advantages and disadvantages of each framework.

3.4 Relevant Challenges and Research Opportunities

In this section, we provide potential challenges and promising research possibilities to effectively deploy AIRS-NOMA networks.

3.4.1 Channel Model and Estimation Strategies

In a general AIRS-NOMA network, the e2e channel (i.e., the channel from terrestrial BS to the ground users through each element of AIRS) is composed of three components. More specifically, the channel responses between the terrestrial BS and AIRS, the AIRS's reflection matrix, and the channel responses between AIRS and ground users link. The combination of these three components, BS-AIRS-user, can be represented by a multiplicative channel model, where each element of AIRS's reflection matrix receives the signal from the BS, and then, via a smart controller that enables dynamic adjustment of amplitude and phase shift, reflects the impinging signal. Since IRS is coupled to the UAV, the system experiences a rapid dynamic mobility pattern. This mobile operation requires real-time channel estimation and reconfiguration, taking into account fading and shadowing effects. Furthermore, the smart controller also plays the role of dynamic exchanging information between the AIRS and terrestrial BS. Based on this, one can ask how is it possible to enable real-time reconfigurability under mobile conditions using a processing effort as low as possible due to the hardware limitation of the IRS.

Channel design and estimation for AIRS-NOMA are critical research topics due to its dynamic CSI-dependence to configure the reflecting elements, the passive nature of AIRS elements, and the multi-user nature of NOMA. To develop robust aerial channel models, one needs to take into account factors that could affect the system performance, such as IRS reflection coefficients, elements' mutual coupling, reflection loss, fluctuations and misaligned signal beams due to the UAV mobility, and NOMA decoding order, since the decoding order is not determined by channel conditions. Unlike the conventional technologies, the passive IRS architecture is not composed of a transceiver chain but is equipped with meta-materials to reflect the signal in the desired direction. Then, the IRS structure cannot employ complex signal processing tasks. In addition, the most conventional communication system operates in far-field conditions, i.e., the distance between the users and the transmitter/receiver antennas is supposed to be large. On the other hand, in an AIRS-NOMA network, one cannot guarantee that the distance between users and its serving IRS is far enough to operate only as a far-field regime or small enough to operate as a near-field regime due to the UAV mobility. Thus, the system must be dynamically adapted to decide which regime it should operate in.

Another important factor that should be strictly considered in the channel modeling is the size of the AIRS. In particular, channel coefficients are proportional to the number of reflecting elements, which induces the cascaded channel estimation problem. To circumvent this issue when the number of AIRS reflecting elements is not large, a decomposition method for cascaded channel estimation can be employed for each AIRS element to transform the cascaded channel into a series of sub-channels by each user [0]. However, when the number of AIRS reflecting

elements and the number of users increase, this method is difficult to implement due to the high signaling overhead. Unlike the fixed semi-passive IRS deployment, where it is possible to estimate the global CSI by integration of at least low-power sensors to reconfigure each AIRS's element [0], AIRS under mobility imposes extra estimation difficulty due to the need to realize fast real-time IRS configuration, which leads to high computation complexity for the time-varying channels. In consequence, additional sensing components are required to employ sophisticated channel estimation protocols, which can potentially lead to high-energy consumption. From an implementation perspective, current channel estimation methods are not appropriate to explore the benefits of the AIRS-NOMA networks. One approach to circumvent this problem consists of inserting additional sensing components at the terrestrial BS to control and optimize channel estimation methods. If these methods are employed by terrestrial control, the BS can provide high computational power to estimate the channel and the processing cost at the IRS might be minimized. However, due to the fast time-varying wireless environment and dynamic QoS requirements of the users, the AIRS control layer must send data of the environment and send measurements to the ground controller for optimization of channel estimation protocols. Then, the AIRS control layer needs additional sensing components with receiver chains to enable information exchange with BS. Therefore, efficient algorithms should be carefully developed to maintain as low complexity as possible and to avoid operations that require high-energy consumption.

3.4.2 Deployment Strategy

As previously introduced, the complexity of the channel acquisition increases as the number of users and reflecting elements of IRS increase. In addition, from a NOMA implementation perspective, there is a limited number of users that can be served in the same resource block. However, the design of efficient user clustering schemes plays an important role to exploit the benefits of AIRS-NOMA networks to support the massive number of devices [0]. But, to jointly enhance the coverage area, the proposition of deployment strategies to efficiently explore the AIRS-NOMA framework arises as one important research topic. By designing a practical deployment of AIRS-NOMA network under real-time reconfigurability, especially under mobility conditions that demand dynamic IRS configuration, it is needed to take into account the heterogeneous QoS requirements and the heterogeneous mobility profiles.

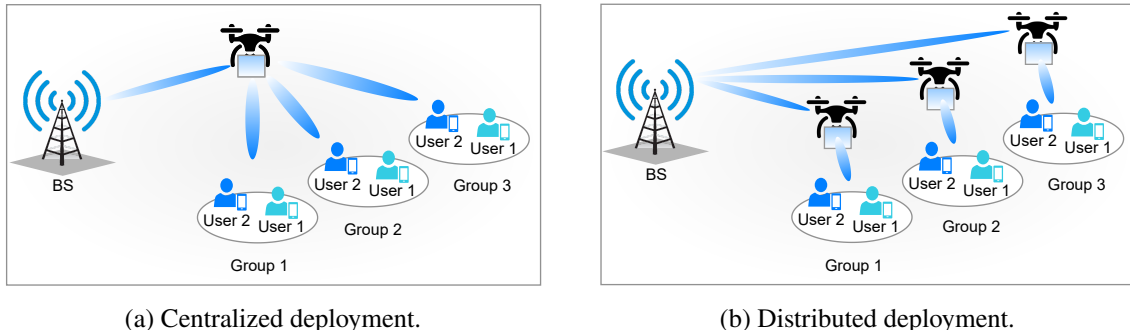


Figure 3.13: Different deployment strategies.

To circumvent these issues, cluster-based strategies are approaches that aim to serve multiple users according to specific requirements with a passive 3D beam. In particular, the users can be clustered in centralized and distributed designs. In the previous results, we employed a centralized design where the users are partitioned into multiple clusters and each group is served from passive beamforming of a single centrally deployed AIRS, as illustrated in Fig. 3.13a. This strategy is ideal for cases where groups of users are not separated by large distances, where the AIRS forms multiple independent beams to each users' group so that their channel gains could be dynamically enhanced, offering additional degrees-of-freedom in the time, frequency, and spatial domains. Despite the above advantages, a large number of reflecting elements is required to improve the 3D beamforming of each group. In consequence, the complexity and energy consumption increase, since the energy neutrality assumption cannot be satisfied and the structure must be equipped with low-power electronics to enable the IRS's reconfigurability capability. In addition, due to the proximity, the signals reflected by one AIRS to a specific cluster might be a strong impact on the reception performance of other clusters. On the other hand, the distributed design can be employed to circumvent cluster interference. In this distributed strategy, each cluster is served by distinct beamforming AIRS, as illustrated in Fig. 3.13b. As a result, the signals reflected by one IRS for a specific cluster have a low impact on the performance of the other clusters due to the relatively large distances. However, this strategy is not always feasible to deploy due to the demand for an excessive amount of energy to support the hardware. Since both described strategies offer advantages and disadvantages, it is needed to identify scenarios feasible to deploy each strategy such that they satisfy all the requirements of NOMA transmission. From the implementation perspective, a more flexible design will be a hybrid IRS deployment to achieve a trade-off between them.

Fig. 3.14 illustrates the performance in terms of sum-rate for both centralized and distributed design. These results demonstrate the good performance when AIRS is designed in near-field conditions to the users, i.e., when an AIRS is located nearby a specific user group. On the other hand, a distributed mode requires higher deployment cost. Thus, the implementation scenario must be carefully studied to ensure the efficient deployment of AIRS. In addition, a new research perspective arises to employ efficiently AIRS in far-field conditions in order to verify its viability.

3.4.3 Terahertz (THz) Communications

Research efforts have been made along the last years on the IRS-enhanced THz communications field. However, most of these efforts are related to terrestrial IRS-enhanced THz communications [0]. In contrast with communications based on microwave and millimeter waves, THz communication achieves ultra-high transmission rates from hundreds of gigabits per second with extremely narrow frequency bands [0]. This feature results in the formation of a signal beam much narrow, which can produce high attenuation and, consequently, brings out performance damage. In particular, it is hard to perform the control of these beams. To tackle this challenge, IRS can be used to design the signal beam due to the ability to smartly manipulate and design the impinging waves.

As presented in the previous section, AIRS-NOMA framework can provide enormous performance gains to the system in terms of data rate, coverage range, and energy efficiency when

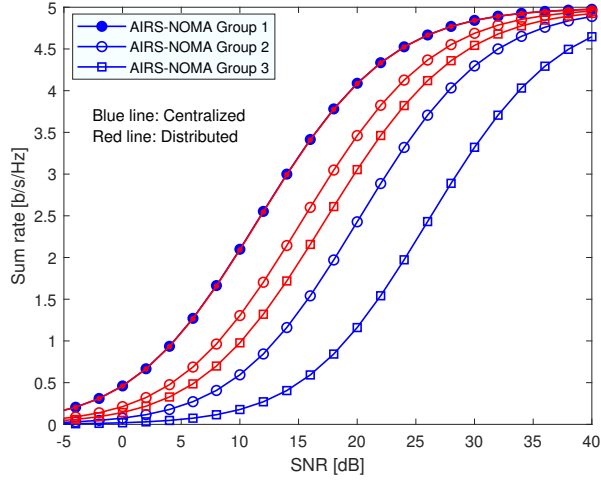


Figure 3.14: Sum-rate versus SNR for AIRS-NOMA system with centralized and distributed deployment. For centralized deployment, the approximate distance between the AIRS and the group 1, group 2, and group 3 are, respectively, 20m, 50m, 100m. For centralized deployment, the approximate distance between the AIRS and a specific group is 20 m. ($K = 20$, $\epsilon = 0.01$, $\alpha_{g1} = 0.7$, and $\alpha_{g2} = 0.3$).

compared with TIRS-NOMA scheme. By considering aerial scenarios, some works have been exploring the integration of AIRS-empowered THz communication [0]. Despite the benefits achieved by the integration of AIRS-NOMA and THz communication, there is a high attenuation THz channel that will introduce new challenges to the AIRS-NOMA communication. Specifically, channel measurements and modeling of THz waves at the sufficiently realistic mobility model must be adequate to the propagation peculiarities of AIRS-NOMA, such as path-loss models, both far-field and near-field transmission, practical phase-shift model, and beamforming control.

In addition, the decoding complexity of NOMA systems is another important challenge to be investigated when THz communication is considered. Although the THz band can support many connected devices, the decoding complexity for NOMA communication to support the devices can increase substantially. Interestingly, the IRS is one of the most promising solutions due to the AIRS to tune the channel conditions of the user by smartly adjusting the reflecting elements [0]. By considering AIRS, it is possible to improve spectrum efficiency and get good coverage capacity to allow more users to connect to the network even at a high distance from BS. In addition, due to the strong directivity of THz waves, the LoS THz waves can be easily blocked by obstacles. Thus, the AIRS framework plays an important role in THz communication due to the ability to improve the LoS path. As far as we know, there are no works that integrate AIRS-NOMA in THz communications. Based on the guidance provided, there are emerging challenges and significant problems that will be faced in future research in AIRS-NOMA empowered THz communication.

3.4.4 Reinforcement Learning in AIRS-NOMA Networks

To overcome the highly dynamic environment and, effectively, to exploit the benefits of integrating IRSs in the UAV-aided NOMA systems, machine learning techniques applied in communication

systems have been arisen as a powerful solution due to the learning features. In particular, RL methods are a branch of machine learning whose main characteristic is the learning of the ideal strategy by exploring unknown environments based on real-time data. More specifically, RL consists of an interactive algorithm that provides one representation of the particulars in an environment by taking actions and receiving rewards. A typical RL-based model for an AIRS-NOMA network is designed to take into consideration four components: agents (BS/UAV/IRS), states (interactions in real-time with the environment), actions (decision-making according to the current state), and rewards (since the action is carried out, the agent obtains a reward or penalty) [0].

The RL-based solutions have the advantage of requiring low training overhead, which makes them practical in a real-time reconfiguration of the IRS. Based on this, the design and deployment of an AIRS-NOMA network can be powerfully optimized by RL methods. In addition, flexible NOMA decoding order design can be proposed by efficient power allocation policy in an effort to maximize the sum-rate and to guarantee successful SIC while opportunistically exploring the time-varying data requirement of users. To circumvent the cascaded channel estimation problem, RL algorithms can be designed to reduce the overhead of CSI acquisition by learning both from the environment and from the feedback of the users, resulting in a fast adaption to the dynamic environment and directly optimizing both the beamformers at the BS and the reflecting elements at the IRS. From the point of view of security, RL methods can be used to learn the external and internal eavesdropping features on a network. Considering that the CSI of the eavesdropper is a challenge to acquire in practice, the proposition of RL methods can facilitate the identification of potential eavesdroppers, and effectively prevent information leakage and improve the legitimate reception quality scenarios.

Since RL methods allow agents to improve their capabilities based on the real-time experience of the environment, models can be formulated to smartly control and optimize the network to generate a trade-off between network capacity and energy consumption. In particular, the UAVs are powered by onboard batteries that usually have limited capacity and lifetime. Then, energy harvesting technologies [0], such as wireless power transfer [0], can be used to mitigate the impact of limited energy and battery lifetimes. These technologies can be empowered by RL-based algorithms to achieve efficiently a trade-off between the high energy demand of the UAV and the limited battery capacities, even under scenarios with high mobility. For example, transmit power and energy consumption of UAV can be improved by optimizing the trajectory of UAV, practical beamforming models for AIRS and BS can be designed by efficiently phase shift.

3.4.5 AIRS Standardization

In the standardization context, research efforts are carried out in the field of IRSs. Due to the potential that IRS technology provides, many universities and research institutions have gradually increased their investments in IRS research. In particular, there are two possible paths for IRS standardization in 3rd Generation Partnership Project (3GPP). First, study items will be performed on one or multiple practical scenarios and channel models in Release 18, and then the work item process will be started in Release 19. Another possible path may be to standardize IRS

as part of 6G standards, along with other new features for 6G. This is possible because it can be harmoniously combined with other expected technologies for Beyond Fifth-Generation (B5G) systems. In June 2021, a new Industry Specification Group (ISG) on IRS was approved by the European Telecommunications Standards Institute (ETSI) [0]. Specifically, three new work items were approved, which consist of channel modeling, use cases, deployment scenarios, and impact to current standards. In [0], the authors provide an industrial viewpoint and a roadmap in order to make IRSs industrially feasible. The authors discussed the relevance of the IRS technology in the latest wireless communication standards, the challenges to commercialize IRSs, and highlight the current and future standardization activities for the IRS technology.

On the other hand, in the aerial context, there has already been much activity in the workgroups of 3GPP to ensure that the fifth-generation (5G) and B5G systems will meet the connectivity needs of Unmanned Aerial Systems (UAS). Specifically, Release 17 - 5G Enhancement for UAVs (TS22.125; TS22.261) [0], is not complete and 3GPP has been making efforts to complete it with a focus on B5G systems and already thinking about possible improvements in Release 18. Based on this, substantial investment from research and businesses is expected in the next years to reach fast progress in the field of implementing, testing, and realistic prototypes in the context of AIRS.

3.5 Conclusion

In this chapter, the integration of AIRS with MIMO-NOMA technique was investigated. We provided a comprehensive discussion of the AIRS-NOMA network and performance comparison between aerial and terrestrial deployment, including fundamentals, potential achievements of efficient integration, and future challenges. Numerical simulations were presented to demonstrate that AIRS-NOMA scheme can be considered as a key enabler of future wireless communication. The obtained results supported our insightful discussions by comparing AIRS-NOMA with achieved results by TIRS-NOMA, and ADF-NOMA deployment, in which the robustness of AIRS-NOMA was confirmed. Specifically, the integration has the capability to extend the communications coverage, increase the sum-rate, enhance user fairness, and improve energy efficiency due to the capacity of enabling long-range communication, providing dynamic and adaptive coverage range to serve the users by compensating the power consumption of UAV and IRS during the communication process. In addition, challenges to inspire future research about the integration of AIRS-NOMA were highlighted. In particular, we discussed channel modeling and estimation challenges associated to real-time reconfigurability of AIRS under mobility conditions and discussed the deployment design based on cluster-based strategies for AIRS-NOMA network, such as centralized and distributed strategies. In general, when AIRSs are designed as distributed strategies with near-field conditions for each user group, the performance in terms of data rate is better, but the deployment cost is higher. On the other hand, centralized deployment presents simplified maintenance, reduced deployment cost, and a data rate higher than terrestrial deployment. These features make centralized deployment viable in suburban and rural areas, and in environmental disaster scenarios. In addition, we also discussed the integration of AIRS-NOMA with THz communication, and potential solutions based on RL methods to decrease the overhead of the CSI acquisition and improve the energy consumption

performance of the network.

Rate-Splitting Multiple Access Networks Assisted by Aerial Intelligent Reflecting Surfaces

B. K. S. Lima et al., "Rate-Splitting Multiple Access Networks Assisted by Aerial Intelligent Reflecting Surfaces," 2022 IEEE Latin-American Conference on Communications (LATINCOM), Rio de Janeiro, Brazil, 2022, pp. 1-6, doi: 10.1109/LATINCOM56090.2022.10000454.

4.1 Introduction

To efficiently support the heterogeneous services that are expected for sixth-generation (6G) wireless systems, the design of appropriate multiple access techniques is crucial for future networks. Recently, Rate-Splitting Multiple Access (RSMA) scheme has received considerable attention as a promising enabling technique in 6G networks [0].

RSMA scheme presents a more general and robust transmission framework compared to Non-Orthogonal Multiple Access (NOMA) [0]. In contrast with NOMA, where the messages are superposed into only one stream with different levels of power or spreading sequences [0], the message transmitted to the users in RSMA scheme is divided into a common message and private message by applying superposition coding at the Base Station (BS). Then, both common and private messages are simultaneously transmitted, in which the extra Degree-of-Freedom (DoF) can be achieved by exploiting smartly the common message(s). At the receivers, the decoding process is carried out by using Successive Interference Cancelation (SIC) technique [0]. Specifically, the common message is decoded by all users and the private message is decoded only by the intended user. To decode the common message, the users first decode the interference part of the signal from other users. Assuming perfect SIC, the intended user decodes its private message, treating the private message of the remaining users as interference.

In order to customize the propagation environment of future communication systems, Aerial Intelligent Reflecting Surface (AIRS)s arise as a promising technology to assist RSMA networks. An Intelligent Reflecting Surface (IRS) is a planar metasurface composed of a large number of reflecting elements [0]. Each reflecting element can be programmed independently to induce

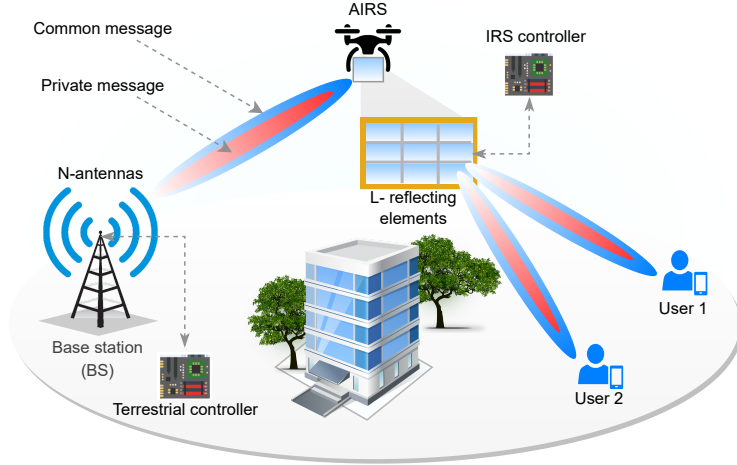


Figure 4.1: Illustration of AIRS-RSMA network with two users.

distinct phase and amplitude changes, which enables IRSs to reflect and steer impinging waves towards any desired direction. Despite the potential gains, few works exploit the combination of IRS and RSMA [0]. In particular, the authors in [0] studied RSMA scheme for IRS-enabled Unmanned Aerial Vehicle (UAV), in which the UAV acts as a BS and IRS is mounted on the facade of a building, i.e., Terrestrial Intelligent Reflecting Surface (TIRS).

By deploying IRS on aerial platforms, it is possible to achieve numerous benefits when compared to the TIRS deployment [0]. For instance, AIRS can provide flexible deployment and full-angle panoramic reflection (360°) [0]. Moreover, only one reflection is sufficient due to Line-of-Sight (LoS), while for terrestrial designs multiple reflections are required due to non line-of-sight (NLoS), which makes the TIRS design relatively challenging to improve beam propagation. To the best of our knowledge, there is no published work that investigates AIRS in RSMA networks. In order to fill out this gap that exists in the literature, this chapter investigates downlink AIRS-aided Multiple-Input Single-Output (MISO) RSMA aerial IRS in MISO-RSMA (AIRS-RSMA) networks, in which a beamforming design is proposed under the assumption of imperfect SIC. In particular, an optimization problem is formulated in order to maximize the total achievable rate by optimizing the transmit beamforming at the BS and common rates to individual users. Due to the non-convexity feature, the optimization problem is converted into an Semi-Definite Program (SDP) problem and an Alternating Optimization (AO)-based method is used to design a suboptimal algorithm for solving, iteratively, the beamforming problem. To demonstrate the robustness of the proposed method, simulation results are presented. The obtained results show that the performance achieved by the proposed approach can reach up to 13% and 43.5% gains in terms of sum-rate compared to AIRS-RSMA without optimization and conventional aerial IRS in MIMO-NOMA (AIRS-NOMA)-Multiple-Input Multiple-Output (MIMO) schemes, respectively.

4.2 System Model

Consider a MISO-RSMA downlink network where one base station (S) equipped with N antennas communicates with $K = 2$ single-antenna users¹. Due to the blockage, it is assumed that there is no direct link between the BS and the k -th user, with $k \in \mathcal{K} = \{1, 2\}$. Thus, an IRS with L reflecting elements is installed at the UAV to enable the communication between the BS and the users. In addition, it is assumed that the UAV continuously flies with a constant velocity in a spherical plane of radius r_u .

Based on RSMA principles, the message intended for k -th user is split into two messages: common and private [0]. Specifically, the messages of each user are encoded together in a common stream s_c , using a codebook shared by each user, while its private message is encoded independently into $s_{p,k}$ streams. At the transmitter, the data streams are linearly precoded and simultaneously transmitted. Then, the signal transmitted by the BS can be written as

$$\mathbf{x} = \mathbf{Ps} = \mathbf{p}_c s_c \alpha_c + \sum_{k=1}^K \mathbf{p}_k s_k \alpha_{p,k}, \quad (4.1)$$

where $\mathbf{s} = [s_c \alpha_c, s_1 \alpha_{p,1}, \dots, s_K \alpha_{p,K}]^T \in \mathbb{C}^{(K+1) \times 1}$ denotes the vector of symbol streams to be transmitted and $\mathbf{P} = [\mathbf{p}_c, \mathbf{p}_1, \mathbf{p}_2] \in \mathbb{C}^{N \times 1}$ stands for the beamforming matrix, with $N \geq (K+1)$, where $\mathbf{p}_m \in \mathbb{C}^{N \times 1}$ with $m \in \mathcal{M} = \{c, 1, 2\}$. In addition, α_c and α_k , with $k \in \{1, 2\}$, represent the power allocation coefficient to the common message and private message, respectively, in which $\alpha_c + \sum_{k=1}^K \alpha_k = 1$.

The channel gain of the BS→AIRS and AIRS→ k -th user links can be expressed, respectively, as

$$\mathbf{H}_{Sr} = \sqrt{\beta_{Sr}} \mathbf{G}_{Sr} \in \mathbb{C}^{N \times L}, \quad (4.2)$$

and

$$\mathbf{h}_{rk} = \sqrt{\beta_{rk}} \mathbf{g}_{rk} \in \mathbb{C}^{L \times 1}, \in \mathbb{C}^{L \times 1} \forall k \in \mathcal{K}, \quad (4.3)$$

where $\beta_{Sr} = \beta_0 d_{Sr}^{-\nu}$ and $\beta_{rk} = d_{rk}^{-\nu}$ denote, respectively, the large-scale average channel power gain between BS→AIRS and AIRS→ k -th user, with $r = \{1, \dots, L\}$, in which β_0 symbolizes the gain parameter. The parameter d_j , with $j \in \{Sr, rk\}$, means the distance between BS→AIRS and AIRS→ k -th user, and ν refers to the pathloss exponent. In addition, \mathbf{G}_{Sr} and \mathbf{g}_{rk} denote the small-scale fading, modeled by the Nakagami distribution, as in [0].

It is assumed that the AIRS is equipped with a controller which can smartly adjust the AIRS's phase shifts. To characterize the phase shifts, it is considered that the phase-shift matrix of the AIRS is diagonal and can be written as [0] $\boldsymbol{\Phi} = \text{diag}[\kappa_1 e^{j\theta_1}, \kappa_2 e^{j\theta_2}, \dots, \kappa_L e^{j\theta_L}] \in \mathbb{C}^{L \times L}$, where $\theta_L \in [0, 2\pi)$ denotes the phase-shift occurring at r -th element of the AIRS and $\kappa_L \in [0, 1)$ refers to the fixed amplitude reflection coefficient. In particular, the effective end-to-end (e2e) channel gain from the BS to k -th user via AIRS is given by

$$\mathbf{h}_k = \mathbf{H}_{Sr} \boldsymbol{\Phi} \mathbf{h}_{rk}^H \in \mathbb{C}^{N \times 1}. \quad (4.4)$$

¹The proposed scheme will add some insights to the technical literature which can be used as a benchmark for future studies in multiuser scenarios.

The signal received at the k -th user can be expressed as $y_k = \mathbf{h}_k \mathbf{x} + \omega_k$, where $\omega_k \sim \mathcal{CN}(0, \sigma^2)$ denotes the additive Gaussian noise (AWGN) at the k -th user.

In RSMA systems, the SIC technique is used once in each receiver to separate the common and private messages. After the common message is separated using SIC, the private message of a specific user can be decoded, considering the private message of the other users as interference. Specifically, the corresponding Signal-to-Interference-plus-Noise Ratio (SINR) to decode the common message at the k -th user is given by

$$\gamma_{c,k} = \frac{\rho |\mathbf{h}_k \mathbf{p}_c|^2 \alpha_c^2}{\rho \sum_{i=1}^K |\mathbf{h}_k \mathbf{p}_i|^2 \alpha_k + 1}, \quad (4.5)$$

where ρ means the transmit Signal-to-Noise Ratio (SNR), $\mathbf{p}_c \in \mathbb{C}^{N \times 1}$ denotes the beamforming vector of the common message serving all users and $\mathbf{p}_i \in \mathbb{C}^{N \times 1}$ represents the beamforming vector of the private message for the k -th user. The design of beamforming vectors will be discussed in the next section.

By considering imperfect SIC, the k -th user must decode its private message taking into account the other users' private messages and the common message as noise. Thus, the SINR to decode the private message at the k -th user is given by

$$\gamma_{p,k} = \frac{\rho |\mathbf{h}_k \mathbf{p}_k|^2 \alpha_k}{\rho |\mathbf{h}_k \mathbf{p}_c|^2 \alpha_c \epsilon + \rho \sum_{i \neq k}^K |\mathbf{h}_k \mathbf{p}_i|^2 \alpha_k + 1}, \quad (4.6)$$

where $\epsilon \in [0, 1]$ is the coefficient of imperfect SIC. On the one hand, instantaneous achievable rate of the k -th user in decoding the common message can be expressed as

$$r_{c,k} = \log_2(1 + \gamma_{c,k}). \quad (4.7)$$

On the other hand, the e2e instantaneous achievable rate of the k -th user in decoding its desired private message can be expressed as

$$r_{p,k} = \log_2(1 + \gamma_{p,k}). \quad (4.8)$$

Since the common message is shared amongst all users, the rate of the common message is formulated as $\min_{k \in \mathcal{K}} \{r_{c,k}\}$ to ensure that all users can decode the common message. Given the common rate $\min_{k \in \mathcal{K}} \{r_{c,k}\}$ and the rate $\bar{r}_{c,k}$ to the k -th user, the constraint $\sum_{i=1}^K \bar{r}_{c,i} \leq \min_{k \in \mathcal{K}} \{r_{c,k}\}$ should be satisfied.

Finally, based on the achievable common rate $\bar{r}_{c,k}$ and achievable private rate $r_{p,k}$, the total achievable rate of the k -th user can be expressed as

$$R_k^{\text{tot}} = \bar{r}_{c,k} + r_{p,k}. \quad (4.9)$$

Next, a beamforming design for the proposed AIRS-RSMA network is formulated.

4.3 Beamforming Design for the Proposed AIRS-RSMA Network

4.3.1 Problem Formulation

Given the considered system model, we formulate an optimization problem to maximize the minimum total achieved rate via transmit beamforming optimization at BS and achievable common rate at the users, taking into account imperfect SIC. The optimization problem can be formulated as

$$\max_{\mathbf{P}, \bar{\mathbf{r}}_c} \min_{k \in K} \{R_k^{\text{tot}}\}, \quad (4.10a)$$

subject to

$$C1 : r_{c,k} \geq \sum_{i=1}^K \bar{r}_{c,i}, \forall k \in K, \quad (4.10b)$$

$$C2 : \sum_{m \in \mathcal{M}} \|\mathbf{p}_m\|^2 \leq P_{tot}, \quad (4.10c)$$

$$C3 : \bar{r}_{c,k} \geq 0, \quad (4.10d)$$

$$C4 : \alpha_c + \sum_{k=1}^K \alpha_k = 1, \quad (4.10e)$$

where $\bar{\mathbf{r}}_c = [\bar{r}_{c,1}, \dots, \bar{r}_{c,K}]^T$ denotes the vector of achievable common rate among users, which is optimized together with the precoding matrix \mathbf{P} , and P_{tot} refers to the maximum transmit power at BS. Constraint (4.10b) ensures that all users can decode correctly the common message. Constraint (4.10d) is imposed to guarantee that the common rate achieved by k -th user is non-negative.

4.3.2 Transmit Beamforming Optimization

To solve the problem (4.10a), we first transform it into its epigraph form to facilitate the design of a method based on majorization minimization. Firstly, we introduce two optimization variables, $\mathbf{r}_p = [r_{p,1}, \dots, r_{p,K}]^T \geq 0$ and $\Omega \geq 0$. The problem (4.10a) can be rewritten as

$$\max_{\mathbf{P}, \bar{\mathbf{r}}_c, \mathbf{r}_p, \Omega} \Omega, \quad (4.11a)$$

subject to

$$C1 : R_k^{\text{tot}} \geq \Omega, \forall k \in \mathcal{K}, \quad (4.11\text{b})$$

$$C2 : A_{c,k}(\mathbf{P}) + B_{c,k}(\mathbf{P}) \geq \sum_{i=1}^K \bar{r}_{c,i}, \forall k, \quad (4.11\text{c})$$

$$C3 : C_{p,k}(\mathbf{P}) + D_{p,k}(\mathbf{P}) \geq r_{p,k}, \forall k, \quad (4.11\text{d})$$

$$C4 : \text{Tr}(\mathbf{P}_c + \sum_{k=1}^K \mathbf{P}_k) \leq P_{tot}, \quad (4.11\text{e})$$

$$C5 : \bar{r}_{c,k} \geq 0 \text{ and } r_{p,k} \geq 0, \forall k, \quad (4.11\text{f})$$

$$C6 : \mathbf{P}_m \succeq 0, \forall m, \quad (4.11\text{g})$$

$$C7 : \text{Rank}(\mathbf{P}_m) = 1, \forall m, \quad (4.11\text{h})$$

where

$$A_{c,k}(\mathbf{P}) = \log_2 \left(\rho \mathbf{h}_k \mathbf{P}_c \mathbf{h}_k^H \alpha_c + \rho \sum_{i=1}^K \mathbf{h}_k \mathbf{P}_i \mathbf{h}_k^H \alpha_k + 1 \right), \forall k, \quad (4.12)$$

$$B_{c,k}(\mathbf{P}) = -\log_2 \left(\rho \sum_{i=1}^K \mathbf{h}_k \mathbf{P}_i \mathbf{h}_k^H \alpha_k + 1 \right), \forall k, \quad (4.13)$$

$$C_{p,k}(\mathbf{P}) = \log_2 \left(\rho \mathbf{h}_k \mathbf{P}_c \mathbf{h}_k^H \alpha_c \epsilon + \rho \sum_{i \neq k}^K \mathbf{h}_k \mathbf{P}_i \mathbf{h}_k^H \alpha_k + \rho \sum_{i=1}^K \mathbf{h}_k \mathbf{P}_i \mathbf{h}_k^H \alpha_k + 1 \right), \forall k, \quad (4.14)$$

$$D_{p,k}(\mathbf{P}) = -\log_2 \left(\rho \mathbf{h}_k \mathbf{P}_c \mathbf{h}_k^H \alpha_c \epsilon + \rho \sum_{i \neq k}^K \mathbf{h}_k \mathbf{P}_i \mathbf{h}_k^H \alpha_k + 1 \right), \forall k, \quad (4.15)$$

where $\mathbf{P}_m = \mathbf{p}_m \mathbf{p}_m^H$, with $m \in \mathcal{M} = \{c, 1, \dots, K\}$, Ω is an auxiliary optimization variable, $\text{Tr}(\cdot)$ denotes the trace of a matrix, and $\text{Rank}(\cdot)$ means the rank of a matrix. Since the elements of constraints (4.11c) and (4.11d) are concave, specifically (4.12) and (4.14), while (4.13) and (4.15) are non-convex, the problem (4.11a) is non-convex. However, these constraints are expressed in the form of differences of convex functions. Thus, (4.11c) and (4.11d) can be rewritten by their corresponding lower bound functions to tackle the non-convex parts. In addition, constraints (4.11g) and (4.11h) are imposed to guarantee that \mathbf{P}_m holds after optimization, in which the rank-one constraint in (4.11h) can be tackled by applying semi-definite relaxation technique. In particular, for handling the non-convex parts of constraints (4.11c) and (4.11d), we use the following proposition.

Proposition 1 [0]: Let $a \in \mathbb{R}^{1 \times 1}$ be a positive scalar and $f(a) = -(ab/\ln 2) + \log_2 a + (1/\ln 2)$.

It follows that

$$-\log_2 b = \max_{a>0} f(a), \quad (4.16)$$

and the optimal solution to the right-hand side of (4.16) is $a = 1/b$.

Proof: Since $f(a)$ is concave, the optimal solution to the right-hand side of (4.16) is obtained by setting $\partial f(a)/\partial a = 0$. ■

By applying Proposition 1 in (4.11a), we transform the elements (4.13) and (4.15) into convex optimization problems. In the t -th iteration, we approximate $B_{c,k}(\mathbf{P})$ and $D_{p,k}(\mathbf{P})$ as affine functions by using their corresponding lower bound functions. Thus, we have the following problems

$$B_{c,k}(\mathbf{P}) \geq \max_{\varrho_{c,k} \in \mathbb{R}^{1 \times 1}, \varrho_{c,k} > 0} \xi_{c,k}(\varrho_{c,k}), \forall k \in \mathcal{K}, \quad (4.17)$$

$$D_{p,k}(\mathbf{P}) \geq \max_{\varrho_{p,k} \in \mathbb{R}^{1 \times 1}, \varrho_{p,k} > 0} \xi_{p,k}(\varrho_{p,k}), \forall k \in \mathcal{K}, \quad (4.18)$$

where

$$\begin{aligned} \xi_{c,k}(\varrho_{c,k}) = & -\frac{\varrho_{c,k}}{\ln 2} \left(\rho \sum_{i=1}^K \mathbf{h}_k \mathbf{P}_i \mathbf{h}_k^H \alpha_k + 1 \right) \\ & + \log_2(\varrho_{c,k}) + \frac{1}{\ln 2}, \forall k \in \mathcal{K}, \end{aligned} \quad (4.19)$$

and

$$\begin{aligned} \xi_{p,k}(\varrho_{p,k}) = & -\frac{\varrho_{p,k}}{\ln 2} \left(\rho \mathbf{h}_k \mathbf{P}_c \mathbf{h}_k^H \alpha_c \epsilon \right. \\ & \left. + \rho \sum_{i \neq k}^K \mathbf{h}_k \mathbf{P}_i \mathbf{h}_k^H \alpha_k + 1 \right) \\ & + \log_2(\varrho_{p,k}) + \frac{1}{\ln 2}, \forall k \in \mathcal{K}. \end{aligned} \quad (4.20)$$

According to Proposition 1, when the optimal $\mathbf{P}_m^{(t)}$ in the $(t-1)$ -th iteration, which is denoted by $\mathbf{P}_m^{(t-1)}$, is obtained, $\varrho_{c,k}$ and $\varrho_{p,k}$ can be updated in the t -th iteration by solving

$$\begin{aligned} \varrho_{c,k}^{(t)} = & \max_{\varrho_{c,k} > 0} -\frac{\varrho_{c,k}}{\ln 2} \left(\rho \sum_{i=1}^K \mathbf{h}_k \mathbf{P}_i^{(t-1)} \mathbf{h}_k^H \alpha_k + 1 \right) \\ & + \log_2(\varrho_{c,k}) + \frac{1}{\ln 2}, \forall k \in \mathcal{K}, \end{aligned} \quad (4.21)$$

and

$$\begin{aligned} \varrho_{p,k}^{(t)} = & \max_{\varrho_{p,k} > 0} -\frac{\varrho_{p,k}}{\ln 2} \left(\rho \mathbf{h}_k \mathbf{P}_c^{(t-1)} \mathbf{h}_k^H \alpha_c \epsilon \right. \\ & \left. + \rho \sum_{i \neq k}^K \mathbf{h}_k \mathbf{P}_i^{(t-1)} \mathbf{h}_k^H \alpha_k + 1 \right) \\ & + \log_2(\varrho_{p,k}) + \frac{1}{\ln 2}, \forall k \in \mathcal{K}. \end{aligned} \quad (4.22)$$

Since perfect Channel Status Information (CSI) at the BS is assumed, (4.21) and (4.22) can be rewritten, respectively, as [0]

$$\varrho_{c,k}^{(t)} = \left(\rho \sum_{i=1}^K \mathbf{h}_k \mathbf{P}_i^{(t-1)} \mathbf{h}_k^H \alpha_k + 1 \right)^{-1}, \quad (4.23)$$

and

$$\varrho_{p,k}^{(t)} = \left(\rho \mathbf{h}_k \mathbf{P}_c^{(t-1)} \mathbf{h}_k^H \alpha_c \epsilon + \rho \sum_{i \neq k}^K \mathbf{h}_k \mathbf{P}_i^{(t-1)} \mathbf{h}_k^H \alpha_k + 1 \right)^{-1}. \quad (4.24)$$

Based on the solution $\mathbf{P}^{(t-1)}$ obtained in the $(t-1)$ -th iteration, the global underestimation of $B_{c,k}(\mathbf{P})$ in (4.13) can be iteratively approximated at the t -th iteration. Then, $B_{c,k}(\mathbf{P})$ can be re-expressed based on its lower bound function, given by $B_{c,k}^L(\mathbf{P}^{(t-1)})$ in (4.25)..

$$B_{c,k}^L(\mathbf{P}^{(t-1)}) = \max_{\varrho_{c,k}^{(t)} > 0} - \frac{\varrho_{c,k}^{(t)} \left(\rho \sum_{i=1}^K \mathbf{h}_k \mathbf{P}_i^{(t)} \mathbf{h}_k^H \alpha_k + 1 \right)}{\ln 2} + \log_2(\varrho_{c,k}^{(t)}) + \frac{1}{\ln 2}, \forall k \in \mathcal{K}, \quad (4.25)$$

In a parallel avenue, in t -th iteration $D_{c,k}(\mathbf{P})$ in (4.15) is replaced by its lower bound. Its corresponding lower bound solution is given by $D_{p,k}^L(\mathbf{P}^{(t-1)})$, shown in (4.26).

$$D_{p,k}^L(\mathbf{P}^{(t-1)}) = \max_{\varrho_{p,k}^{(t)} > 0} - \frac{\varrho_{p,k}^{(t)} \left(\rho \mathbf{h}_k \mathbf{P}_c^{(t)} \mathbf{h}_k^H \alpha_c \epsilon + \rho \sum_{i \neq k}^K \mathbf{h}_k \mathbf{P}_i^{(t)} \mathbf{h}_k^H \alpha_k + 1 \right)}{\ln 2} + \log_2(\varrho_{p,k}^{(t)}) + \frac{1}{\ln 2}, \forall k \in \mathcal{K}, \quad (4.26)$$

As a result, the problem (4.11a) can be expressed based on its lower bound functions and, therefore, reformulated as follows

$$\max_{\mathbf{P}^{(t)}, \bar{\mathbf{r}}_c, \mathbf{r}_p, \Omega} \Omega, \quad (4.27a)$$

subject to

$$C1 : R_k^{\text{tot}} \geq \Omega, \forall k \in \mathcal{K}, \quad (4.27b)$$

$$C2 : A_{c,k}(\mathbf{P}_c^{(t)}) + B_{c,k}^L(\mathbf{P}_c^{(t-1)}) \geq \sum_{i=1}^K \bar{r}_{c,i}, \forall k, \quad (4.27c)$$

$$C3 : C_{p,k}(\mathbf{P}_k^{(t)}) + D_{p,k}^L(\mathbf{P}_k^{(t-1)}) \geq r_{p,k}, \forall k, \quad (4.27d)$$

$$C4 : \text{Tr}(\mathbf{P}_c + \sum_{k=1}^K \mathbf{P}_k) \leq P_{tot}, \quad (4.27e)$$

$$C5 : \bar{r}_{c,k} \geq 0 \text{ and } r_{p,k} \geq 0, \forall k, \quad (4.27f)$$

$$C6 : \mathbf{P}_m \succeq 0, \forall m, \quad (4.27g)$$

$$C7 : \text{Rank}(\mathbf{P}_m) = 1, \forall m. \quad (4.27h)$$

One can notice that the problem (4.27a) consists in an SDP problem. Thus, one can use the AO approach to design a suboptimal iterative algorithm in order to optimize $\varrho_{c,k}^{(t)}$, $\varrho_{p,k}^{(t)}$, and \mathbf{P}_m , $\forall k \in \mathcal{K}$, and $\forall m \in \mathcal{M}$, at each iteration. If the optimal matrix solutions to the problem (4.27a) are rank one, then the optimal precoders are defined as the optimal solution to the problem.

Algorithm 6 AO algorithm for Beamforming Design in AIRS-RSMA networks

Initialize: $\mathbf{P}_m^{(0)} \forall m \in \mathcal{M}$, set the convergence index $\tau = 10^{-4}$, and the number of iteration $t = 1$;

- 1: **Repeat:**
- 2: In the t -th iteration, approximate $B_{c,k}(\mathbf{P})$ and $D_{p,k}(\mathbf{P})$ as affine functions by using their corresponding lower bound functions obtained by solving (4.17) and (4.18).
- 3: Solve (4.23) and (4.24) to obtain $\varrho_{c,k}^{(t)}$ and $\varrho_{p,k}^{(t)}$, respectively;
- 4: With the given $\varrho_{c,k}^{(t)}$ and $\varrho_{p,k}^{(t)}$, solve the problem (4.27a) to obtain $\mathbf{P}_m^{(t)}$;
- 5: Given $\mathbf{P}_m^{(t)}$, solve (4.7) and (4.8) to obtain $r_{c,k}$, and $r_{p,k}$;
- 6: Update iteration $t = t + 1$;
- 7: **Until:** $|\Omega^{(t)} - \Omega^{(t-1)}| < \tau$ or $t = T_{\max}$;

Output: $\mathbf{P}_m^* = \mathbf{p}_m^{(t)} \mathbf{p}_m^{(t),H}, \forall m \in \mathcal{M}$, $\bar{r}_{c,k}$, and $r_{p,k}$.

To verify that the relaxed problem satisfies the rank-one condition, the following proposition is presented.

Proposition 2: The solution for \mathbf{P}_m of the problem (4.27a) satisfies the rank-one conditions.

Proof: Please refer to Appendix A.

Thus, by performing an eigenvalue decomposition on the solution \mathbf{P}_m^* , the beamforming vector \mathbf{p}_m^* that maximizes the achievable rate is obtained by selecting the principal eigenvector. The proposed algorithm to realize the above alternating optimization is summarized in Algorithm 6. Since \mathbf{P} and $\bar{\mathbf{r}}_c$ are optimized, the objective value is non-decreasing and the convergence of problem (4.27a) is guaranteed for a sufficient number of iterations T_{\max} . On the other hand, the stop criteria $|\Omega^{(t)} - \Omega^{(t-1)}| < \tau$ controls the convergence of Algorithm 6.

4.4 Simulation Results

In this section, simulations results are provided to evaluate the performance of the proposed transmit beamforming design in AIRS-RSMA networks. It is considered a scenario with $N = 4$ antennas at the BS and $K = 2$ single-antenna users, in which the center of cell where the users are positioned is located at $d_{SK} = 100$ m from the BS. Once the UAV continuously flies in a radius $r_u = 5$ m, following the height range $20 - r_u \leq z \leq 20 + r_u$, the distance between the BS and AIRS, and the AIRS and users are, approximately, $d_{Sr} = 80$ m and $d_{rk} = 25$ m. In particular, it is assumed $v = 2.2$, $\alpha_c = 0.9$, $\alpha_k = 0.05 \forall k \in \mathcal{K} = \{1, 2\}$, $\mu = 2.5$, $\tau = 10^{-4}$, $T_{\max} = 10^3$, and $\beta_0 = 1000$. The parameter β_0 is adjusted based on the desired performance of the receivers [0]. For AIRS-NOMA-MISO scenario, it is considered $\alpha_1 = 0.8$ and $\alpha_2 = 0.2$ [0]. In addition, it is assumed that the power consumption of IRS is 3 mW per element.

Fig. 4.2 plots the sum-rate of the proposed AIRS-RSMA network assuming both optimized and non-optimized approaches, and different levels of imperfect SIC. For non-optimized approaches, the conventional zero-forcing (ZF) precoder is considered. For comparison purposes, the AIRS-NOMA-MISO scheme is also plotted. One can see that the proposed method can enhance significantly the performance of the system, where the sum-rate is maximized due to the extra DoF achieved

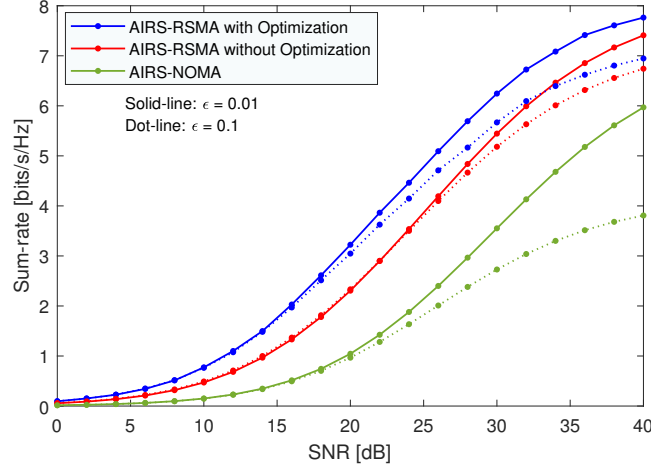


Figure 4.2: Sum-rate versus transmit SNR for different levels of imperfect SIC and $L = 50$.

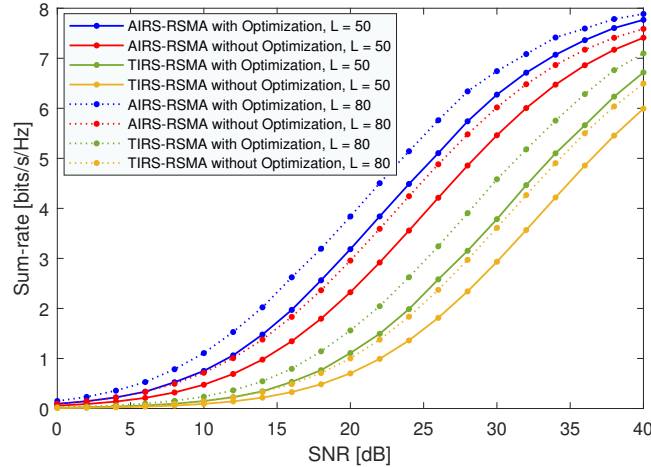


Figure 4.3: Sum-rate versus transmit SNR for different deployment, number of reflecting elements and $\epsilon = 0.01$.

by smartly utilizing the common messages. For example, when the SNR is 30 dB and $\epsilon = 0.01$, the non-optimized AIRS-RSMA achieves a performance of 5.4 bits/s/Hz, while AIRS-RSMA with optimization can reach 6.2 bits/s/Hz, which represents a performance gain of approximately 13%. Compared to the AIRS-NOMA-MISO scheme, the proposed method can achieve gains of up to 43.5% in terms of sum-rate. It is also observed that AIRS-NOMA-MISO scheme is more susceptible to the errors caused by imperfect SIC. This result is because of the message splitting process of the AIRS-RSMA scheme, where decoding errors can be reduced and controlled by adjusting the split of common and private message.

Fig. 4.3 shows the sum-rate versus transmit SNR for different deployment and number of reflecting elements. One can see that the proposed method for AIRS-RSMA scheme has the ability to achieve enhanced sum-rate compared to optimized and non-optimized TIRS-RSMA deployment. By exploring aerial setup, it can be achieved higher performance gains due to the capacity to enable long-range communication, providing dynamic and adaptive coverage range to serve the users. One

can also observe that the greater the number of reflecting elements, the higher the sum-rate that the all methods are able to achieve, which reinforces the idea that IRS can be considered a key enabler of future wireless communications.

4.5 Conclusions

In this chapter, MISO-RSMA networks assisted by AIRS under imperfect SIC was investigated. We presented the system model and formulated an optimization problem to maximize the total achievable rate by optimizing the transmit beamforming at the BS and common achievable rate of the users. To handle the non-convexity of the original problem, we converted the optimization problem into an SDP problem. To solve the reformulated problem, an iterative suboptimal algorithm based on AO method was proposed, where the solution was obtained interactively. Numerical simulations were presented and demonstrated the robustness of the proposed beamforming design for AIRS-RSMA networks, where the sum-rate is significantly improved in comparison with the non-optimized AIRS-RSMA, TIRS-RSMA, and AIRS-NOMA-MISO schemes. It is noteworthy that the presented insights can serve as a benchmark for future works, in which the multiuser scenario can be investigated as well as the design of an efficient UAV trajectory and phase shift matrix to further improve the performance of AIRS-RSMA networks.

LSTM-based Trajectory and Phase-Shift Prediction for RSMA Networks Assisted by AIRS

B. K. S. Lima, J. P. Carvalho, R. Dinis, D. B. da Costa, M. Beko, and R. Oliveira, "LSTM-based Trajectory and Phase-Shift Prediction for RSMA Networks Assisted by AIRS" in IEEE Transactions on Communications, 2024, doi: 10.1109/TCOMM.2024.3407192.

5.1 Introduction

Rate-Splitting Multiple Access (RSMA) scheme has received considerable attention as a promising enabling technique in 6G networks due to a more general and robust transmission framework [0]. In contrast with Non-Orthogonal Multiple Access (NOMA), where the messages are superposed into only one stream with different levels of power or spreading sequences [0], the message transmitted to the users in RSMA scheme is divided into a common message and private message by applying superposition coding at the Base Station (BS). Both common and private messages are simultaneously transmitted, in which the extra Degree-of-Freedom (DoF) can be achieved by exploiting smartly the common message(s). At the receivers, the decoding process is carried out by using Successive Interference Cancelation (SIC) techniques [0]. Specifically, the common message is decoded by all users and the private message is decoded only by the intended user. To decode the common message, the users first decode the interference part of the signal from other users. Assuming perfect SIC, the intended user decodes its private message, treating the private message of the remaining users as interference.

By deploying Intelligent Reflecting Surface (IRS) on aerial platforms, it is possible to achieve numerous benefits when compared to the Terrestrial Intelligent Reflecting Surface (TIRS) deployment [0]. In particular, [0] provides a comprehensive discussion about the interplay of aerial IRS in Multiple-Input Multiple-Output (MIMO) NOMA networks, as well as its architecture, functionality principles, and performance gains. For instance, Aerial Intelligent Reflecting Surface (AIRS) can provide flexible deployment and full-angle panoramic reflection [0]. To face the highly dynamic environment and exploit the potential of IRSs in multiple access networks, solutions based on

Machine Learning (ML) have been investigated over the years. In particular, the Long Short-Term Memory (LSTM) technique is a variant of Recurrent Neural Network (RNN) and has been explored due to its potential to predict sequential patterns by recursively forwarding the previous information to the memory [0]. This fact, makes LSTM specialized in extracting resources from the dynamic environment.

5.1.1 Related works

Research efforts have been carried out in the field of LSTM-enhanced wireless networks. The work [0] explored an LSTM-based algorithm in a NOMA network to detect the channel characteristics automatically. The proposed algorithm was able to train different channel conditions via offline learning and test the corresponding output data to realize automatic encoding, decoding, and channel detection. In [0], the authors investigated the problem of energy consumption in an ultra-dense network. To reduce the energy consumption of the network, the authors proposed a method by exploiting the LSTM to extract the sequential correlated features from the channel information and the feed forward network to adjust the on/off mode decision at the BS. An LSTM-based Deep Learning (DL) detector for uplink and downlink for RSMA networks was proposed in [0]. The framework eliminates the need for the use of SIC.

Related to the Reconfigurable Intelligent Surface (RIS)/IRS field, the work [0] investigated an IRS-Multiple-Input Single-Output (MISO) NOMA. The authors adopted an LSTM-based algorithm for predicting the mobility of users and a K-means-based Gaussian mixture model algorithm for user clustering. Then, a Deep Q-Learning (DQN)-based algorithm is invoked for jointly determining the phase shift matrix and power allocation policy. In [0], the authors investigated a scenario where multiple mobile robots are served by an access point (AP) through NOMA networks. The trajectories and NOMA decoding orders of robots, phase-shift of the RIS, and the power allocation of the AP were optimized via LSTM and Dueling Double Deep Q-network (D3QN) algorithm. In [0], the authors explored the problem of channel estimation for RIS-NOMA networks. A DL-based channel estimation method using a convolutional LSTM model was proposed. The algorithm exploits the characteristics of spatial features and temporal features of a time-series dataset to predict channel features.

In [0], the authors investigated multi-access edge computing-enabled and RIS-assisted Terahertz (THz) virtual reality network in an indoor scenario. LSTM and convolutional neural networks were combined to predict the locations, Line-of-Sight (LoS), and non line-of-sight (NLoS) status of the virtual users. A Deep Reinforcement Learning (DRL)-based algorithm was developed to select the optimal phase shifts of the RIS. In [0], a problem related to the energy conservation of a RIS-enabled wireless communication system for power transmission was investigated. An LSTM-based algorithm was proposed to perform decision-making by using data about channel state and RIS's energy harvesting. The LSTM uses the current configuration of the IRS, the BS's transmission power, and the receiver's location as input in the training phase. In [0], the authors terrestrial RIS-aided vehicle-to-everything systems. To provide low latency and high reliability, the authors proposed an LSTM-based algorithm to control the phase shift. The algorithm exploits and

learns temporal variation of channels from past pilot sequences.

By exploring Unmanned Aerial Vehicle (UAV)-enabled wireless networks, [0] proposed a method based on Kalman filtering and LSTM to improve the beam tracking accuracy and spectrum efficiency, while reducing the overheads of an UAV-assisted mmWave dual-band high-speed railway wireless network. The authors in [0] investigated a multi-objective optimization problem for a UAV-enabled wireless-powered Internet-of-Things (IoT) system. To minimize the total energy consumption of the UAV and maximize the system throughput and the total harvested energy, a method by combining Deep Deterministic Policy Gradient (DDPG) and LSTM was proposed. In [0], the authors proposed an LSTM-based method to predict cellular traffic. Based on the output of LSTM, the optimal positions of UAVs are derived and compared in different multiple access techniques. The UAV's position was optimized in [0]. The authors performed a data preprocessing of the spatio-temporal parameters such as longitude, latitude, altitude, and time. Then, an LSTM-based model is applied to predict the UAV's position. The works [0] also explored problems related to the UAV trajectory. In [0], the overall data loss of the ground devices was minimized by applying an LSTM-based layer to optimize trajectory and velocity by predicting the time-varying energy harvesting, data arrivals, and channel conditions. In [0], a recurrent LSTM was used to achieve an effective trajectory prediction and minimize the trajectory prediction error.

5.1.2 Motivation and Contributions

Although the aforementioned research contributions have provided solutions for AIRS or TIRS with different multiple access techniques, there is some published work that specifically investigates the integration of AIRS in RSMA networks. In particular, in [0], expressions for the approximate cumulative distribution function of common and private stream Signal-to-Interference-plus-Noise Ratio (SINR), and the average outage probability were derived. In addition, by using an iterative algorithm, the power allocation coefficients in each time slot of UAV flight duration are obtained. In a parallel avenue, the work [0] investigated a RIS-UAV-aided RSMA network. RSMA parameters, 3D-coordinates of the aerial RIS, and phase shift matrix at the RIS were jointly optimized by using a heuristic approach for optimum power allocation. In [0], a two-user scenario was explored and just beamforming was optimized. Although AIRS-RSMA systems have been investigated in recent work, the effects of the dynamic environment are still not clarified and ML-based solutions are not explored, such as the powerful LSTM technique. In order to fill out this gap in the literature, this chapter investigates downlink AIRS-aided MISO LSTM networks with multiuser. In contrast with [0], where a two-user scenario was explored and only beamforming was optimized, this work explores a multiuser scenario, for both static and dynamic user movement, in which beamforming at BS, the trajectory of the UAV, and the phase-shift of the AIRS were optimized by combining conventional optimization method and machine learning approaches. Further details and the main contributions of this work are summarized as follows:

- A beamforming design is proposed under the assumption of imperfect SIC for multiuser scenarios. In particular, an optimization problem is formulated in order to maximize the total achievable rate by optimizing the transmit beamforming at the BS and common rates

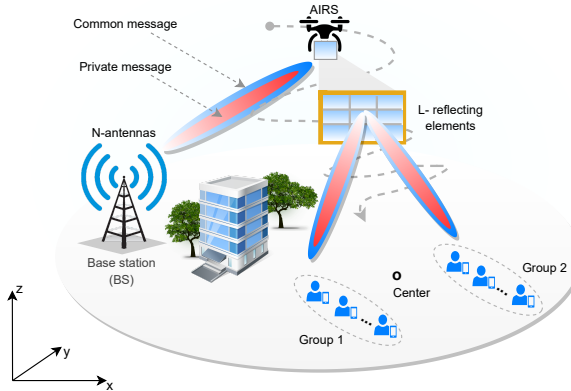


Figure 5.1: Illustration of AIRS-RSMA network with two groups of users.

to the users. The optimization problem is converted into a Semi-Definite Program (SDP) problem and an Alternating Optimization (AO)-based method is used to design a suboptimal algorithm.

- A new framework for a downlink AIRS-RSMA multiuser network is proposed to optimize the trajectory of the UAV and the phase shift of AIRS. The users are grouped by using K-means approaches and, taking into account the centroid of each user group, LSTM-based algorithms are developed to accurately design the trajectory of the UAV and the phase-shift of the AIRS. To improve the achievable rate of the system, two learning policies are proposed, in which the scenarios with static and dynamic users are explored. Then, two LSTM-based networks are employed to predict the next positions of the UAV and the efficient phase-shift of AIRS.
- To verify the adaptability of the proposed method, the UAV is configured to take a new trajectory to maximize the total achievable of the system. The UAV takes a new position, calculates the instantaneous sum-rate at time t , and compares it with the sum-rate obtained at $t - 1$. Supposing that the sum-rate at t is lower than $t - 1$, the UAV returns the previous position and recalculates a new position to maximize the total achievable rate at $t + 1$.
- Training and test results are presented to demonstrate the potential of the proposed scheme, as well as numerical simulation results. The results show that the proposed models efficiently predict the UAV's trajectory and phase-shift vectors to maximize the sum-rate of the systems for static and dynamic scenarios.

5.2 System Model

Consider a MISO-RSMA downlink network where one BS equipped with N antennas communicates with G clusters composed of U single-antenna ground users, as illustrated in 5.1. Users are clustered based on their channel gain and distance from each other [0]. To this end, the principles of K-means are exploited. For simplicity, we assume that each group consists of K users, i.e., $U = GK$. Due to

the blockage, it is assumed that there is no direct link between the BS and the k -th user of the g -th cluster, in which $k \in \mathcal{K} = \{1, \dots, K\}$ and $g \in \mathcal{G} = \{1, \dots, G\}$. Thus, an IRS with L reflecting elements, denoted by $\mathcal{L} = \{1, \dots, L\}$, is deployed at the UAV to enable communication between the BS and the users. In addition, it is assumed that the UAV continuously flies with a constant velocity in a 3D plane. Note that the beamforming at BS, the phase-shift matrix of AIRS, and the UAV trajectory will be explored in depth in the following sections. The proposed method is versatile and with great potential for adaptability, trained to enable and enhance communication in two scenarios. In the first scenario, it is assumed that the users are arranged in a static way, while in the second scenario, the users are in constant mobility in a delimited area.

Based on RSMA principles, the message intended for k -th user within g -th group is split into a common part, s_{gk}^c , and a private part, s_{gk}^p , [0]. Specifically, the messages of each user within each group are encoded together in a common stream $s_g^c = (s_{g1}^c, \dots, s_{gK}^c)$, using a codebook shared by the k -th user of the g -th group, while the private parts are encoded independently into private streams s_{gk}^p . At the transmitter, the data streams are linearly precoded and superimposed in the power domain, then simultaneously transmitted. As a result, the signal transmitted by the BS can be expressed as

$$\mathbf{x} = \sum_{g=1}^G \left(\mathbf{p}_g^c \sqrt{\alpha_g^c} s_g^c + \sum_{k=1}^K \mathbf{p}_{gk}^p \sqrt{\alpha_{gk}^p} s_{gk}^p \right) \in \mathbb{C}^{N \times 1}, \quad (5.1)$$

where the vector of symbol streams to be transmitted to the g -th group can be denoted by $\mathbf{s}_g = [s_g^c \alpha_g^c, s_{g1}^p \alpha_{g1}^p, \dots, s_{gK}^p \alpha_{gK}^p]^T \in \mathbb{C}^{(K+1) \times 1}$, where α_g^c and α_{gk}^p are, respectively, the power allocation coefficients for the common and private messages in which $\alpha_g^c + \sum_{k=1}^K \alpha_{gk}^p = 1$, $\mathbf{p}_g^c \in \mathbb{C}^{N \times 1}$ denotes the beamforming vector of the common message serving all users within g -th group and $\mathbf{p}_{gk}^p \in \mathbb{C}^{N \times 1}$ represents the beamforming vector of the private message for the k -th user of the g -th group. For notation simplicity, the precoding vectors intended for the g -th group are reexpressed by $\mathbf{P}_g = [\mathbf{p}_g^c, \mathbf{p}_{g1}^p, \dots, \mathbf{p}_{gK}^p] \in \mathbb{C}^{N \times (K+1)}$, where \mathbf{P}_g stands for the beamforming matrix of the g -th user group.

The channel gain links between the BS and the AIRS, and the AIRS and the k -th user of the g -th group can be written, respectively, as

$$\tilde{\mathbf{H}} = \sqrt{\beta_l} \tilde{\mathbf{H}} \in \mathbb{C}^{N \times L}, \quad (5.2)$$

and

$$\tilde{\mathbf{h}}_{gk} = \sqrt{\beta_{gk}} \tilde{\mathbf{h}}_{gk} \in \mathbb{C}^{L \times 1}, \quad \forall k \in \mathcal{K}, \forall g \in \mathcal{G}, \quad (5.3)$$

where $\tilde{\mathbf{H}}$ and $\tilde{\mathbf{h}}_{gk}$ denote the small-scale fading, modeled by the Nakagami distribution, as in [0]. The parameters $\beta_l = \beta_0 d_l^{-\nu}$ and $\beta_{gk} = d_{gk}^{-\nu}$ denote, respectively, the large-scale average channel power gain between the BS and the AIRS, and the AIRS and the k -th user of the g -th group, in which β_0 symbolizes the gain parameter. The parameters d_l and d_{gk} mean the distance between the BS and the AIRS, and the AIRS and the k -th user of the g -th group. In addition, ν refers to the pathloss exponent. Based on three-dimensional Cartesian coordinates, the location of the UAV can be represented by (x_l^t, y_l^t, z_l^t) and the location of the k -th user within the g -th group at the t time

step by $(x_{gk}^t, y_{gk}^t, 0)$, the distances d_l and d_{gk} can be given, respectively, by

$$d_l^t = \sqrt{(x_0 - x_l^t)^2 + (y_0 - y_l^t)^2 + (z_l^t)^2}, \quad (5.4)$$

and

$$d_{gk}^t = \sqrt{(x_l^t - x_{gk}^t)^2 + (y_l^t - y_{gk}^t)^2 + (z_l^t)^2}. \quad (5.5)$$

For each time step t , the UAV chooses a new position to cross according to the centroid of each group. Since the users are in mobility, their distances are also recalculated in each time step. The data related to the distance will be deeply explored in the following sections, specifically in the trajectory training subsection.

It is assumed that the AIRS is equipped with a controller that can smartly adjust the AIRS's phase shifts. To characterize the phase shifts, in training step, it is considered that the phase-shift matrix of the AIRS is diagonal and can be written as [0] $\Phi = \text{diag}[\kappa_1 e^{j\theta_1}, \kappa_2 e^{j\theta_2}, \dots, \kappa_L e^{j\theta_L}] \in \mathbb{C}^{L \times L}$, denotes the phase-shift occurring at r -th element of the AIRS, in which $|\kappa_l e^{j\theta_l}| = 1$ for $\theta_l \in [0, 2\pi)$ and $l \in \mathcal{L}$, and κ_l refers to the fixed amplitude reflection coefficient. We assume that $\kappa_l = 1$, as commonly adopted in the literature, i.e., [0]. For practical implementation purposes, we consider that discrete phase shifts are adopted at each element of the AIRS. Then, each element of the AIRS can take a finite number of values by uniformly quantizing the interval $[0, 2\pi)$, which can be expressed as [0]

$$\theta_l \in \left\{ \frac{2\pi n}{2^{\tilde{b}}}, n = 0, 1, 2, \dots, 2^{\tilde{b}} - 1 \right\}, \forall l \in \mathcal{L}. \quad (5.6)$$

where \tilde{b} denotes the bit resolution. The interval in (5.6) is used in the training process of our proposed DL models.

In particular, the effective end-to-end (e2e) channel gain from the BS to k -th user of the g -th group via AIRS is given by

$$\mathbf{h}_{gk} = \ddot{\mathbf{h}}_{gk}^H \Phi \ddot{\mathbf{H}} \in \mathbb{C}^{N \times 1}. \quad (5.7)$$

The signal received at the k -th user of the g -th group can be expressed as $y_{gk} = \mathbf{h}_{gk} \mathbf{x} + \omega_{gk}$, where $\omega_{gk} \sim \mathcal{CN}(0, \sigma^2)$ denotes the additive Gaussian noise (AWGN) at the k -th user within g -th group.

In RSMA systems, the SIC technique is used once in each receiver to separate the common and private messages. After the common message is separated using SIC, the private message of a specific user can be decoded, considering the private message of the other users as interference. Specifically, the corresponding SINR to decode the common message at the k -th user of the g -th group is given by

$$\gamma_{gk}^c = \frac{\rho |\mathbf{h}_{gk} \mathbf{p}_g^c|^2 \alpha_g^c}{\rho \sum_{i=1}^K |\mathbf{h}_{gk} \mathbf{p}_{gi}^p|^2 \alpha_{gi}^p + 1}, \quad (5.8)$$

where ρ means the transmit Signal-to-Noise Ratio (SNR). By considering imperfect SIC, the k -th user of the g -th group must decode its private message taking into account the other users' private messages and the common message as noise. Thus, the SINR to decode the private message at the

k -th user of the g -th group is given by

$$\gamma_{gk}^p = \frac{\rho |\mathbf{h}_{gk} \mathbf{p}_{gk}^p|^2 \alpha_{gk}^p}{\rho |\mathbf{h}_{gk} \mathbf{p}_g^c|^2 \alpha_g^c \epsilon + \rho \sum_{i \neq k}^K |\mathbf{h}_{gk} \mathbf{p}_{gi}^p|^2 \alpha_{gi}^p + 1}, \quad (5.9)$$

where $\epsilon \in [0, 1]$ is the coefficient of imperfect SIC. On the one hand, the instantaneous achievable rate of the k -th user of the g -th group in decoding the common message can be expressed as

$$r_{gk}^c = \log_2(1 + \gamma_{gk}^c). \quad (5.10)$$

On the other hand, the e2e instantaneous achievable rate of the k -th user in decoding its desired private message can be expressed as

$$r_{gk}^p = \log_2(1 + \gamma_{gk}^p). \quad (5.11)$$

Since the common message is shared amongst all users, the rate of the common message is formulated as $\bar{r}_{gi}^c = \min_{k \in \mathcal{K}} \{r_{gk}^c\}$ to ensure that all users can decode the common message. Given the common rate \bar{r}_{gk}^c , the constraint $\sum_{i=1}^K \alpha_g^c \leq \bar{r}_{gk}^c$ should be satisfied.

Finally, based on the achievable common rate \bar{r}_{gk}^c and achievable private rate r_{gk}^p , the total achievable rate of the k -th user can be expressed as

$$R_{gk}^{\text{tot}} = \bar{r}_{gk}^c + r_{gk}^p. \quad (5.12)$$

Next, a beamforming design for the proposed AIRS-RSMA network is formulated.

5.3 Beamforming Design

Given the considered system model, we formulate an optimization problem to maximize the minimum total achieved rate via transmit beamforming optimization at BS and achievable common rate at the users, taking into account imperfect SIC. The optimization problem can be formulated as

$$\max_{\mathbf{P}_g, \bar{\mathbf{r}}_g^c} \min_{k \in K} \{R_{gk}^{\text{tot}}\}, \quad (5.13a)$$

subject to

$$C1 : r_{gk}^c \geq \sum_{i=1}^K \bar{r}_{gi}^c, \forall k \in \mathcal{K}, \forall g \in \mathcal{G}, \quad (5.13b)$$

$$C2 : \|\mathbf{p}_g^c\|^2 + \sum_{i=1}^K \|\mathbf{p}_{gi}^p\|^2 \leq P_{tot}, \quad (5.13c)$$

$$C3 : \bar{\mathbf{r}}_g^c \geq 0, \quad (5.13d)$$

$$C4 : \alpha_{gk}^c + \sum_{i=1}^K \alpha_{gi}^p = 1, \quad (5.13e)$$

where $\bar{\mathbf{r}}_g^c = [\bar{r}_{g1}^c, \dots, \bar{r}_{gK}^c]^T$ denotes the vector of achievable common rate among users within g -th group, which is optimized together with the precoding matrix \mathbf{P}_g , and P_{tot} refers to the maximum transmit power at BS. Constraint (5.13b) ensures that all users can decode correctly the common message. Constraint (5.13d) is imposed to guarantee that the common rate achieved by k -th user of the g -th group is non-negative.

To solve the problem (5.13a), we first transform it into its epigraph form to facilitate the design of a method based on majorization minimization. Firstly, we introduce two optimization variables, $\mathbf{r}_g^p = [r_{g1}^p, \dots, r_{gK}^p]^T \geq 0$ and $\Omega_g \geq 0$. The problem (5.13a) can be rewritten as

$$\max_{\mathbf{P}_g, \bar{\mathbf{r}}_g^c, \mathbf{r}_g^p, \Omega_g} \Omega_g, \quad (5.14a)$$

subject to

$$C1 : R_{gk}^{\text{tot}} \geq \Omega_g, \quad (5.14b)$$

$$C2 : A_{gk}^c(\mathbf{P}_g) + B_{gk}^c(\mathbf{P}_g) \geq \sum_{i=1}^K \bar{r}_{gi}^c, \quad (5.14c)$$

$$C3 : C_{gk}^p(\mathbf{P}_g) + D_{gk}^p(\mathbf{P}_g) \geq r_{gk}^p, \quad (5.14d)$$

$$C4 : \text{Tr} \left(\mathbf{p}_g^c + \sum_{i=1}^K \mathbf{p}_{gi}^p \right) \leq P_{tot}, \quad (5.14e)$$

$$C5 : \bar{r}_{gk}^c \geq 0 \text{ and } r_{gk}^p \geq 0, \quad (5.14f)$$

$$C6 : \mathbf{P}_g \succeq 0, \quad (5.14g)$$

$$C7 : \text{Rank}(\mathbf{P}_g) = 1, \quad (5.14h)$$

where

$$A_{gk}^c(\mathbf{P}_g) = \log_2 \left(\rho \mathbf{h}_{gk} \mathbf{P}_g^c \mathbf{h}_{gk}^H \alpha_g^c + \rho \sum_{i=1}^K \mathbf{h}_{gk} \mathbf{P}_i^p \mathbf{h}_{gk}^H \alpha_{gi}^p + 1 \right), \forall k, \forall g, \quad (5.15)$$

$$B_{gk}^c(\mathbf{P}_g) = -\log_2 \left(\rho \sum_{i=1}^K \mathbf{h}_{gk} \mathbf{P}_{gi}^p \mathbf{h}_{gk}^H \alpha_{gi}^p + 1 \right), \forall k, \forall g, \quad (5.16)$$

$$\begin{aligned} C_{gk}^p(\mathbf{P}_g) &= \log_2 \left(\rho \mathbf{h}_{gk} \mathbf{P}_g^c \mathbf{h}_k^H \alpha_g^c \epsilon + \rho \sum_{i \neq k}^K \mathbf{h}_{gk} \mathbf{P}_{gi}^p \mathbf{h}_{gk}^H \alpha_{gi}^p + \right. \\ &\quad \left. \rho \sum_{i=1}^K \mathbf{h}_{gk} \mathbf{P}_{gi}^p \mathbf{h}_{gk}^H \alpha_{gi}^p + 1 \right), \forall k, \forall g, \end{aligned} \quad (5.17)$$

$$D_{gk}^p(\mathbf{P}_g) = -\log_2 \left(\rho \mathbf{h}_{gk} \mathbf{P}_g^c \mathbf{h}_{gk}^H \alpha_g^c \epsilon + \rho \sum_{i \neq k}^K \mathbf{h}_{gk} \mathbf{P}_{gi}^p \mathbf{h}_{gk}^H \alpha_{gi}^p + 1 \right), \forall k, \forall g, \quad (5.18)$$

where $\mathbf{P}_g^c = \mathbf{p}_g^c \mathbf{p}_g^{cH}$ and $\mathbf{P}_{gk}^p = \mathbf{p}_{gk}^p \mathbf{p}_{gk}^{pH}$, with $g \in \mathcal{G}$ and $k \in \mathcal{K}$, Ω_g is an auxiliary optimization variable, $\text{Tr}(\cdot)$ denotes the trace of a matrix, and $\text{Rank}(\cdot)$ means the rank of a matrix. Since the elements of constraints (5.14c) and (5.14d) are concave, specifically (5.15) and (5.17), while (5.16) and (5.18) are non-convex, the problem (5.14a) is non-convex. However, these constraints are expressed in the form of difference of convex functions. Thus, (5.14c) and (5.14d) can be rewritten by their corresponding lower bound functions to tackle the non-convex parts. In addition, constraints (5.14g) and (5.14h) are imposed to guarantee that \mathbf{P}_g holds after optimization, in which the rank-one constraint in (5.14h) can be tackled by applying semi-definite relaxation technique. In particular, for handling the non-convex parts of constraints (5.14c) and (5.14d), we use the proposition similar to the one presented in Chapter 4, as follows

Proposition 1 [0]: Let $a \in \mathbb{R}^{1 \times 1}$ be a positive scalar and $f(a) = -(ab/\ln 2) + \log_2 a + (1/\ln 2)$.

It follows that

$$-\log_2 b = \max_{a>0} f(a), \quad (5.19)$$

and the optimal solution to the right-hand side of (5.19) is $a = 1/b$.

Proof: Since $f(a)$ is concave, the optimal solution to the right-hand side of (5.19) is obtained by setting $\partial f(a)/\partial a = 0$. ■

By applying Proposition (5.19) in (5.14a), we transform the elements (5.16) and (5.18) into convex optimization problems. In the t -th iteration, we approximate $B_{gk}^c(\mathbf{P}_g)$ and $D_{gk}^p(\mathbf{P}_g)$ as affine functions by using their corresponding lower bound functions. Thus, we have the following problems

$$B_{gk}^c(\mathbf{P}_g) \geq \max_{\varrho_{gk}^c \in \mathbb{R}^{1 \times 1}, \varrho_{gk}^c > 0} \xi_{gk}^c(\varrho_{gk}^c), \forall k \in \mathcal{K}, \forall g \in \mathcal{G}, \quad (5.20)$$

$$D_{gk}^p(\mathbf{P}_g) \geq \max_{\varrho_{gk}^p \in \mathbb{R}^{1 \times 1}, \varrho_{gk}^p > 0} \xi_{gk}^p(\varrho_{gk}^p), \forall k \in \mathcal{K}, \forall g \in \mathcal{G}, \quad (5.21)$$

where

$$\xi_{gk}^c(\varrho_{gk}^c) = -\frac{\varrho_{gk}^c}{\ln 2} \left(\rho \sum_{i=1}^K \mathbf{h}_{gi} \mathbf{P}_{gi}^p \mathbf{h}_{gi}^H \alpha_{gi}^p + 1 \right) + \log_2(\varrho_{gk}^c) + \frac{1}{\ln 2}, \quad (5.22)$$

and

$$\begin{aligned} \xi_{gk}^p(\varrho_{gk}^p) = & -\frac{\varrho_{gk}^p}{\ln 2} \left(\rho \mathbf{h}_{gk} \mathbf{P}_g^c \mathbf{h}_{gk}^H \alpha_g^c + \rho \sum_{i \neq k}^K \mathbf{h}_{gi} \mathbf{P}_{gi}^p \mathbf{h}_{gi}^H \alpha_{gi}^p + 1 \right) \\ & + \log_2(\varrho_{gk}^p) + \frac{1}{\ln 2}. \end{aligned} \quad (5.23)$$

According to the Proposition 1, when the optimal $\mathbf{P}_g^{(t)}$ in the $(t - 1)$ -th iteration, which is denoted by $\mathbf{P}_g^{(t-1)}$, is obtained, ϱ_{gk}^c and ϱ_{gk}^p can be updated in the t -th iteration by solving

$$\begin{aligned}\varrho_{gk}^{c(t)} = \max_{\varrho_{gk}^c > 0} & -\frac{\varrho_{gk}^c}{\ln 2} \left(\rho \sum_{i=1}^K \mathbf{h}_{gk} \mathbf{P}_{gi}^{p(t-1)} \mathbf{h}_{gk}^H \alpha_{gi}^p + 1 \right) \\ & + \log_2(\varrho_{gk}^c) + \frac{1}{\ln 2}, \forall k \in \mathcal{K}, \forall g \in \mathcal{G},\end{aligned}\quad (5.24)$$

and

$$\begin{aligned}\varrho_{gk}^{p(t)} = \max_{\varrho_{gk}^p > 0} & -\frac{\varrho_{gk}^p}{\ln 2} \left(\rho \mathbf{h}_{gk} \mathbf{P}_g^{c(t-1)} \mathbf{h}_{gk}^H \alpha_g^c \epsilon + \rho \sum_{i \neq k}^K \mathbf{h}_{gk} \mathbf{P}_{gi}^{p(t-1)} \mathbf{h}_{gk}^H \alpha_{gi}^p + 1 \right) \\ & + \log_2(\varrho_{gk}^p) + \frac{1}{\ln 2}, \forall k \in \mathcal{K}, \forall g \in \mathcal{G}.\end{aligned}\quad (5.25)$$

Since perfect Channel Status Information (CSI) at the BS is assumed, (5.24) and (5.25) can be rewritten, respectively, as [0]

$$\varrho_{gk}^{c(t)} = \left(\rho \sum_{i=1}^K \mathbf{h}_{gk} \mathbf{P}_{gi}^{p(t-1)} \mathbf{h}_{gk}^H \alpha_{gi}^p + 1 \right)^{-1}, \quad (5.26)$$

and

$$\varrho_{gk}^{p(t)} = \left(\rho \mathbf{h}_{gk} \mathbf{P}_g^{c(t-1)} \mathbf{h}_{gk}^H \alpha_g^c \epsilon + \rho \sum_{i \neq k}^K \mathbf{h}_{gk} \mathbf{P}_{gi}^{p(t-1)} \mathbf{h}_{gk}^H \alpha_{gi}^p + 1 \right)^{-1}. \quad (5.27)$$

Based on the solution $\mathbf{P}_g^{(t-1)}$ obtained in the $(t - 1)$ -th iteration, the global underestimation of $B_{gk}^c(\mathbf{P}_g)$ in (5.16) can be iteratively approximated at the t -th iteration. Then, $B_{gk}^c(\mathbf{P}_g)$ can be re-expressed based on its lower bound function, given by $\ddot{B}_{gk}^c(\mathbf{P}_g^{(t-1)})$ as follows

$$\begin{aligned}\ddot{B}_{gk}^c(\mathbf{P}_g^{(t-1)}) = \max_{\varrho_{pk}^{c(t)} > 0} & -\frac{\varrho_{pk}^{c(t)} \left(\rho \sum_{i=1}^K \mathbf{h}_{gk} \mathbf{P}_{gi}^{p(t)} \mathbf{h}_{gk}^H \alpha_{gi}^p + 1 \right)}{\ln 2} \\ & + \log_2(\varrho_{pk}^{c(t)}) + \frac{1}{\ln 2}, \forall k \in \mathcal{K},\end{aligned}\quad (5.28)$$

In a parallel avenue, in t -th iteration $D_{gk}^p(\mathbf{P}_g)$ in (5.18) is replaced by its lower bound. Its corresponding lower bound solution is given by $\ddot{D}_{gk}^p(\mathbf{P}_g^{(t-1)})$, as follows

$$\begin{aligned}\ddot{D}_{gk}^p(\mathbf{P}_g^{(t-1)}) = \max_{\varrho_{gk}^{p(t)} > 0} & -\frac{\varrho_{gk}^{p(t)} \left(\rho \mathbf{h}_{gk} \mathbf{P}_g^{c(t)} \mathbf{h}_{gk}^H \alpha_g^c \epsilon + \rho \sum_{i \neq k}^K \mathbf{h}_{gk} \mathbf{P}_{gi}^{p(t)} \mathbf{h}_{gk}^H \alpha_{gi}^p + 1 \right)}{\ln 2} \\ & + \log_2(\varrho_{gk}^{p(t)}) + \frac{1}{\ln 2}, \forall k \in \mathcal{K},\end{aligned}\quad (5.29)$$

As a result, the problem (5.14a) can be expressed based on its lower bound functions and, therefore, reformulated as follows

$$\max_{\mathbf{P}_g^{(t)}, \bar{\mathbf{r}}_g^c, \mathbf{r}_g^p, \Omega_g} \Omega_g, \quad (5.30a)$$

subject to

$$C1 : R_{gk}^{\text{tot}} \geq \Omega_g, \quad (5.30b)$$

$$C2 : A_{gk}^c(\mathbf{P}_g^{c(t)}) + \ddot{B}_{gk}^c(\mathbf{P}_g^{c(t-1)}) \geq \sum_{i=1}^K \bar{r}_{gi}^c, \quad (5.30c)$$

$$C3 : C_{gk}^p(\mathbf{P}_{gk}^{p(t)}) + \ddot{D}_{gk}^p(\mathbf{P}_{gk}^{p(t-1)}) \geq r_{gk}^p, \quad (5.30d)$$

$$C4 : \text{Tr}(\mathbf{P}_g^c + \sum_{k=1}^K \mathbf{P}_{gk}^p) \leq P_{tot}, \quad (5.30e)$$

$$C5 : \bar{r}_{gk}^c \geq 0 \text{ and } r_{gk}^p \geq 0, \quad (5.30f)$$

$$C6 : \mathbf{P}_g \succeq 0, \quad (5.30g)$$

$$C7 : \text{Rank}(\mathbf{P}_g^c) = 1, \text{ Rank}(\mathbf{P}_{gk}^p) = 1. \quad (5.30h)$$

One can notice that the problem (5.30a) consists of an SDP problem. Thus, one can use the AO approach to design a suboptimal iterative algorithm in order to optimize $\varrho_{gk}^{c(t)}$, $\varrho_{gk}^{p(t)}$, and \mathbf{P}_g , $\forall k \in \mathcal{K}$, and $\forall g \in \mathcal{G}$, at each iteration. If the optimal matrix solutions to the problem (5.30a) are rank one, then the optimal precoders are defined as the optimal solution to the problem. To verify that the relaxed problem satisfies the rank-one condition, the following proposition is presented.

Proposition 2: The solution \mathbf{P}_g^* of the problem (5.30a) satisfies the rank-one conditions.

Proof: Please refer to Appendix A.

Thus, by performing an eigenvalue decomposition on the solution \mathbf{P}_g^* , the beamforming vector that maximizes the achievable rate is obtained by selecting the principal eigenvector. The proposed algorithm to realize the above alternating optimization is summarized in Algorithm 6 in Chapter 4.

Remark: The complexity of solving an SDP problem is $O(n_{\text{sdp}}^{1/2} \cdot (m_{\text{sdp}} n_{\text{sdp}}^3 + m_{\text{sdp}}^2 n_{\text{sdp}}^2 + m_{\text{sdp}}^3)) \cdot \log(1/\tau)$ [0], where m_{sdp} is the number of semidefinite cone constraints, n_{sdp} represents the dimension of the semidefinite cone, and τ denotes the accuracy of solving the problem. Since we have T number of alternating optimization, $m_{\text{sdp}} = 7$ and $n_{\text{sdp}} = (N + 1)$, the computational complexity of the problem can be expressed as

$$T \cdot O(7(N + 1)^{\frac{7}{2}} + 49(N + 1)^{\frac{5}{2}} + 343(N + 1)^{\frac{1}{2}}) \cdot \log(\frac{1}{\tau}). \quad (5.31)$$

5.4 Phase-shift and Trajectory optimization with LSTM

5.4.1 Long Short-Term Memory Networks

LSTM are part of a group of architectures called RNN, which are a family of neural networks widely used for models whose problems are characterized by data sequences [0]. These two types of networks differ from other neural networks since the network parameters are shared along several points of the sequence under analysis. The outputs of the previous elements influence each one of the output elements. This particularity of persistence of the characteristics present in the data allows the model to look at a sequence as a whole and not just at an individual element. Unlike other networks, RNNs use feedback from activation's from previous time slots as input from the

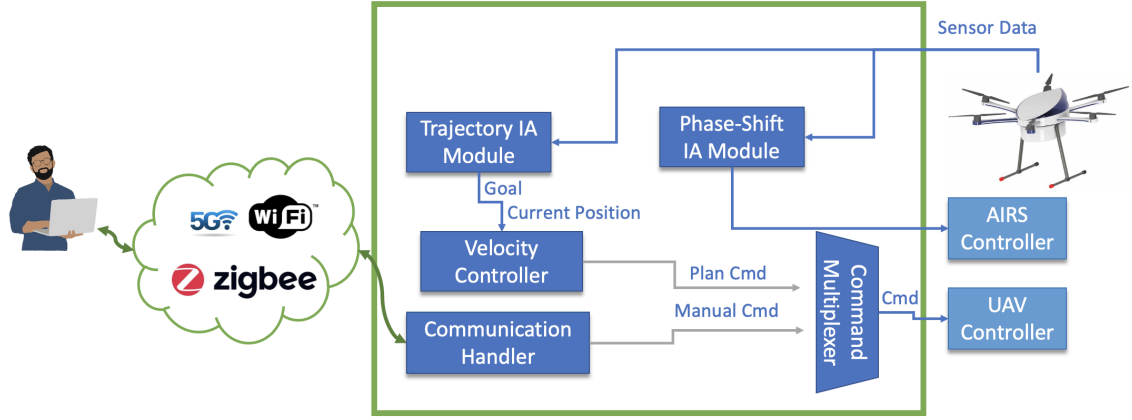


Figure 5.2: Architecture of the proposed system.

network to make a decision for the current input. It should be noted that the sequences that the RNN analyzes correspond to a time interval δ , which may not refer precisely to the phenomenon of time duration in the real world.

5.4.2 Trajectory

The observation space used to train the network is composed of the location of the UAV and the sum-rate experienced by each group at the t -th interval of time. Since the training process is performed by considering two groups, the observation space for trajectory optimization can be expressed as

$$S^\dagger = \left[x_l^t, y_l^t, z_l^t, \sum_{k=1}^K R_{1k}^{\text{tot},t}, \sum_{k=1}^K R_{2k}^{\text{tot},t} \right]. \quad (5.32)$$

As shown in Fig. 5.2 the S^\dagger is represented by the sensor data where there is a Global Positioning System (GPS), an AIRS and also an Inertial Measurement Unit (IMU). The information from these sensors will feed two Artificial Intelligence (AI) modules, the module for trajectory prediction and the module for phase-shift prediction (the second module will be explained in Section 5.4.3). As for the trajectory AI module, it receives the UAV's current position and the rate of each user group and returns the next UAV position to be reached. To generate the UAV's next position, the parameters that were used to train the network are shown in Table 5.1 and Algorithm 7, where N_n denotes the amount of neurons in each layer, the input is equal to 5 which represents the current 3D UAV position (x , y and z) and the sum-rate experienced by each group. The model was implemented using Matlab with Deep Learning Tool Box associated. The model was also trained on a laptop with NVIDIA GeForce GTX 1060, 16GB RAM and Intel Core i7-8750H CPU @ 2.20GHz x 12.

When this position is generated by the trajectory AI module, this result will feed the drone's velocity controller so that it can adapt its current speed until it reaches the desired destination. This controller extends a proportional–integral–derivative (PID) controllers, where the variables change depending on the type of UAV, the UAV's velocity calculation on the three axes were based on [0], where:

Table 5.1: The proposed custom RNN architecture hyperparameters for AI trajectory model.

Layer	Output	Hyperparameters
INPUT	5x1	
LSTM_1	600	$N_n = 1440000$;
FC OUTPUT	3	$N_n = 1803$; optm=ADAM loss=Mean Square Error

Algorithm 7 The proposed training model phase of section 5.4.2.

Require: $e = 1, \dots, N$, $LSTM_1 = 600$,

- 1: //Build the Deep Learning Model
- 2: **for** $e = 1, \dots, N$ **do**
- 3: $model[0] \leftarrow input$
- 4: $model[1] \leftarrow LSTM_1$
- 5: $model[2] \leftarrow FNN$
 //Compile Model
- 6: $model \leftarrow Loss = \text{Mean Square Error}$
- 7: $model \leftarrow Optimizer = \text{Adam}$
 //Train Model
- 8: $model \leftarrow Dataset$
 //Score model evaluation and save it
- 9: $results \leftarrow model.save$
- 10: **end for**

$$\hat{\mathbf{e}}\hat{\mathbf{P}}^{(t)} = \hat{\mathbf{g}}\hat{\mathbf{P}}^{(t)} - \hat{\mathbf{c}}\hat{\mathbf{P}}^{(t)}, \quad (5.33)$$

and

$$\hat{\mathbf{e}}\hat{\mathbf{D}}^{(t)} = \|(\hat{\mathbf{e}}\hat{\mathbf{Q}}^{(t)})\|, \quad (5.34)$$

where $\hat{\mathbf{e}}\hat{\mathbf{Q}}^{(t)}$ represents the error position, $\hat{\mathbf{g}}\hat{\mathbf{Q}}^{(t)}$ the goal position, $\hat{\mathbf{c}}\hat{\mathbf{Q}}^{(t)}$ the current position at time instant t , and $\hat{\mathbf{e}}\hat{\mathbf{D}}^{(t)}$ is the distance error position $\hat{\mathbf{e}}\hat{\mathbf{Q}}^{(t)}$.

With (5.33) and (5.34) it is possible to normalize the error as follows

$$\hat{\mathbf{e}}\hat{\mathbf{N}}^{(t)} = \frac{\hat{\mathbf{e}}\hat{\mathbf{P}}^{(t)}}{\hat{\mathbf{e}}\hat{\mathbf{D}}^{(t)}}, \quad (5.35)$$

where $\hat{\mathbf{e}}\hat{\mathbf{N}}^{(t)}$ is the error normalized. If the distance is lower than a certain threshold, τ (in this work, the threshold value is set to $\tau = 5$ meters, obtained by calculating the Euclidean distance for the coordinates x and y), (5.36) is activated.

$$\hat{\mathbf{v}}\hat{\mathbf{Q}}^{(t)} = \hat{\mathbf{e}}\hat{\mathbf{Q}}^{(t)} \cdot \left(\frac{\hat{\mathbf{e}}\hat{\mathbf{D}}^{(t)}}{\tau} \right)^{\hat{SF}}, \quad (5.36)$$

where $\hat{\mathbf{v}}\hat{\mathbf{Q}}^{(t)}$ is the velocity vector and \hat{SF} is the Smooth Factor (the \hat{SF} was set to 2 [0]). If the distance is higher than 5 meters (threshold), (5.37) is then used.

$$\hat{\mathbf{v}}\hat{\mathbf{Q}}^{(t)} = \hat{\mathbf{e}}\hat{\mathbf{N}}^{(t)} \cdot P\hat{M}V. \quad (5.37)$$

In (5.37), $P\hat{M}V = 2$ denotes the Param Max Velocity.

In this way, it is allowed to dynamically vary the UAV speed depending on the UAV distance in relation to the desired destination without any sudden changes regarding the UAV's acceleration.

The Command Multiplexer module subscribes to the manual topic controlled by a human and the trajectory AI module and prioritizes the manual topic in order to increase the safety of the UAV's navigation.

5.4.3 Phase-shift

While the AI module in section 5.4.2 predicts the next UAV position, this section will describe how the phase-shift for each user group is optimized. In particular, the observation space used as input to train the LSTM consists of UAV position, a phase vector, and the data related to the centroid of each group. In the training process, the phase-shift of the l -th element of the AIRS is chosen from an action set. Specifically, a set of actions is created, which is composed of different phase vectors of size L resulting from the permutation of possible values in (5.6). Then, at each instant of time t , the system takes an action from the action set. In the end, for each group of users, the action that maximizes the sum-rate is chosen. Therefore, we obtain the phase change that maximizes the rate of each group for a specific UAV position. This phase vector, also called action set, is used as input to the LSTM, as well as the UAV position and the coordinates of the centroid of the g -th group. Then, the observation space for phase shift optimization can be expressed as

$$S^{\ddagger} = \left[x_l^t, y_l^t, z_l^t, x_g^c, y_g^c, \theta_{g1}^* \cdots \theta_{gL}^* \right]. \quad (5.38)$$

where x_g^c and y_g^c denote the coordinates x and y of the centroid of the g -th group and θ_{gl}^* denotes the phase of the l -th element of the AIRS.

To generate the AIRS's next phase-shift, the parameters that were used to train the network are shown in Table 5.2 and Algorithm 8, where the input is the current phase-shift, the current UAV 3D position and the coordinates x_g^c and y_g^c of the centroid of the g -th group (65 values), the output is the next predicted phase-shift and N_n denotes the amount of neurons in each layer.

Table 5.2: The proposed custom RNN architecture hyperparameters for AI trajectory model.

Layer	Output	Hyperparameters
INPUT	65x1	
LSTM_1	600	$N_n = 1598400$;
LSTM_2	600	$N_n = 2882400$;
FC OUTPUT	60	$N_n = 36060$; optm=ADAM loss=Mean Square Error

While in Section 5.4.2 only one LSTM layer was used to build the model, in this section, as the network input is larger, it is necessary to increase the size of the network's LSTM layer. As mentioned in [0], it is better to split the LSTM layer into more than one to improve performance and reduce the complexity of the network, making the model more tiny, rather than increasing the size of just one LSTM layer. Another advantage of making the model more tiny is the ability to run

Algorithm 8 The proposed training model phase of section 5.4.3.

Require: $e = 1, \dots, N$, $LSTM_1 = 600$, $LSTM_2 = 600$,

- 1: //Build the Deep Learning Model
- 2: **for** $e = 1, \dots, N$ **do**
- 3: $model[0] \leftarrow input$
- 4: $model[1] \leftarrow LSTM_1$
- 5: $model[2] \leftarrow LSTM_2$
- 6: $model[3] \leftarrow FNN$
- //Compile Model
- 7: $model \leftarrow Loss = \text{Mean Square Error}$
- 8: $model \leftarrow Optimizer = Adam$
- //Train Model
- 9: $model \leftarrow Dataset$
- //Score model evaluation and save it
- 10: $results \leftarrow model.save$
- 11: **end for**

these algorithms directly on the UAV, making the response action faster than sending and receiving the information via the cloud [0].

5.5 Results

In this section, simulation results are provided to evaluate the performance of the proposed method. It is considered a scenario with $N = 4$ antennas at the BS and $K = 3$ single-antenna users per group, which are positioned in a cell of radius of 200 m. The UAV continuously flies, following the height range $20 \leq z \leq 60$ in meters, and an IRS with $L = 60$ reflective elements is fitted to the UAV. In particular, it is assumed $\ddot{b} = 2$, $\nu = 2.2$, $\alpha_g^c = 0.9$, $\alpha_{gk}^p = 0.05 \forall k \in \mathcal{K}$, $\tau = 10^{-3}$, $T_{\max} = 10^3$, and $\beta_0 = 1000$. The parameter β_0 is adjusted based on the desired performance of the receivers [0]. For AIRS-NOMA scenario, it is considered $\alpha_{g1} = 0.7$, $\alpha_{g2} = 0.2$, and $\alpha_{g3} = 0.1$. When not specified, the value for SNR is set as 40 dB. In addition, it is assumed that the power consumption of IRS is 3 mW per element.

5.5.1 Training Progress

One of the crucial phases in the development of this system is the training phase for the models proposed in Sections 5.4.2 and 5.4.3. By exploring the static scenario, Fig. 5.3a depicts the AIRS's trajectory in the training process based on the learning policy to find the centroid of the static user groups, as described in Section 5.4. In this figure, one can see that the UAV explores 50 starting points. The AIRS starts from one of these points and, at each time t , recalculates the distance to the center of the user groups based on linear equation. The coefficients of the equation of line are updated at each time t . Then, an observation space is generated by considering the data obtained for each starting point, as expressed in equations (5.32) and (5.38).

Similarly, Fig. 5.3b shows the training process, but now exploring the dynamic scenario. The learning policy is formulated by considering that the users are in movement, and a new observation

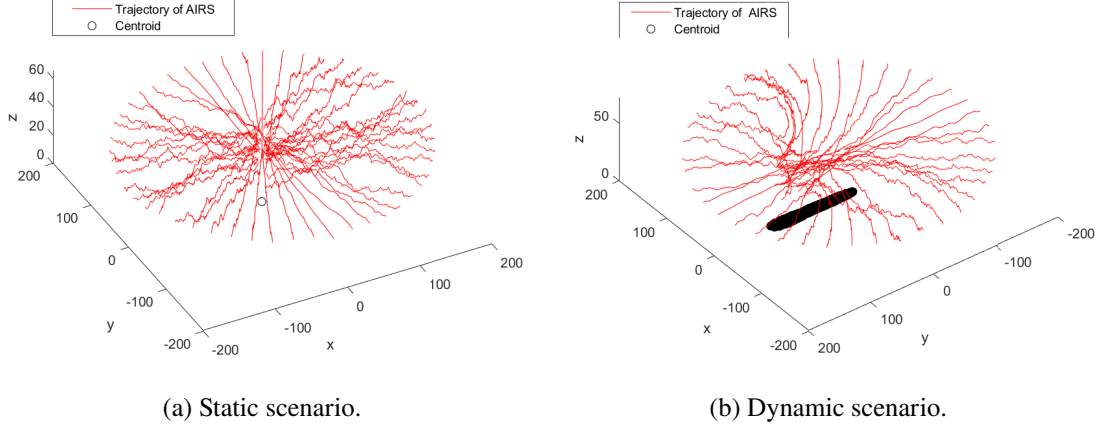


Figure 5.3: Generating the observation space.

space is generated. The observation spaces are used as input to the LSTM networks to predict the trajectory and phase-shift. In addition to the static and dynamic user group data that feeds the LSTM individually, further training was carried out in which this data (static and dynamic) is grouped together and fed into another LSTM network to also evaluate this information.

As the model for predicting the phase-shift is more complex than the model for predicting the trajectory (trajectory network returns 3 output values, while the phase-shift network returns a vector of size L , where $L > 3$), the number of epochs of the phase-shift will have to be higher in order to have an algorithm that can learn and predict with good performance. Thus, the model in Section 5.4.2 has a number of epochs equal to 200, while the model in section 5.4.3 was set to 500 epochs. The results in terms of Root Mean Squared Error (RMSE) and loss can be observed in Figs. 5.4 and 5.5.

As can be seen in Figs. 5.4 and 5.5, the model that predicts the trajectory manages to converge more quickly than the model that predicts the phase-shift. This is due to the complexity of the network's input values, where the first model only needs five variables, and the second needs an input 13 times larger to predict the phase-shift. The other reason for the difference in convergence has to do with the complexity of the network, where the second model has approximately 5 million parameters to optimize, while the first is almost 5 times smaller.

In terms of RMSE and Loss for the trajectory models, the static model has an RMSE of 0.171 with a training loss of 1.46%, the dynamic model has an RMSE of 0.168 with a training loss of 1.42% and the mix model (static and dynamic together) has an RMSE of 0.164 with a final loss of 1.35%. Although the results are very close, it is possible to recognize that the results of the model that uses static and dynamic information to predict the trajectory are better compared to the other 2 models in the training phase. This is due to the fact that the other 2 models were only trained with one type of data (either only static information or only dynamic information). In addition, it is also possible to observe the peaks in both figures due to two possible reasons: the regularization put in place during the training phase (L2 regularization method) and the attempt to converge to a minimum (local or global).

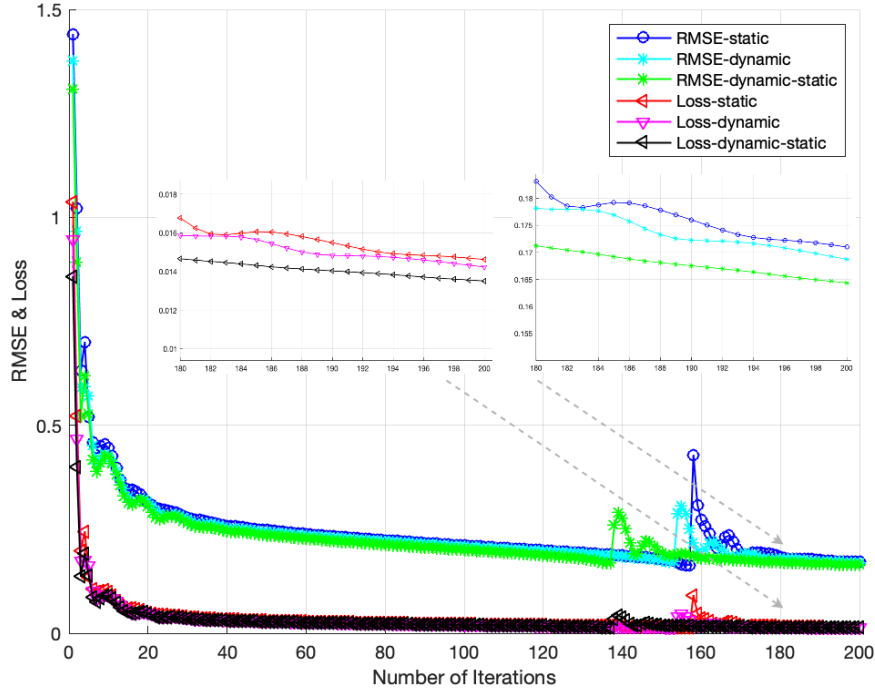


Figure 5.4: RMSE and loss training results for trajectory model with the static and dynamic group movement.

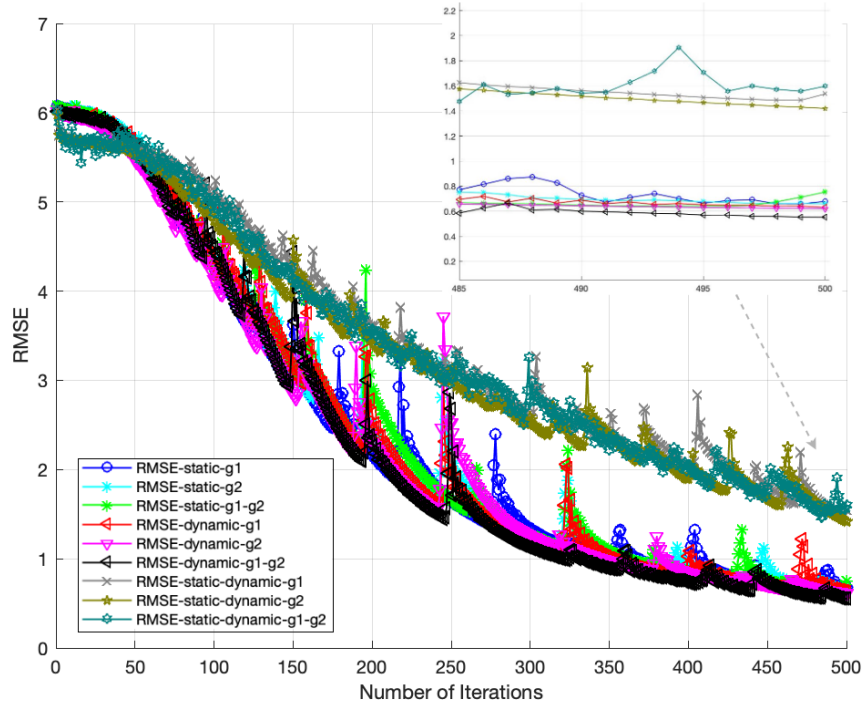


Figure 5.5: RMSE and loss training results for phase-shift model with the static and dynamic group movement.

As can be observed in Fig. 5.5, although both models (static, dynamic, and mix) converge throughout the training phase, it can be concluded that using both pieces of information (static and dynamic) to predict the phase-shift of the AIRS makes the model less effective at predicting it, having a RMSE higher than 1.4, while models that only use one type of information manage to be below 1 in RMSE. Concerning the models that only use one type of information, the results are quite close, but the dynamic model achieves better results.

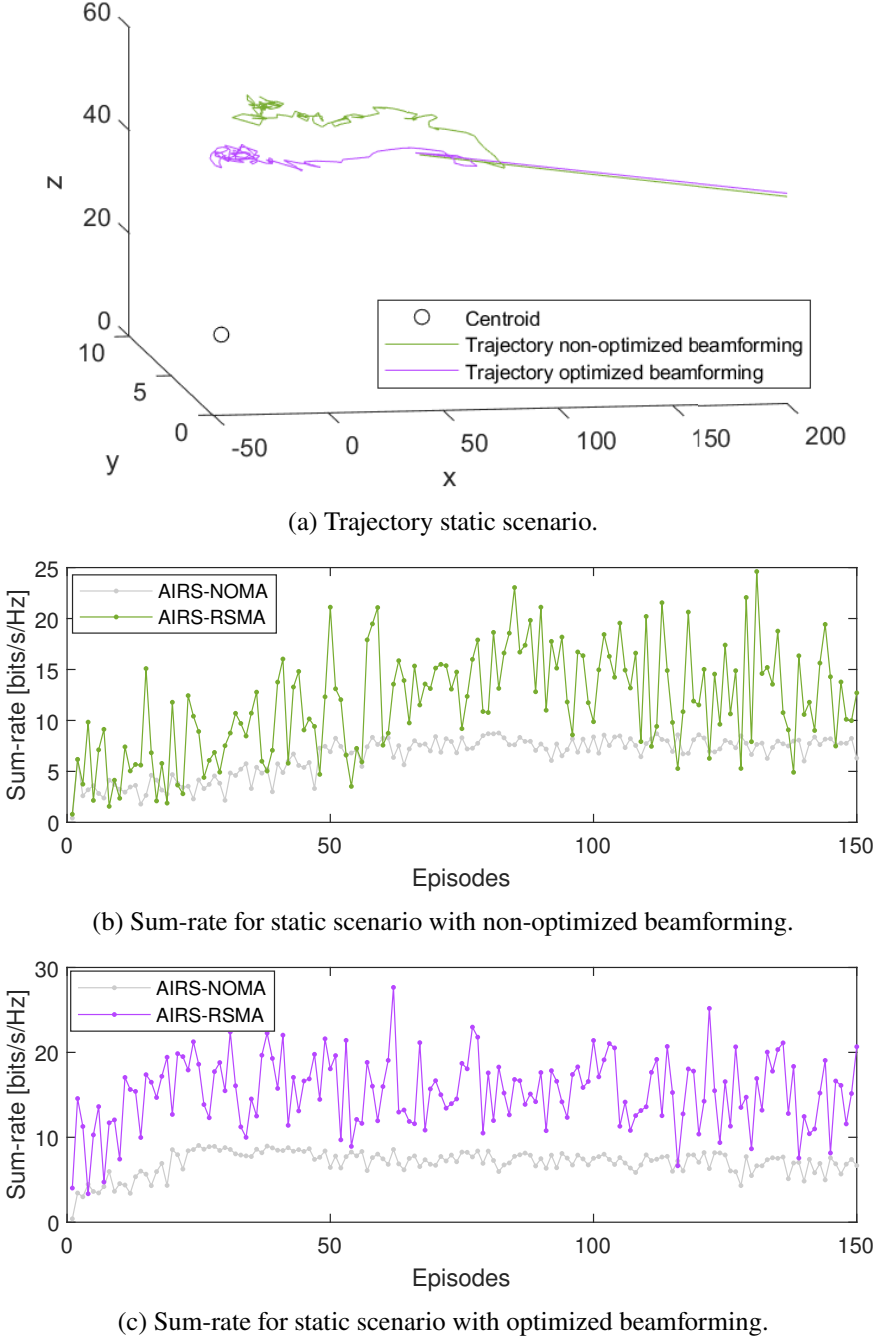
5.5.2 Performance Analysis

In order to demonstrate the potential of the proposed methods, this subsection provides testing and performance results for each investigated scenario. Fig. 5.6 depicts the trajectory of the UAV (Fig. 5.6a) and the sum-rate versus the episodes (Fig. 5.6b and Fig. 5.6c) in the proposed AIRS-RSMA network for a static scenario. The analysis considers both non-optimized, where a random precoder is used, and optimized beamforming approaches. For comparison, the AIRS-NOMA scheme is also plotted. The AIRS-NOMA scheme shows lower performance gains, as it is more susceptible to errors caused by imperfect SIC. In contrast, the AIRS-RSMA scheme can reduce and control decoding errors by adjusting the split of the common and private messages. By employing optimized beamforming, higher performance gains are achieved due to the capacity to redirect the signal, providing an adaptive beam between the BS and AIRS.

Fig. 5.7 shows the trajectory of the UAV (Fig. 5.7a) and the sum-rate versus the episodes (Fig. 5.7b and Fig. 5.7c) for a dynamic scenario, considering both optimized and non-optimized beamforming. It is evident that the application of optimized beamforming results in better and more stable rate gains throughout the episodes. Furthermore, in this scenario, the AIRS-RSMA network also outperforms the AIRS-NOMA.

Fig. 5.8 investigates the total sum-rate for the static scenario versus the transmit SNR. To compare the performance between the proposed DL methods, the joint dynamic-static (dyn-sta) and static (sta) models based on combining data from all user groups (g1-g2) are applied to predict the phase-shift (PS) and the trajectory (Traj) of the UAV. One can see that the static model achieves superior gains in terms of sum-rate when compared with dyn-sta model. In particular, when the SNR is 35 dB and $\epsilon = 0.1$, the static method achieves a performance of 23.7 bits/s/Hz, while dyn-sta can reach 20.1 bits/s/Hz. Since the combined model uses data from both static and dynamic scenarios, the UAV may follow a parabolic trajectory when it is not needed. Additionally, it is observed that the impact of the trajectory is greater than that of the phase-shift. This result is confirmed when the dyn-sta model is applied for PS optimization and the static model for trajectory optimization. In this case, the obtained sum-rate shows similar results to when the static model is used to predict both PS and trajectory.

Fig. 5.9 investigates the total sum-rate for the dynamic scenario versus the transmit SNR, in which the joint dyn-sta and dynamic models are applied. It is evident that the dynamic model outperforms the dyn-sta model. For instance, when the SNR is 35 dB and ϵ is 0.1, the dyn-sta method achieves a performance of 17.7 bits/s/Hz, while the dynamic model can reach 20.3 bits/s/Hz, representing a performance gain of approximately 12.8%. Additionally, it is observed that trajectory

Figure 5.6: Performance comparison static scenario with $\rho = 40$ dB and $\epsilon = 0.1$.

prediction also has a greater impact on the dynamic scenario.

In particular, by comparing the performance between Fig. 5.8 and Fig. 5.9, one can see that the static scenario achieves superior performance compared to the dynamic scenario. It is important to mention that the dynamic scenario represents the worst case. Additionally, the combined model (dyn-sta) achieves similar performance for both scenarios when the SNR is 40 dB. This is because the dyn-sta scheme is modeled by combining data from both scenarios, and the models were trained considering $\rho = 40$ dB. Note that it is possible to perform the training process for other values.

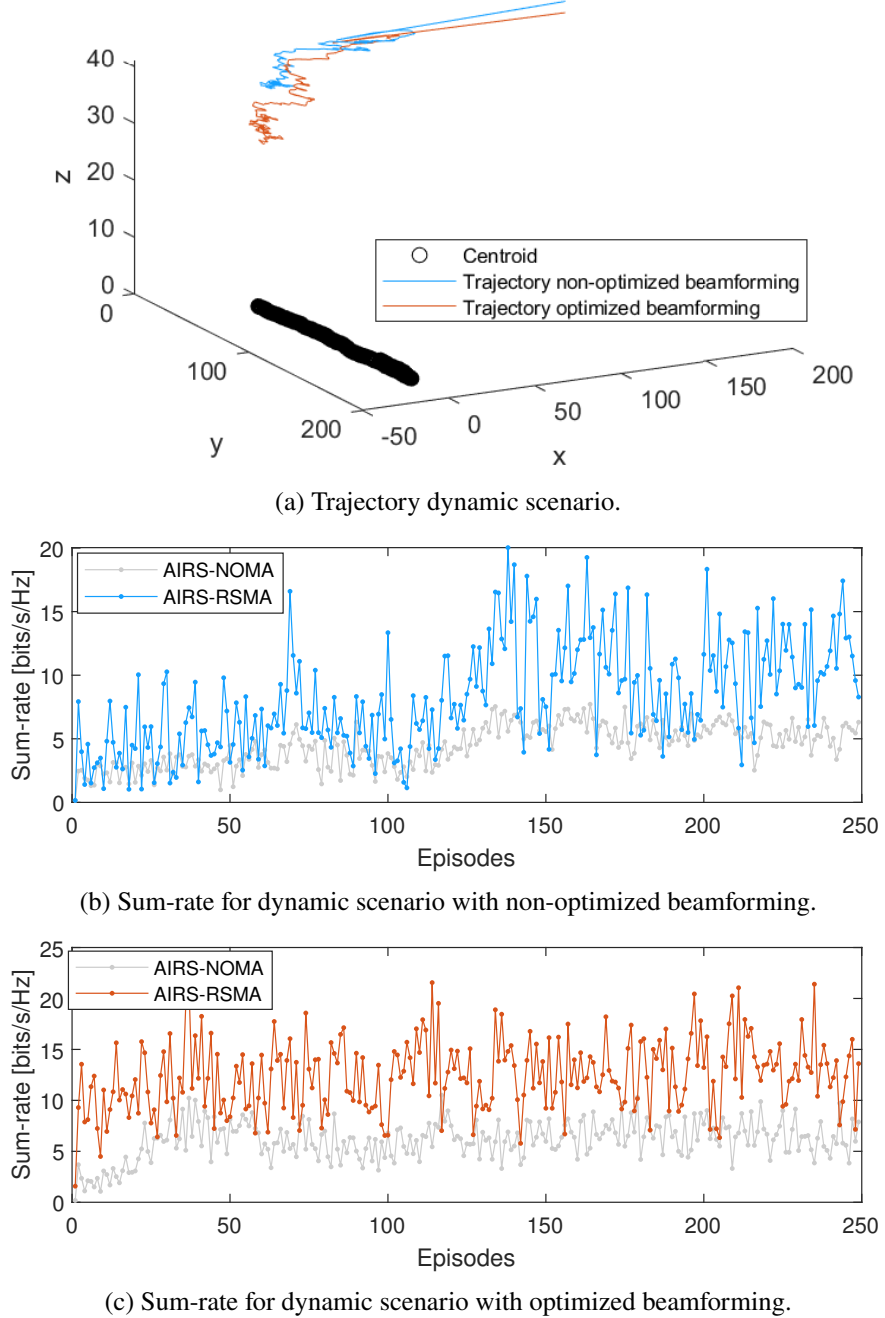


Figure 5.7: Performance comparison dynamic scenario with $\rho = 40$ dB and $\epsilon = 0.1$.

5.6 Conclusions

In this chapter, MISO-RSMA network with multiuser assisted by AIRS was investigated. The system model and the formulation for the beamforming problem were presented, such as a solution to handle it. To enhance the total achievable rate of the system, our focus was on predicting the characteristics of the environment. This involved predicting both the trajectory of the UAV and the phase-shift of the AIRS's elements, taking into account both static and dynamic scenarios. The

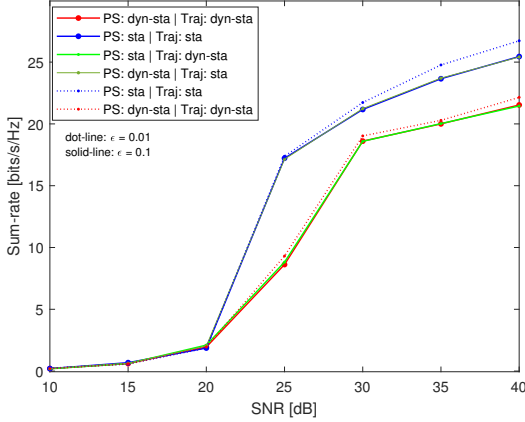


Figure 5.8: Sum-rate for AIRS-RSMA scheme versus transmit SNR for static scenario with different prediction models.

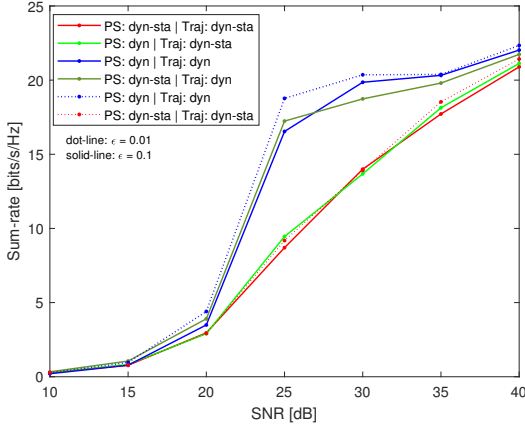


Figure 5.9: Sum-rate for AIRS-RSMA scheme versus transmit SNR for dynamic scenario with different prediction models.

DL framework LSTM is used to predict these features and, consequently, predicting models were proposed.

In particular, dynamic and static observation spaces were constructed based on real-time features of the environment, including the position of the UAV, the phase-shift vectors that maximize the sum-rate of each group at the t -th time, and the total sum-rate of the system. For more insightful results, the dynamic and static models were combined to create a third model. Finally, the proposed models were tested on the AIRS-RSMA network, and training, testing, and numerical results were presented for each scenario, in which the sum-rate is improved compared to the non-optimized beamforming AIRS-RSMA and AIRS-NOMA schemes. It is concluded that, despite the convergence of the models in the training phase for predicting trajectory and phase-shift, the trajectory model converges more quickly than the phase-shift model.

In addition, it has been validated that using static and dynamic information separately is more effective than combining them when predicting the next position in the trajectory and forecasting the phase-shift. Furthermore, it has been revealed that the trajectory has a more significant impact

CHAPTER 5. LSTM-BASED TRAJECTORY AND PHASE-SHIFT PREDICTION FOR RSMA NETWORKS ASSISTED BY AIRS

on the sum-rate compared to the phase-shift. The results also indicate that the combining model achieves similar performance for both scenarios. It is noteworthy that the insights provided can serve as a benchmark for future works. Since the observation spaces have been created, other DL models can be developed based on alternative frameworks to predict the features of the system in real-time.

Conclusions

The increasing number of network-connected devices, along with the inherent demands of services and applications, underscores the pivotal role of multiple access technologies in meeting the diverse requirements of future wireless communication. Concurrently, Intelligent Reflecting Surface (IRS) has emerged as a promising technology capable of intelligently enhancing the radio propagation environment in recent years. Current research on IRS primarily focuses on utilizing phase shifts to enhance the performance of transmitted signals. This approach enables IRS to achieve performance enhancements without the need for additional transmission power, resulting in an energy-efficient solution that distinguishes itself from other technologies. When mounted on an Unmanned Aerial Vehicle (UAV), IRS can effectively leverage the mobility and flexibility inherent in UAVs.

Building upon this foundation, this thesis embarked on a systematic exploration of multiple access techniques, IRS, and UAV to facilitate the communication between the base station and users. The initial phase involved a literature review, particularly focusing on the integration of UAVs into Non-Orthogonal Multiple Access (NOMA) networks. A specific issue pertaining to power allocation and user pairing was investigated. The quest for a solution led to an exploration of Reinforcement Learning (RL) approaches. Then, a method based on Multi-Armed Bandit (MAB) framework was proposed. The solution successfully enhanced the system's sum-rate by accurately identifying user pairs. Furthermore, the power coefficients were determined through a closed-form expression, further contributing to the effectiveness of the approach. Next, the interplay of IRS mounted on a UAV to improve the wireless propagation environment was investigated in depth. A comprehensive literature review about the integration of these technologies was carried out, as well as its architecture, functionality principles, and performance gains. In-depth discussions were conducted, and the analysis was substantiated with presented simulation results. The findings highlighted the considerable advantages that integrating IRS mounted on a UAV can offer to enhance network performance.

Employing the Rate-Splitting Multiple Access (RSMA) technique for medium access control, the integration of IRS into UAVs was explored again. This time, two-users scenarios was

considered and an optimization problem for beamforming between the Base Station (BS) and the Aerial Intelligent Reflecting Surface (AIRS) was formulated. Given its non-convex nature, the problem was transformed into a Semi-Definite Program (SDP) problem, enabling interactive resolution through Alternating Optimization (AO) methods. Simulation results demonstrated the rate improvements achieved by the proposed solution in the examined scenario. Furthermore, a performance comparison between RSMA and NOMA networks was conducted, highlighting the notable efficiency of the RSMA technique when compared to its counterpart.

Extending the analysis to a multi-user scenario, problems related to predicting the UAV's trajectory and the phase-shift of the IRS were investigated. A comprehensive review of existing solutions was conducted, leading us to opt for the application of machine learning tools to address the formulated problem. Due to the ability to effectively model and analyze sequential data, Long Short-Term Memory (LSTM) was in-depth investigated and applied to solve the problems. In addressing the multi-user context, users were organized into groups, and the trajectory of the UAV was meticulously computed to determine the centroid of each user group. The process commenced with the collection of data, incorporating the UAV's position and the sum rate of each group at time t . Subsequently, an observation space centered on the phase-shift was constructed. This involved selecting the phase-shift of each reflecting element from a quantized set, employing it to direct signals towards users. The phase-shift vector, which maximizes the rate for each user group, was then chosen to constitute the observation space, included both the UAV's position and the coordinates of the centroid for each user group. Since the observation spaces were created, two LSTM networks were developed in order to predict the trajectory and phase-shift. Note that, LSTMs play a crucial role in capturing patterns and dependencies within sequences, making them a powerful tool for tasks that involve understanding and predicting sequential information. The models were applied on the aerial IRS in MISO-RSMA (AIRS-RSMA) network, and validated by simulation, in which training, testing and performance results were presented.

The solutions presented in this Thesis play a role in solidifying Multiple Access (MA) techniques as viable tools for medium access management in the future generations of mobile communication. Furthermore, the discussions and findings presented substantiate results outlined in existing literature, portraying IRSs as a promising technology with low complexity of implementation, as there is no need for encoding and decoding messages intended for users. When integrated with UAV, IRS retain the ability to leverage the mobility and coverage advantages inherent in the flexible features of UAVs. A comparative analysis of the results reveals the clear superiority of the proposed methods over the relevant comparative schemes. This superiority renders them particularly appealing for applications and services demanding enhanced performance in terms of user capacity, coverage, and spectral efficiency.



Bibliography

- [0] J. A. del Peral-Rosado et al. “Survey of Cellular Mobile Radio Localization Methods: From 1G to 5G”. In: *IEEE Communications Surveys Tutorials* 20.2 (2018), pp. 1124–1148. doi: [10.1109/COMST.2017.2785181](https://doi.org/10.1109/COMST.2017.2785181) (cit. on p. 1).
- [0] X. Yuan et al. “Reconfigurable-intelligent-surface empowered wireless communications: Challenges and opportunities”. In: *IEEE Wirel. Commun.* 28.2 (Feb. 2021), pp. 136–143. doi: [10.1109/MWC.001.2000256](https://doi.org/10.1109/MWC.001.2000256) (cit. on pp. 1, 28, 32, 55).
- [0] B. K. S. Lima et al. “Aerial Intelligent Reflecting Surfaces in MIMO-NOMA Networks: Fundamentals, Potential Achievements, and Challenges”. In: *IEEE Open J. Commun. Soc.* 3 (2022), pp. 1007–1024. doi: [10.1109/OJCOMS.2022.3182223](https://doi.org/10.1109/OJCOMS.2022.3182223) (cit. on pp. 1, 67).
- [0] S. K. Sharma and X. Wang. “Toward massive machine type communications in ultra-dense cellular IoT networks: Current issues and machine learning-assisted solutions”. In: *IEEE Commun. Surv. Tutor.* 22.1 (2020), pp. 426–471. doi: [10.1109/COMST.2019.2916177](https://doi.org/10.1109/COMST.2019.2916177) (cit. on p. 5).
- [0] Y. Saito et al. “Non-orthogonal multiple access (NOMA) for cellular future radio access”. In: *IEEE 77th Veh. Technol. Conf.* (June 2013), pp. 1–5 (cit. on p. 5).
- [0] Z. Ding et al. “A survey on non-orthogonal multiple access for 5G networks: Research challenges and future trends”. In: *IEEE J. Sel. Areas Commun.* 35.10 (2017), pp. 2181–2195. doi: [10.1109/JSAC.2017.2725519](https://doi.org/10.1109/JSAC.2017.2725519) (cit. on p. 5).
- [0] Y. Liu et al. “Nonorthogonal multiple access for 5G and beyond”. In: *Proceedings of the IEEE* 105.12 (2017), pp. 2347–2381. doi: [10.1109/JPROC.2017.2768666](https://doi.org/10.1109/JPROC.2017.2768666) (cit. on pp. 5, 11).
- [0] M. Mozaffari et al. “A tutorial on UAVs for wireless networks: Applications, challenges, and open problems”. In: *IEEE Commun. Surv. Tutor.* 21.3 (2019), pp. 2334–2360. doi: [10.1109/COMST.2019.2902862](https://doi.org/10.1109/COMST.2019.2902862) (cit. on pp. 5, 28, 34).

BIBLIOGRAPHY

- [0] S. Hayat, E. Yanmaz, and R. Muzaffar. “Survey on unmanned aerial vehicle networks for civil applications: A communications viewpoint”. In: *IEEE Commun. Surv. Tutor.* 18.4 (2016), pp. 2624–2661. doi: [10.1109/COMST.2016.2560343](https://doi.org/10.1109/COMST.2016.2560343) (cit. on p. 5).
- [0] M. Mozaffari et al. “Mobile internet of things: Can UAVs provide an energy-efficient mobile architecture?” In: *IEEE Glob. Commun. Conf. (GLOBECOM)* (Dec. 2016), pp. 1–6. doi: [10.1109/GLOCOM.2016.7841993](https://doi.org/10.1109/GLOCOM.2016.7841993) (cit. on p. 6).
- [0] Z. Na et al. “UAV-supported clustered NOMA for 6G-enabled internet of things: Trajectory planning and resource allocation”. In: *IEEE Internet Things J.* PP (June 2020), pp. 1–1. doi: [10.1109/JIOT.2020.3004432](https://doi.org/10.1109/JIOT.2020.3004432) (cit. on p. 6).
- [0] Z. Qin et al. “Deep learning in physical layer communications”. In: *IEEE Wirel. Commun.* 26.2 (2019), pp. 93–99. doi: [10.1109/MWC.2019.1800601](https://doi.org/10.1109/MWC.2019.1800601) (cit. on p. 6).
- [0] D. Wang et al. “From IoT to 5G I-IoT: The next generation IoT-based intelligent algorithms and 5G technologies”. In: *IEEE Commun. Mag.* 56.10 (2018), pp. 114–120. doi: [10.1109/MCOM.2018.1701310](https://doi.org/10.1109/MCOM.2018.1701310) (cit. on p. 6).
- [0] Y. Huang et al. “Online maneuver design for UAV-enabled NOMA systems via reinforcement learning”. In: *2020 IEEE Wirel. Commun. Netw. Conf. (WCNC)*. May 2020, pp. 1–6. doi: [10.1109/WCNC45663.2020.9120492](https://doi.org/10.1109/WCNC45663.2020.9120492) (cit. on p. 6).
- [0] S. Khairy et al. “Constrained deep reinforcement learning for energy sustainable multi-UAV based random access IoT networks with NOMA”. In: *IEEE J. Sel. Areas Commun.* 39.4 (2021), pp. 1101–1115. doi: [10.1109/JSAC.2020.3018804](https://doi.org/10.1109/JSAC.2020.3018804) (cit. on p. 6).
- [0] Y. Zhang, Q. Wu, and M. Shikh-Bahaei. “A pointer network based deep learning algorithm for user pairing in full-duplex Wi-Fi networks”. In: *IEEE Trans. Veh. Technol.* 69.10 (2020), pp. 12363–12368. doi: [10.1109/TVT.2020.3011613](https://doi.org/10.1109/TVT.2020.3011613) (cit. on p. 6).
- [0] S. Maghsudi and E. Hossain. “Multi-armed bandits with application to 5G small cells”. In: *IEEE Wirel. Commun.* 23.3 (2016), pp. 64–73. doi: [10.1109/MWC.2016.7498076](https://doi.org/10.1109/MWC.2016.7498076) (cit. on pp. 6, 12).
- [0] Z. Tian et al. “Distributed NOMA-based multi-armed bandit approach for channel access in cognitive radio networks”. In: *IEEE Wirel. Commun. Lett.* 8.4 (2019), pp. 1112–1115. doi: [10.1109/LWC.2019.2908371](https://doi.org/10.1109/LWC.2019.2908371) (cit. on p. 6).
- [0] M. A. Adjif, O. Habachi, and J. .-. Cances. “Joint channel selection and power control for NOMA: A multi-armed bandit approach”. In: *2019 IEEE Wirel. Commun. Netw. Conf. (WCNC)*. May 2019, pp. 1–6. doi: [10.1109/WCNCW.2019.8902878](https://doi.org/10.1109/WCNCW.2019.8902878) (cit. on p. 6).
- [0] P. Pourbaba et al. “Multi-armed bandit learning for full-duplex UAV relay positioning for vehicular communications”. In: *2019 16th Proc. Int. Symp. Wirel. Commun. Syst. (ISWCS)*. Aug. 2019, pp. 188–192. doi: [10.1109/ISWCS.2019.8877122](https://doi.org/10.1109/ISWCS.2019.8877122) (cit. on p. 6).
- [0] Y. Lin, T. Wang, and S. Wang. “UAV-assisted emergency communications: An extended multi-armed bandit perspective”. In: *IEEE Commun. Lett.* 23.5 (2019), pp. 938–941. doi: [10.1109/LCOMM.2019.2906194](https://doi.org/10.1109/LCOMM.2019.2906194) (cit. on p. 7).

- [0] Y. Zhao, J. Lee, and W. Chen. “Q-greedyUCB: A new exploration policy to learn resource-efficient scheduling”. In: *China Commun.* 18.6 (June 2021), pp. 12–23 (cit. on p. 7).
- [0] M. A. Adjif, O. Habachi, and J.-P. Cances. “Joint Channel Selection and Power Control for NOMA: A Multi-Armed Bandit Approach”. In: *2019 IEEE Wirel. Commun. and Networking Conf. (WCNC)* (Nov. 2019), pp. 1–6 (cit. on p. 7).
- [0] C. Bettstetter, H. Hartenstein, and X. Costa-Pérez. “Stochastic properties of the random waypoint mobility model”. In: *Wirel. Netw.* 10 (2004), pp. 555–567 (cit. on p. 8).
- [0] F. Ono, H. Ochiai, and R. Miura. “A wireless relay network based on unmanned aircraft system with rate optimization”. In: *IEEE Trans. Wirel. Commun.* 15.11 (2016), pp. 7699–7708. doi: [10.1109/TWC.2016.2606388](https://doi.org/10.1109/TWC.2016.2606388) (cit. on p. 9).
- [0] C. You and R. Zhang. “3D trajectory optimization in rician fading for UAV-enabled data harvesting”. In: *IEEE Trans. Wirel. Commun.* 18.6 (Apr. 2019), pp. 3192–3207. doi: [10.1109/TWC.2019.2911939](https://doi.org/10.1109/TWC.2019.2911939) (cit. on p. 9).
- [0] 3. T. 36.777. *Enhanced LTE support for aerial vehicles*. 2021. URL: <https://portal.3gpp.org/ngppapp/CreateTdoc.aspx?mode=view%5C&contributionUid=RP-171050> (cit. on p. 9).
- [0] H. V. Cheng, E. Björnson, and E. G. Larsson. “Performance Analysis of NOMA in Training-Based Multiuser MIMO Systems”. In: *IEEE Trans. Wirel. Commun.* 17.1 (Oct. 2018), pp. 372–385 (cit. on p. 10).
- [0] C. Hu, H. Wang, and R. Song. “Group Successive Interference Cancellation Assisted Semi-Blind Channel Estimation in Multi-Cell Massive MIMO-NOMA Systems”. In: *IEEE Commun. Lett.* 25.9 (July 2021), pp. 3085–3089 (cit. on p. 10).
- [0] P. Auer, N. Cesa-Bianchi, and P. Fischer. “Finite-time Analysis of the Multiarmed Bandit Problem”. In: *J Mach. Learn.* 47 (May 2002), pp. 235–256. doi: [10.1109/TVT.2017.2752264](https://doi.org/10.1109/TVT.2017.2752264) (cit. on p. 13).
- [0] N. Cesa-Bianchi and G. Lugosi. “Combinatorial bandits”. In: *J. Comp. Sys. Sci.* 78.5 (Jan. 2012), pp. 1404–1422. issn: 0022-0000 (cit. on p. 15).
- [0] Z. Yang et al. “A general power allocation scheme to guarantee quality of service in downlink and uplink NOMA systems”. In: *IEEE Trans. Wirel. Commun.* 15.11 (2016), pp. 7244–7257. doi: [10.1109/TWC.2016.2599521](https://doi.org/10.1109/TWC.2016.2599521) (cit. on p. 16).
- [0] R. S. Sutton and A. G. Barto. *Reinforcement learning: an introduction*. Second. The MIT Press, 2018. URL: <http://incompleteideas.net/book/the-book-2nd.html> (cit. on p. 17).
- [0] T. Lattimore and C. Szepesvári. *Bandit Algorithms*. Cambridge University Press, 2020. doi: [10.1017/9781108571401](https://doi.org/10.1017/9781108571401) (cit. on p. 19).
- [0] V. Kuleshov and D. Precup. “Algorithms for multi-armed bandit problems”. In: *J. Mach. Learn. Res.* 1 (Feb. 2014) (cit. on p. 21).

BIBLIOGRAPHY

- [0] Z. Yang et al. “Novel relay selection strategies for cooperative NOMA”. In: *IEEE Trans. Veh. Technol.* 66.11 (2017), pp. 10114–10123. doi: [10.1109/TVT.2017.2752264](https://doi.org/10.1109/TVT.2017.2752264) (cit. on p. 24).
- [0] N. Nomikos et al. “Hybrid NOMA/OMA with buffer-aided relay selection in cooperative networks”. In: *IEEE J. Sel. Areas Commun.* 13.3 (2019), pp. 524–537. doi: [10.1109/JSTSP.2019.2894059](https://doi.org/10.1109/JSTSP.2019.2894059) (cit. on p. 24).
- [0] C. v. n. i. Cisco. “Global mobile data traffic forecast update, 2017–2022”. In: (Feb. 2019). URL: <https://www.statista.com/statistics/271405/global-mobile-data-traffic-forecast/> (cit. on p. 27).
- [0] Y. Yuan et al. “NOMA for next-generation massive IoT: Performance potential and technology directions”. In: *IEEE Commun. Mag.* 59.7 (July 2021), pp. 115–121. doi: [10.1109/MCOM.01.2000997](https://doi.org/10.1109/MCOM.01.2000997) (cit. on p. 27).
- [0] B. K. S. Lima et al. “Adaptive power factor allocation for cooperative full-duplex NOMA systems with imperfect SIC and rate fairness”. In: *IEEE Trans. Veh. Technol.* 69.11 (Oct. 2020), pp. 14061–14066. doi: [10.1109/TVT.2020.3029791](https://doi.org/10.1109/TVT.2020.3029791) (cit. on pp. 27, 41, 55, 63, 67).
- [0] Q. Wu and R. Zhang. “Towards smart and reconfigurable environment: intelligent reflecting surface aided wireless network”. In: *IEEE Commun. Mag.* 58.1 (2020), pp. 106–112. doi: [10.1109/MCOM.001.1900107](https://doi.org/10.1109/MCOM.001.1900107) (cit. on pp. 28, 32).
- [0] M. Di Renzo et al. “Smart radio environments empowered by reconfigurable intelligent surfaces: how it works, state of research, and road ahead”. In: *IEEE J. Sel. Areas Commun.* PP (July 2020), pp. 1–1. doi: [10.1109/JSAC.2020.3007211](https://doi.org/10.1109/JSAC.2020.3007211) (cit. on pp. 28, 32, 34, 48).
- [0] Y. Liu et al. “Reconfigurable intelligent surfaces: Principles and opportunities”. In: *IEEE Commun. Surv. Tutor.* 23.3 (July 2020), pp. 1546–1577. doi: [10.1109/COMST.2021.3077737](https://doi.org/10.1109/COMST.2021.3077737) (cit. on pp. 28, 32, 51).
- [0] M. Munochiveyi et al. “Reconfigurable Intelligent Surface Aided Multi-User Communications: State-of-the-Art Techniques and Open Issues”. In: *IEEE Access* 9 (Aug. 2021), pp. 118584–118605. doi: [10.1109/ACCESS.2021.3107316](https://doi.org/10.1109/ACCESS.2021.3107316) (cit. on pp. 28, 32).
- [0] Y. Jia et al. “Non-terrestrial Communications Assisted by Reconfigurable Intelligent Surfaces”. In: *Available at the Early Access Issues, ArXiv preprint arXiv:2109.00876* (Sept. 2021). arXiv: [2109.00876 \[cs.IT\]](https://arxiv.org/abs/2109.00876). URL: <https://arxiv.org/abs/2109.00876> (cit. on pp. 28, 32).
- [0] X. Pang et al. “When UAV meets IRS: Expanding air-ground networks via passive reflection”. In: *IEEE Wirel. Commun.* 28.5 (Nov. 2021), pp. 164–170. doi: [10.1109/MWC.010.2000528](https://doi.org/10.1109/MWC.010.2000528) (cit. on pp. 28, 32, 56, 67).
- [0] S. Alfattani et al. “Aerial platforms with reconfigurable smart surfaces for 5G and beyond”. In: *IEEE Commun. Mag.* 59 (Feb. 2021), pp. 96–102. doi: [10.1109/MCOM.001.2000350](https://doi.org/10.1109/MCOM.001.2000350) (cit. on pp. 28, 32, 56).

- [0] H. Lu et al. “Enabling panoramic full-angle reflection via aerial intelligent reflecting surface”. In: *2020 IEEE Inter. Conf. Commun. Workshops (ICC Workshops)* (July 2020), pp. 1–6. doi: [10.1109/ICCWorKshops49005.2020.9145305](https://doi.org/10.1109/ICCWorKshops49005.2020.9145305) (cit. on p. 29).
- [0] L. Haiquan et al. “Aerial intelligent reflecting surface: Joint placement and passive beam-forming design with 3D beam flattening”. In: *Available at the Early Access Issues, ArXiv preprint arXiv:2007.13295* (Nov. 2020). arXiv: [2007.13295](https://arxiv.org/abs/2007.13295) [eess.SP]. URL: <https://arxiv.org/abs/2007.13295> (cit. on p. 29).
- [0] B. Shang, R. Shafin, and L. Liu. “UAV swarm-enabled aerial reconfigurable intelligent surface”. In: *IEEE Wirel. Commun.* 28.5 (Oct. 2021), pp. 156–163. doi: [10.1109/MWC.01.2000526](https://doi.org/10.1109/MWC.01.2000526) (cit. on pp. 29, 32).
- [0] C. Liu, M. A. Syed, and L. Wei. “Toward ubiquitous and flexible coverage of UAV-IRS-assisted NOMA networks”. In: *Available at the Early Access Issues, ArXiv preprint arXiv:2110.04699* abs/2110.04699 (Oct. 2021). arXiv: [2110.04699](https://arxiv.org/abs/2110.04699). URL: <https://arxiv.org/abs/2110.04699> (cit. on p. 29).
- [0] T. N. Do et al. “Aerial reconfigurable intelligent surface-aided wireless communication systems”. In: *IEEE Inter. Symp. on Pers., Ind. and Mob. Rad. Commun. (IEEE PIMRC 2021)* (Oct. 2021). doi: [10.1109/PIMRC50174.2021.9569450](https://doi.org/10.1109/PIMRC50174.2021.9569450) (cit. on pp. 29, 36, 56, 57, 67, 71, 72).
- [0] T. Zhou et al. “Achievable rate optimization for aerial intelligent reflecting surface-aided cell-free massive MIMO system”. In: *IEEE Access* 9 (Dec. 2021), pp. 3828–3837. doi: [10.1109/ACCESS.2020.3047450](https://doi.org/10.1109/ACCESS.2020.3047450) (cit. on p. 29).
- [0] Y. Li et al. “Aerial reconfigurable intelligent surface-enabled URLLC UAV systems”. In: *IEEE Access* 9 (Oct. 2021), pp. 140248–140257. doi: [10.1109/ACCESS.2021.3119268](https://doi.org/10.1109/ACCESS.2021.3119268) (cit. on p. 29).
- [0] M. T. Mamaghani and Y. Hong. “Aerial intelligent reflecting surface enabled terahertz covert Communications in Beyond-5G Internet of Things”. In: *Available at the Early Access Issues, ArXiv preprint arXiv:2111.11650* abs/2111.11650 (Nov. 2021). arXiv: [2111.11650](https://arxiv.org/abs/2111.11650). URL: <https://arxiv.org/abs/2111.11650> (cit. on p. 29).
- [0] H.-B. Jeon et al. “An Energy-efficient Aerial Backhaul System with Reconfigurable Intelligent Surface”. In: *Available at the Early Access Issues, ArXiv preprint arXiv:2104.01723* (Apr. 2021). arXiv: [2104.01723](https://arxiv.org/abs/2104.01723) [eess.SP]. URL: <https://arxiv.org/abs/2104.01723> (cit. on p. 29).
- [0] A. Khalili et al. “Resource Management for Transmit Power Minimization in UAV-Assisted RIS HetNets Supported by Dual Connectivity”. In: *IEEE Trans. Wirel. Commun.* abs/2106.13174 (Aug. 2021), pp. 1–1. doi: [10.1109/TWC.2021.3107306](https://doi.org/10.1109/TWC.2021.3107306) (cit. on p. 29).

BIBLIOGRAPHY

- [0] X. Cao et al. “Reconfigurable intelligent surface-assisted aerial-terrestrial communications via multi-task learning”. In: *IEEE J. Sel. Areas Commun.* 39.10 (June 2021), pp. 3035–3050. doi: [10.1109/JSAC.2021.3088634](https://doi.org/10.1109/JSAC.2021.3088634) (cit. on p. 29).
- [0] X. Mu et al. “Intelligent reflecting surface enhanced multi-UAV NOMA networks”. In: *IEEE J. Sel. Areas Commun.* 39.10 (Oct. 2021), pp. 3051–3066. issn: 1558-0008. doi: [10.1109/jsac.2021.3088679](https://doi.org/10.1109/jsac.2021.3088679) (cit. on p. 29).
- [0] S. Li et al. “Reconfigurable intelligent surface assisted UAV communication: Joint trajectory design and passive beamforming”. In: *IEEE Wirel. Commun. Lett.* 9.5 (Jan. 2020), pp. 716–720. doi: [10.1109/LWC.2020.2966705](https://doi.org/10.1109/LWC.2020.2966705) (cit. on pp. 29, 67).
- [0] K. K. Nguyen et al. “RIS-assisted UAV communications for IoT with wireless power transfer using deep reinforcement learning”. In: *Available at the Early Access Issues, ArXiv preprint arXiv:2108.02889* (Aug. 2021). arXiv: [2108.02889](https://arxiv.org/abs/2108.02889) [eess.SP]. URL: <https://arxiv.org/abs/2108.02889> (cit. on p. 29).
- [0] A. Al-Hilo et al. “RIS-Assisted UAV for Timely Data Collection in IoT Networks”. In: *Available at the Early Access Issues, ArXiv preprint arXiv:2103.17162* (Mar. 2021). arXiv: [2103.17162](https://arxiv.org/abs/2103.17162) [eess.IV]. URL: <https://arxiv.org/abs/2103.17162> (cit. on p. 29).
- [0] X. Liu, Y. Liu, and Y. Chen. “Machine learning empowered trajectory and passive beamforming design in UAV-RIS wireless networks”. In: *IEEE J. Sel. Areas Commun.* 39.7 (Dec. 2021), pp. 2042–2055. doi: [10.1109/JSAC.2020.3041401](https://doi.org/10.1109/JSAC.2020.3041401) (cit. on pp. 29, 30).
- [0] K. K. Nguyen et al. “Reconfigurable Intelligent Surface-assisted Multi-UAV Networks: Efficient Resource Allocation with Deep Reinforcement Learning”. In: *IEEE J. Sel. Top. Signal Process* (Dec. 2021), pp. 1–1. doi: [10.1109/JSTSP.2021.3134162](https://doi.org/10.1109/JSTSP.2021.3134162) (cit. on pp. 29, 30).
- [0] N. Agrawal et al. “Performance Evaluation of RIS-Assisted UAV-Enabled Vehicular Communication System With Multiple Non-Identical Interferers”. In: *IEEE Trans. Intell. Transp. Syst.* (Nov. 2021), pp. 1–12. doi: [10.1109/TITS.2021.3123072](https://doi.org/10.1109/TITS.2021.3123072) (cit. on pp. 29, 30).
- [0] S. Li et al. “Robust Secure UAV Communications with the Aid of Reconfigurable Intelligent Surfaces”. In: *IEEE Trans. Wirel. Commun.* 20.10 (Apr. 2021), pp. 6402–6417. doi: [10.1109/TWC.2021.3073746](https://doi.org/10.1109/TWC.2021.3073746) (cit. on pp. 29, 30).
- [0] Z. Ding et al. “A State-of-the-Art Survey on Reconfigurable Intelligent Surface-Assisted Non-Orthogonal Multiple Access Networks”. In: *Proceedings of the IEEE* 110.9 (2022), pp. 1358–1379. doi: [10.1109/JPROC.2022.3174140](https://doi.org/10.1109/JPROC.2022.3174140) (cit. on pp. 30, 32).
- [0] Y. Liu et al. “Reconfigurable intelligent surface (RIS) aided multi-user networks: Interplay between NOMA and RIS”. In: *Available at the Early Access Issues, ArXiv preprint arXiv:2011.13336* (Oct. 2021). arXiv: [2011.13336](https://arxiv.org/abs/2011.13336) [cs.IT]. URL: <https://arxiv.org/abs/2011.13336> (cit. on pp. 30, 32, 48).

- [0] A. S. Sena et al. “What Role Do Intelligent Reflecting Surfaces Play in Multi-Antenna Non-Orthogonal Multiple Access?” In: *IEEE Wirel. Commun.* 27.5 (Oct. 2020), pp. 24–31. doi: [10.1109/MWC.001.2000061](https://doi.org/10.1109/MWC.001.2000061) (cit. on pp. 30, 32, 37, 39, 50).
- [0] G. Yang et al. “Reconfigurable intelligent surface-assisted non-orthogonal multiple access”. In: *IEEE Trans. Wirel. Commun.* 20.5 (Jan. 2021), pp. 3137–3151. doi: [10.1109/TWC.2020.3047632](https://doi.org/10.1109/TWC.2020.3047632) (cit. on pp. 30, 35).
- [0] Y. Cheng et al. “Downlink and Uplink Intelligent Reflecting Surface Aided Networks: NOMA and OMA”. In: *IEEE Trans. Wirel. Commun.* 20.6 (June 2021), pp. 3988–4000. issn: 1558-2248. doi: [10.1109/twc.2021.3054841](https://doi.org/10.1109/twc.2021.3054841) (cit. on p. 30).
- [0] Z. Sun and Y. Jing. “On the performance of multi-Antenna IRS-assisted NOMA networks with continuous and discrete IRS phase shifting”. In: *IEEE Trans. Wirel. Commun.* (Oct. 2021), pp. 1–1. doi: [10.1109/TWC.2021.3117494](https://doi.org/10.1109/TWC.2021.3117494) (cit. on pp. 30, 36).
- [0] A.-T. Le et al. “Enabling User Grouping and Fixed Power Allocation Scheme for Reconfigurable Intelligent Surfaces-Aided Wireless Systems”. In: *IEEE Access* 9 (June 2021), pp. 92263–92275. doi: [10.1109/ACCESS.2021.3092335](https://doi.org/10.1109/ACCESS.2021.3092335) (cit. on p. 30).
- [0] Q. Chen et al. “Impact of Residual Hardware Impairment on the IoT Secrecy Performance of RIS-Assisted NOMA Networks”. In: *IEEE Access* 9 (2021), pp. 42583–42592. doi: [10.1109/ACCESS.2021.3065760](https://doi.org/10.1109/ACCESS.2021.3065760) (cit. on p. 30).
- [0] A. S. de Sena et al. “IRS-Assisted Massive MIMO-NOMA Networks: Exploiting Wave Polarization”. In: *IEEE Trans. Wirel. Commun.* 20.11 (May 2021), pp. 7166–7183. doi: [10.1109/TWC.2021.3081419](https://doi.org/10.1109/TWC.2021.3081419) (cit. on p. 30).
- [0] T. Hou et al. “MIMO-NOMA Networks Relying on Reconfigurable Intelligent Surface: A Signal Cancellation-Based Design”. In: *IEEE Trans. Commun.* 68.11 (Aug. 2020), pp. 6932–6944. doi: [10.1109/TCOMM.2020.3018179](https://doi.org/10.1109/TCOMM.2020.3018179) (cit. on p. 30).
- [0] Z. Yang et al. “Machine Learning for User Partitioning and Phase Shifters Design in RIS-Aided NOMA Networks”. In: *IEEE Trans. Commun.* 69.11 (July 2021), pp. 7414–7428. doi: [10.1109/TCOMM.2021.3100866](https://doi.org/10.1109/TCOMM.2021.3100866) (cit. on p. 31).
- [0] X. Xu et al. *Graph-Emerged Multi-Agent Learning for Smart Reconfigurable THz MIMO-NOMA Networks*. Nov. 2021. doi: [10.1109/JSAC.2021.3126079](https://doi.org/10.1109/JSAC.2021.3126079) (cit. on p. 31).
- [0] R. Zhong et al. “AI Empowered RIS-Assisted NOMA Networks: Deep Learning or Reinforcement Learning?” In: *IEEE J. Sel. Areas Commun.* 40.1 (Jan. 2022), pp. 182–196. doi: [10.1109/JSAC.2021.3126068](https://doi.org/10.1109/JSAC.2021.3126068) (cit. on p. 31).
- [0] H. M. Hariz et al. “AI-based Radio Resource Management and Trajectory Design for PD-NOMA Communication in IRS-UAV Assisted Networks”. In: *Available at the Early Access Issues, ArXiv preprint arXiv:2111.03869* (Nov. 2021). arXiv: [2111.03869](https://arxiv.org/abs/2111.03869) [eess.SP]. url: <https://arxiv.org/abs/2111.03869> (cit. on p. 31).

BIBLIOGRAPHY

- [0] X. Gao, Y. Liu, and X. Mu. “Trajectory and Passive Beamforming Design for IRS-aided Multi-Robot NOMA Indoor Networks”. In: (Nov. 2020), pp. 1–6. doi: [10.1109/ICC4292.2021.9500747](https://doi.org/10.1109/ICC4292.2021.9500747) (cit. on p. 31).
- [0] S. Jiao et al. “Deep Reinforcement Learning Based Optimization for IRS Based UAV-NOMA Downlink Networks”. In: *Available at the Early Access Issues, ArXiv preprint arXiv:2106.09616* (June 2021). arXiv: [2106.09616](https://arxiv.org/abs/2106.09616) [eess.SP]. URL: <https://arxiv.org/abs/2106.09616> (cit. on p. 31).
- [0] C. Huang et al. “Deep Reinforcement Learning-Based Relay Selection in Intelligent Reflecting Surface Assisted Cooperative Networks”. In: *IEEE Wirel. Commun. Lett.* 10.5 (Feb. 2021), pp. 1036–1040. doi: [10.1109/LWC.2021.3056620](https://doi.org/10.1109/LWC.2021.3056620) (cit. on p. 31).
- [0] X. Jia and X. Zhou. “IRS-Assisted Ambient Backscatter Communications Utilizing Deep Reinforcement Learning”. In: *IEEE Wirel. Commun. Lett.* 10.11 (July 2021), pp. 2374–2378. doi: [10.1109/LWC.2021.3100901](https://doi.org/10.1109/LWC.2021.3100901) (cit. on p. 31).
- [0] J. Xu et al. “Optimization for Master-UAV-powered Auxiliary-Aerial-IRS-assisted IoT Networks: An Option-based Multi-agent Hierarchical Deep Reinforcement Learning Approach”. In: *Available at the Early Access Issues, ArXiv preprint arXiv:2112.10630* (Dec. 2021). arXiv: [2112.10630](https://arxiv.org/abs/2112.10630) [eess.SY]. URL: <https://arxiv.org/abs/2112.10630> (cit. on p. 31).
- [0] X. Gao et al. “Resource Allocation In IRSs Aided MISO-NOMA Networks: A Machine Learning Approach”. In: *GLOBECOM 2020 - 2020 IEEE Global Commun. Conf.* Dec. 2020, pp. 1–6. doi: [10.1109/GLOBECOM42002.2020.9348009](https://doi.org/10.1109/GLOBECOM42002.2020.9348009) (cit. on p. 31).
- [0] Z. Mao, M. Peng, and X. Liu. “Channel estimation for reconfigurable intelligent surface assisted wireless communication systems in mobility scenarios”. In: *China Commun.* 18.3 (Mar. 2021), pp. 29–38 (cit. on pp. 32, 47).
- [0] Z. Wan et al. “Terahertz Massive MIMO With Holographic Reconfigurable Intelligent Surfaces”. In: *IEEE Trans. Commun.* 69.7 (Mar. 2021), pp. 4732–4750 (cit. on pp. 32, 49).
- [0] C. Bettstetter, H. Hartenstein, and X. Costa-Pérez. “Stochastic properties of the random waypoint mobility model”. In: *Wirel. Netw.* 10 (2004), pp. 555–567 (cit. on p. 35).
- [0] A. H. Sawalme et al. “Wireless Coverage for Mobile Users in Dynamic Environments Using UAV”. In: *IEEE Access* 7 (Aug. 2019), pp. 126376–126390 (cit. on p. 35).
- [0] S. M. R. Islam et al. “Power-domain non-orthogonal multiple Access (NOMA) in 5G systems: Potentials and challenges”. In: *IEEE Commun. Surv. Tut.* 19.2 (Oct. 2017), pp. 721–742. doi: [{10.1109/COMST.2016.2621116}](https://doi.org/10.1109/COMST.2016.2621116) (cit. on p. 35).
- [0] Huang, Chongwen and Zappone, Alessio and Alexandropoulos, George C. and Debbah, Mérouane and Yuen, Chau. “Reconfigurable intelligent surfaces for energy efficiency in wireless communication”. In: *IEEE Trans. Wirel. Commun.* 18.8 (06 2019), 4157–4170. doi: [{10.1109/TWC.2019.2922609}](https://doi.org/10.1109/TWC.2019.2922609) (cit. on p. 43).

- [0] Y.-C. Liang et al. “Reconfigurable intelligent surfaces for smart wireless environments: channel estimation, system design and applications in 6G network”. In: *Sci. China Inf. Sci.* 64 (July 2021), pp. 1869–1919 (cit. on p. 47).
- [0] Y. Pan et al. “Sum-Rate Maximization for Intelligent Reflecting Surface Assisted Terahertz Communications”. In: *IEEE Trans. Veh. Technol.* (Jan. 2022), pp. 1–1 (cit. on p. 49).
- [0] Z. Chen et al. “Towards intelligent reflecting surface empowered 6G terahertz communications: A survey”. In: *China Communications* 18.5 (May 2021), pp. 93–119 (cit. on p. 49).
- [0] L. Xu et al. “Joint Location, Bandwidth and Power Optimization for THz-Enabled UAV Communications”. In: *IEEE Commun. Lett.* 25.6 (Mar. 2021), pp. 1984–1988 (cit. on p. 50).
- [0] Y. Pan et al. “UAV-Assisted and Intelligent Reflecting Surfaces-Supported Terahertz Communications”. In: *IEEE Wirel. Commun. Lett.* 10.6 (Mar. 2021), pp. 1256–1260 (cit. on p. 50).
- [0] Q. Pan et al. “Differential Privacy and IRS Empowered Intelligent Energy Harvesting for 6G Internet of Things”. In: *IEEE Internet Things J.* (Aug. 2021), pp. 1–1 (cit. on p. 51).
- [0] Z. Feng, B. Clerckx, and Y. Zhao. “Waveform and Beamforming Design for Intelligent Reflecting Surface Aided Wireless Power Transfer: Single-User and Multi-User Solutions”. In: *IEEE Trans. Wirel. Commun.* (Jan. 2022), pp. 1–1 (cit. on p. 51).
- [0] Jian, Mengnan and Liu, Ruiqi and Chen, Yijian. “Standardization for Reconfigurable Intelligent Surfaces: Progresses, Challenges and the Road Ahead”. In: *2021 IEEE/CIC Inter. Conf. Commun. China (ICCC Workshops)*. 07 2021, 337–342 (cit. on p. 52).
- [0] Ruiqi Liu and Qingqing Wu and Marco Di Renzo and Yifei Yuan. “A Path to Smart Radio Environments: An Industrial Viewpoint on Reconfigurable Intelligent Surfaces”. In: *IEEE Wirel. Commun.* (01 2022), 1–7 (cit. on p. 52).
- [0] 3GPP. *Release 17- 5G Enhancement for UAVs*. URL: %7Bhttps://www.3gpp.org/release-17%7D (cit. on p. 52).
- [0] B. Clerckx et al. “Rate splitting for MIMO wireless networks: a promising PHY-layer strategy for LTE evolution”. In: *IEEE Commun. Mag.* 54.5 (May 2016), pp. 98–105. DOI: 10.1109/MCOM.2016.7470942 (cit. on pp. 55, 57, 67, 71).
- [0] Y. Mao, B. Clerckx, and V. Li. “Rate-Splitting Multiple Access for Downlink Communication Systems: Bridging, Generalizing and Outperforming SDMA and NOMA”. In: *EURASIP J. Wirel. Commun. Net.* 2018 (May 2018). DOI: 10.1186/s13638-018-1104-7 (cit. on pp. 55, 67).
- [0] Z. Yang et al. “Optimization of Rate Allocation and Power Control for Rate Splitting Multiple Access (RSMA)”. In: *IEEE Trans. Commun.* 69.9 (Dec. 2021), pp. 5988–6002. DOI: 10.1109/TCOMM.2021.3091133 (cit. on pp. 55, 67).
- [0] A. Bansal et al. “Rate-Splitting Multiple Access for Intelligent Reflecting Surface Aided Multi-User Communications”. In: *IEEE Trans. Veh. Technol.* 70.9 (Aug. 2021), pp. 9217–9229. DOI: 10.1109/TVT.2021.3102212 (cit. on p. 56).

BIBLIOGRAPHY

- [0] H. Fu, S. Feng, and D. W. Kwan Ng. “Resource Allocation Design for IRS-Aided Downlink MU-MISO RSMA Systems”. In: *2021 IEEE Int. Conf. Commun. Works. (ICC Workshops)*. July 2021, pp. 1–6. doi: [10.1109/ICCWorkshops50388.2021.9473650](https://doi.org/10.1109/ICCWorkshops50388.2021.9473650) (cit. on p. 56).
- [0] Z. Yang et al. “Energy Efficient Rate Splitting Multiple Access (RSMA) with Reconfigurable Intelligent Surface”. In: *2020 IEEE Int. Conf. Commun. Workshops (ICC Workshops)*. June 2020, pp. 1–6. doi: [10.1109/ICCWorkshops49005.2020.9145189](https://doi.org/10.1109/ICCWorkshops49005.2020.9145189) (cit. on p. 56).
- [0] A. Bansal, N. Agrawal, and K. Singh. “Rate-Splitting Multiple Access for UAV-Based RIS-Enabled Interference-Limited Vehicular Communication System”. In: *IEEE Trans. Intel. Veh.* 8.1 (2023), pp. 936–948. doi: [10.1109/TIV.2022.3168159](https://doi.org/10.1109/TIV.2022.3168159) (cit. on p. 56).
- [0] R. Feng et al. “Robust Secure Beamforming in MISO Full-Duplex Two-Way Secure Communications”. In: *IEEE Trans. Veh. Technol.* 65.1 (Jan. 2016), pp. 408–414. doi: [10.1109/TVT.2015.2394370](https://doi.org/10.1109/TVT.2015.2394370) (cit. on pp. 60, 61, 75, 76, 103).
- [0] A. S. de Sena et al. “Massive MIMO-NOMA Networks With Imperfect SIC: Design and Fairness Enhancement”. In: *IEEE Trans. Wirel. Commun.* 19.9 (June 2020), pp. 6100–6115 (cit. on pp. 63, 81).
- [0] S. Hochreiter and J. Schmidhuber. “Long Short-term Memory”. In: *Neural computation* 9 (Dec. 1997), pp. 1735–80. doi: [10.1162/neco.1997.9.8.1735](https://doi.org/10.1162/neco.1997.9.8.1735) (cit. on p. 68).
- [0] G. Gui et al. “Deep Learning for an Effective Nonorthogonal Multiple Access Scheme”. In: *IEEE Trans. Veh. Technol.* 67.9 (2018), pp. 8440–8450. doi: [10.1109/TVT.2018.2848294](https://doi.org/10.1109/TVT.2018.2848294) (cit. on p. 68).
- [0] S. Kim, J. Son, and B. Shim. “Energy-Efficient Ultra-Dense Network Using LSTM-based Deep Neural Networks”. In: *IEEE Trans. Wirel. Commun.* 20.7 (2021), pp. 4702–4715. doi: [10.1109/TWC.2021.3061577](https://doi.org/10.1109/TWC.2021.3061577) (cit. on p. 68).
- [0] A. K. Kowshik et al. “Deep Learning-Based Signal Detection for Rate-Splitting Multiple Access Under Generalized Gaussian Noise”. In: *IEEE O. J. Veh. Technol.* 4 (2023), pp. 257–270. doi: [10.1109/OJVT.2023.3238034](https://doi.org/10.1109/OJVT.2023.3238034) (cit. on p. 68).
- [0] X. Gao et al. “Machine Learning Empowered Resource Allocation in IRS Aided MISO-NOMA Networks”. In: *IEEE Trans. Wirel. Commun.* 21.5 (2022), pp. 3478–3492. doi: [10.1109/TWC.2021.3122409](https://doi.org/10.1109/TWC.2021.3122409) (cit. on pp. 68, 72).
- [0] X. Gao et al. “Intelligent Trajectory Design for RIS-NOMA aided Multi-robot Communications”. In: *IEEE Trans. Wirel. Commun.* (2023), pp. 1–1. doi: [10.1109/TWC.2023.3254130](https://doi.org/10.1109/TWC.2023.3254130) (cit. on pp. 68, 72).
- [0] C. Nguyen, T. M. Hoang, and A. A. Cheema. “Channel Estimation Using CNN-LSTM in RIS-NOMA Assisted 6G Network”. In: *IEEE Trans. Mach. Lear. Commun. Netw.* 1 (2023), pp. 43–60. doi: [10.1109/TMLCN.2023.3278232](https://doi.org/10.1109/TMLCN.2023.3278232) (cit. on p. 68).
- [0] X. Liu et al. “Learning-Based Prediction, Rendering and Transmission for Interactive Virtual Reality in RIS-Assisted Terahertz Networks”. In: *IEEE J. Sel. A. Commun.* 40.2 (2022), pp. 710–724. doi: [10.1109/JSAC.2021.3118405](https://doi.org/10.1109/JSAC.2021.3118405) (cit. on p. 68).

- [0] K. D. Gupta et al. “LSTM-Based Energy-Efficient Wireless Communication With Reconfigurable Intelligent Surfaces”. In: *IEEE Trans. Green Commun. Netw.* 6.2 (2022), pp. 704–712. doi: [10.1109/TGCN.2021.3135437](https://doi.org/10.1109/TGCN.2021.3135437) (cit. on p. 68).
- [0] H. Kim, Y. Byun, and B. Shim. “LSTM-based RIS Phase Shift Control for V2X Communication Systems”. In: *2022 IEEE 96th Veh. Technol. Conf.(VTC2022-Fall)*. 2022, pp. 1–5. doi: [10.1109/VTC2022-Fall57202.2022.10012864](https://doi.org/10.1109/VTC2022-Fall57202.2022.10012864) (cit. on p. 68).
- [0] L. Yan et al. “KF-LSTM Based Beam Tracking for UAV-Assisted mmWave HSR Wireless Networks”. In: *IEEE Trans. Veh. Technol.* 71.10 (2022), pp. 10796–10807. doi: [10.1109/TVT.2022.3187978](https://doi.org/10.1109/TVT.2022.3187978) (cit. on p. 69).
- [0] S. Zhang and R. Cao. “Multi-Objective Optimization for UAV-Enabled Wireless Powered IoT Networks: An LSTM-Based Deep Reinforcement Learning Approach”. In: *IEEE Commun Lett* 26.12 (2022), pp. 3019–3023. doi: [10.1109/LCOMM.2022.3210660](https://doi.org/10.1109/LCOMM.2022.3210660) (cit. on p. 69).
- [0] F. Guo et al. “Machine Learning for Predictive Deployment of UAVs With Multiple Access”. In: *IEEE O. J. Commun. Soc.* 4 (2023), pp. 908–921. doi: [10.1109/OJCOMS.2023.3264465](https://doi.org/10.1109/OJCOMS.2023.3264465) (cit. on p. 69).
- [0] R. Kant, P. Saini, and J. Kumari. “Long Short-Term Memory Auto-Encoder-Based Position Prediction Model for Fixed-Wing UAV During Communication Failure”. In: *IEEE Trans. Art. Intel.* 4.1 (2023), pp. 173–181. doi: [10.1109/TAI.2022.3153763](https://doi.org/10.1109/TAI.2022.3153763) (cit. on p. 69).
- [0] K. Li, W. Ni, and F. Dressler. “LSTM-Characterized Deep Reinforcement Learning for Continuous Flight Control and Resource Allocation in UAV-Assisted Sensor Network”. In: *IEEE Int. Things J.* 9.6 (2022), pp. 4179–4189. doi: [10.1109/JIOT.2021.3102831](https://doi.org/10.1109/JIOT.2021.3102831) (cit. on p. 69).
- [0] Y. Zhang et al. “Recurrent LSTM-based UAV Trajectory Prediction with ADS-B Information”. In: *GLOBECOM 2022 - 2022 IEEE Global Commun. Conf.* 2022, pp. 1–6. doi: [10.1109/GLOBECOM48099.2022.10000919](https://doi.org/10.1109/GLOBECOM48099.2022.10000919) (cit. on p. 69).
- [0] A. Bansal, N. Agrawal, and K. Singh. “Rate-Splitting Multiple Access for UAV-Based RIS-Enabled Interference-Limited Vehicular Communication System”. In: *IEEE Trans. Intel. Veh.* 8.1 (2023), pp. 936–948. doi: [10.1109/TIV.2022.3168159](https://doi.org/10.1109/TIV.2022.3168159) (cit. on p. 69).
- [0] S. K. Singh et al. “RSMA for Hybrid RIS-UAV-aided Full-Duplex Communications with Finite Blocklength Codes under Imperfect SIC”. In: *IEEE Trans. Wirel. Commun.* (2023), pp. 1–1. doi: [10.1109/TWC.2023.3238808](https://doi.org/10.1109/TWC.2023.3238808) (cit. on p. 69).
- [0] B. K. S. Lima et al. “Rate-Splitting Multiple Access Networks Assisted by Aerial Intelligent Reflecting Surfaces”. In: *2022 IEEE Latin-American Conf. Commun. (LATINCOM)*. 2022, pp. 1–6. doi: [10.1109/LATINCOM56090.2022.10000454](https://doi.org/10.1109/LATINCOM56090.2022.10000454) (cit. on p. 69).
- [0] B. K. S. Lima et al. “Power Allocation, Relay Selection, and User Pairing for Cooperative NOMA Systems with Rate Fairness”. In: *2021 IEEE 93rd Veh. Technol. Conf. (VTC2021-Spring)*. 2021, pp. 1–5. doi: [10.1109/VTC2021-Spring51267.2021.9449065](https://doi.org/10.1109/VTC2021-Spring51267.2021.9449065) (cit. on p. 70).

BIBLIOGRAPHY

- [0] C. You, B. Zheng, and R. Zhang. “Channel Estimation and Passive Beamforming for Intelligent Reflecting Surface: Discrete Phase Shift and Progressive Refinement”. In: *IEEE J. Sel. A. Commun.* 38.11 (2020), pp. 2604–2620. doi: [10.1109/JSAC.2020.3007056](https://doi.org/10.1109/JSAC.2020.3007056) (cit. on p. 72).
- [0] I. Pólik and T. Terlaky. “Interior Point Methods for Nonlinear Optimization”. In: *Lecture Notes in Mathematics -Springer-verlag-* 1989 (Jan. 2010). doi: [10.1007/978-3-642-11339-0_4](https://doi.org/10.1007/978-3-642-11339-0_4) (cit. on p. 77).
- [0] J. P. Matos-Carvalho, S. D. Correia, and S. Tomic. “Sensitivity Analysis of LSTM Networks for Fall Detection Wearable Sensors”. In: *2023 6th Conference on Cloud and Internet of Things (CIoT)*. 2023, pp. 112–118. doi: [10.1109/CIoT57267.2023.10084906](https://doi.org/10.1109/CIoT57267.2023.10084906) (cit. on pp. 77, 81).
- [0] R. Santos‡ et al. “A Hybrid LSTM-based Neural Network for Satellite-less UAV Navigation”. In: *2023 6th Conference on Cloud and Internet of Things (CIoT)*. 2023, pp. 91–97. doi: [10.1109/CIoT57267.2023.10084873](https://doi.org/10.1109/CIoT57267.2023.10084873) (cit. on p. 77).
- [0] R. Santos et al. “Applying Deep Neural Networks to Improve UAV Navigation in Satellite-less Environments”. In: *2022 International Young Engineers Forum (YEF-ECE)*. 2022, pp. 63–68. doi: [10.1109/YEF-ECE55092.2022.9850152](https://doi.org/10.1109/YEF-ECE55092.2022.9850152) (cit. on p. 77).
- [0] J. P. Matos-Carvalho et al. “Terrain Classification Using W-K Filter and 3D Navigation with Static Collision Avoidance”. In: *Intelligent Systems and Applications*. Ed. by Y. Bi, R. Bhatia, and S. Kapoor. Cham: Springer International Publishing, 2020, pp. 1122–1137. ISBN: 978-3-030-29513-4 (cit. on pp. 79, 80).
- [0] R. Sacoto-Martins et al. “Multi-purpose Low Latency Streaming Using Unmanned Aerial Vehicles”. In: *2020 12th International Symposium on Communication Systems, Networks and Digital Signal Processing (CSNDSP)*. 2020, pp. 1–6. doi: [10.1109/CSNDSP49049.2020.9249562](https://doi.org/10.1109/CSNDSP49049.2020.9249562) (cit. on p. 81).
- [0] J. P. Matos-Carvalho, J. M. Fonseca, and A. Mora. “UAV Downwash Dynamic Texture Features for Terrain Classification on Autonomous Navigation”. In: *2018 Federated Conference on Computer Science and Information Systems (FedCSIS)*. 2018, pp. 1079–1083 (cit. on p. 81).
- [0] H. Fu et al. “Robust Secure Beamforming Design for Two-User Downlink MISO Rate-Splitting Systems”. In: *IEEE Trans. Wirel. Commun.* 19.12 (Sept. 2020), pp. 8351–8365. doi: [10.1109/TWC.2020.3021725](https://doi.org/10.1109/TWC.2020.3021725) (cit. on p. 103).

APPENDIX

A

Proposition 2: Chapter 4

Proposition 2: The solution for \mathbf{P}_m of the problem (4.27a) satisfies the rank-one conditions.

To verify if the solution for \mathbf{P}_m satisfies the rank-one condition, we first investigate if the obtained solution satisfies the Karush-Kuhn-Tucker (KKT) conditions. To verify the KKT conditions, it is formulated the Lagrangian function of problem (4.27a) following a similar approach provided in [0] and [0]. Without loss of generalization, the Lagrangian function of problem (4.27a) with respect to \mathbf{P}_c^* is given by

$$\mathcal{L}(\mathbf{P}_c^*) = \sum_{k=1}^K \mu_k^* [\rho \mathbf{h}_k \mathbf{P}_c^* \mathbf{h}_k^H \alpha_k] - \mathbf{P}_c^* \boldsymbol{\Gamma}_c^* + \lambda^* [\mathbf{P}_c^* - P_{tot}], \quad (\text{A.1})$$

where μ^* and λ^* are the optimal dual variables associated with the constraint (4.27c) and (4.27e), respectively. Besides, $\boldsymbol{\Gamma}_c^*$ is the optimal dual variable matrix associated with constraint (4.27g). The KKT conditions of problem (4.27a) are expressed as

$$\begin{aligned} \bar{C}1 : \boldsymbol{\Gamma}_c^* &\succeq \mathbf{0}, \quad \bar{C}2 : \mathbf{P}_c^* \boldsymbol{\Gamma}_c^* = \mathbf{0}, \\ \bar{C}3 : \mathbf{P}_c^* &\succeq \mathbf{0}, \quad \bar{C}4 : \lambda^* [\mathbf{P}_c^* - P_{tot}] = 0. \end{aligned}$$

Taking partial derivate of $\mathcal{L}(\mathbf{P}_c^*)$ in (A.1) and applying the KKT conditions, we obtain

$$\nabla_{\mathbf{P}_c^*} \mathcal{L}(\mathbf{P}_c^*) = \sum_{k=1}^K \mu_k^* [\rho \mathbf{h}_k \mathbf{h}_k^H \alpha_k] - \boldsymbol{\Gamma}_c^* + \lambda^* \mathbf{I}_N, \quad (\text{A.2})$$

For $\nabla_{\mathbf{P}_c^*} \mathcal{L}(\mathbf{P}_c^*) = 0$, we obtain

$$\boldsymbol{\Gamma}_c^* = \lambda^* \mathbf{I}_N - \underbrace{\sum_{k=1}^K \mu_k^* [\rho \mathbf{h}_k \mathbf{h}_k^H \alpha_k]}_{\mathbf{H}_c^*}, \quad (\text{A.3})$$

where \mathbf{H}_c^* is a Hermitian matrix. Since $\boldsymbol{\Gamma}_c^* = \lambda^* \mathbf{I}_N - \mathbf{H}_c^* \succeq \mathbf{0}$ is positive semi-definite for KKT condition $\bar{C}1$, and $\lambda^* \geq \tilde{\lambda}_{\mathbf{H}_c^*}^{\max} \geq 0$, in which $\tilde{\lambda}_{\mathbf{H}_c^*}^{\max}$ is the maximum eigenvalue of \mathbf{H}_c^* . From

the condition $\bar{C}2$, since $\lambda^* > \tilde{\lambda}_{\mathbf{H}_c^*}^{\max}$, $\boldsymbol{\Gamma}_c^*$ has a full rank. On the other hand, if $\lambda^* = \tilde{\lambda}_{\mathbf{H}_c^*}^{\max}$ and $\text{Rank}(\boldsymbol{\Gamma}_c^*) = N - 1$, we have $\text{Rank}(\mathbf{P}_c^*) = 1$. Similarly, it is possible to prove that the solution of $\mathbf{P}_k^*, \forall k \in \mathcal{K}$ is rank-one.

■

